1-1-1992

Structure and star forming activities of the cold, massive molecular cloud G216-2.5.

Youngung, Lee
University of Massachusetts Amherst

STRUCTURE AND STAR FORMING ACTIVITIES OF THE COLD, MASSIVE MOLECULAR CLOUD G216-2.5

A Dissertation Presented

by

YOUNGUNG LEE

Submitted to the Graduate School of the
University of Massachusetts in partial fulfillment
of the requirements for the degree of

DOCTOR OF PHILOSOPHY

September 1992

Department of Physics and Astronomy

STRUCTURE AND STAR FORMING ACTIVITIES OF THE COLD, MASSIVE MOLECULAR CLOUD G216-2.5

A Dissertation Presented

by

YOUNGUNG LEE

Approved as to style and content by:

Ronald L. Snell, ~~Chair~~

Robert L. Dickman, Member

F. Peter Schloerb, Member

Michael F. Skrutskie, Member

Robert V. Krotkov, Outside Member

Robert B. Hallock, Department Head
Department of Physics and Astronomy

To
my wife Juna,
my boy Haesung,
my parents,
and
my parents-in-law

ACKNOWLEDGEMENTS

It has been a great pleasure to have been part of the Five College Radio Astronomy Observatory and University of Massachusetts. FCRAO and Korean Astronomy Observatory have the same design for their radio telescopes, and in that sense, FCRAO is simply the best place for me to learn observing skills as well as astronomical science.

First of all, I would like to thank my adviser Ron Snell, who initiated this project, and supported me throughout my graduate studies. He has been extremely patient to me as I developed basic scientific skills. He has always been kind to me.

My special thanks goes to Bill Irvine, Director of FCRAO, who gave me a chance to study at FCRAO and allocated me huge amounts of observing time, and always said 'yes' when I requested N/A time. I am greatly indebted to him.

My thanks also goes to Bob Dickman, who has always been encouraged me, and suggested many valuable ideas on my work. He showed me how to write a scientific paper in a very careful way. His enthusiasm never died even after I waked him up in the middle of the nights when Modcomp or telescope stopped. I have also annoyed Mike Brewer in many late nights when hardware troubles occurred. He was always patient to my questions and helped me make telescope alive. I can't thank enough for that.

I would like to thank to all the faculties and staffs of FCRAO, who developed and built our wonderful receiver QUARRY. Without QUARRY, I could not have finished my dissertation within five years. I am also grateful to many members of the faculty who leaded me to deeper range of astronomy; in particular Paul

Goldsmith, John Kwan, Ted Harrison, Pete Schloerb, David van Blerkom, Gene Tademaru, and Judy Young. Even if I didn't have a chance to take courses from Steve and Karen Strom, I learned how to dedicate oneself to science from them. Steve has always provided open access to his invaluable journals. I am very grateful for that.

My special thanks is also extended to Mike Skrutskie, John Carpenter, and Mike Meyer. They kindly observed IRAS point sources for me in near-infrared bands at Kitt Peak and San Pedro Martir, Mexico, which are very crucial for studying star forming activities. John also kindly provided the Gem OB-1 data.

I would also like to thank Mark Heyer, who developed the data reduction packages for QUARRY data. Taoling Xie and John Carpenter also provided use of their programs. All the useful scientific discussion with them I can't forget. Lynne Hillenbrand showed me how to perform photometry, and provided data on young stars. German Cortes, and Gene Lauria helped me out of series of UNIX and LaTeX problems. I thank them heartfully.

My deepest appreciation goes to my wife, Juna. She suffered separation from me for a year. Along with her own research work in Florida, she alone has been taking care of our boy, Haesung George. She has always been encouraging me in many ways, and supported me through the years. I guess it's my turn to do so, now. I also thank my parents, my parents-in-law, and brothers and sisters in Korea, who prayed for us, and gave us heartfelt encouragement.

Firstly and finally, many thanks, God ! Now it's time to start another line. Please be with us all the years ahead.

ABSTRACT

STRUCTURE AND STAR FORMING ACTIVITIES
OF THE COLD, MASSIVE MOLECULAR CLOUD G216-2.5

SEPTEMBER 1992

YOUNGUNG LEE

B.S., SEOUL NATIONAL UNIVERSITY, SEOUL, KOREA

M.S., SEOUL NATIONAL UNIVERSITY, SEOUL, KOREA

Ph.D., UNIVERSITY OF MASSACHUSETTS

Directed by: Professor Ronald L. Snell

We have studied the gas and dust properties and the star forming activity in G216-2.5 (also called Maddalena's cloud), a cold, massive GMC that has no evidence for star formation. We have mapped 11 square degrees in the J = 1–0 transitions of ^{12}CO and ^{13}CO using the QUARRY fifteen-beam array receiver on the 14 m telescope at FCRAO. We have confirmed the results of Maddalena and Thaddeus (1985) that the cloud is unusually cold and has very broad linewidths ($\Delta V \sim 8$ km s^{-1}).

The visual extinction to ^{13}CO column density ratio is found to be similar to that in local molecular clouds, suggesting that if the gas to dust ratio is normal, the ^{13}CO abundance relative to molecular hydrogen in this cloud is similar to that found for clouds near the sun.

The low gas and dust temperatures found for this cloud are largely due to the absence of heating by massive stars. The exceptionally low gas temperature can be explained if the cosmic-ray heating rate is reduced by a factor of two in the outer Galaxy.

Low luminosity, and presumably low mass, young stars have been identified in this cloud. These young stars are found preferentially on the edge of the cloud. Clusters of T Tauri stars are found in two locations within G216-2.5.

The mass of the cloud has been established by several techniques, and masses between 1×10^5 and 6×10^5 $M_\odot$ were obtained.

It is suggested that G216-2.5 is a remnant cloud from a past episode of massive star formation for the following reasons. First, the cloud has a relatively large velocity dispersion for a non-star-forming GMC. Second, there is clear evidence for shells and rings within the cloud, which may be the fossil remains of its earlier star formation activity. Third, the kinematics of the cloud is dominated by a global velocity gradient suggesting that the cloud is part of a very large expanding shell. Lastly, the discrepancy between the LTE and virial masses may be explained if the cloud has been severely perturbed and is currently expanding. G216-2.5 may be part of a larger star forming complex that includes the adjacent H II region S287 and its molecular cloud.

Table of Contents

List of Tables

List of Figures

CHAPTER 1

INTRODUCTION

1.1 Background

Giant molecular clouds (GMCs) in our Galaxy are a significant mass component of the interstellar medium. The fundamental goal of the study of molecular clouds is to understand how they evolve from the more diffuse interstellar medium and how they form stars. All present day star formation is believed to be taking place in molecular clouds, so we may think of them as providing the initial conditions for the process of star formation. Yet, while all stars may form in molecular clouds, there are at least some molecular clouds that do not appear to be forming stars. Furthermore, even within those clouds that do form stars, it appears that only a small fraction of the whole mass of a cloud actively participates in the star forming process.

Investigations of GMCs are often biased; usually the clouds selected for study are located near H II regions, OB associations, IR sources, reflection nebulae, or some other recent product of the formation of fairly massive stars. Little attention has been given to clouds that show no conspicuous star-forming activity, although there is evidence that such clouds exist (Maddalena and Thaddeus 1985). Comparing the unbiased Columbia CO survey of distant objects in the inner Galaxy

with far-infrared, radio-continuum, and radio recombination line surveys, Myers *et al.* (1986) showed that the number of young stars that accompany large molecular clouds fluctuates greatly and that some large clouds display little or no evidence of star formation. Using GMCs identified by the Massachusetts-Stony Brook Galactic Plane CO Survey, Solomon and Rivolo (1989) divided them into warm clouds ($T_R^*(\mathrm{peak}) > 7.5$ K) and cold clouds ($5 < T_R^*(\mathrm{peak}) < 7.5$ K). They were unable to present a complete distribution of the cold clouds, since they selected only clouds with $T_R^*(\mathrm{peak}) > 5$ K; however, they could test for trends within the sample itself, by dividing the sample of clouds into 'cold' and 'warm' subsamples. While they did not discuss star formation activities explicitly (although this is a plausible source of the observed temperature difference), Solomon and Rivolo argued that the cooler clouds show less arm-interarm contrast and a flatter radial distribution than the warmer clouds, and have a lower average mass than the warmer ones.

Over the last two decades there have been relatively few studies of the GMCs in the outer Galaxy (Mead and Kutner 1988; Mead, Kutner, and Evans 1990; Sodroski 1991; Digel, Bally, and Thaddeus 1990; and Carpenter, Snell, and Schloerb 1990). However, there are several reasons why their study is needed. First, a comparison of the physical properties of GMCs in the inner and outer Galaxy may enable one to derive information on environmental conditions (such as metallicity, local dust-to-gas ratio, cosmic-ray heating, and cloud-cloud collisions), and on the formation, evolution, and physical properties of the clouds. For example, a low flux of cosmic rays could result in lower gas temperatures in the envelopes of outer Galaxy clouds, or fewer cloud-cloud collisions could result in a reduced star formation rate (Mead

and Kutner 1988). Second, it is also known that a large fraction ($\sim$ 60 %) of the mass of the Galaxy's neutral interstellar medium resides in the outer Galactic disk (Solomon *et al.* 1987; Bloemen 1985). Therefore, more detailed studies of GMCs in the outer Galaxy are essential to acquire a more complete understanding of the interstellar medium. Sodroski (1991) recently derived physical properties for 35 GMCs and GMC complexes in the outer Galaxy, including G216-2.5, using the Columbia ^{12}CO survey of the Galactic plane. However, the spatial resolution of the data were not sufficient to provide a detailed analysis of the cloud structure, nor adequate to be certain that several clouds were not blended into one. Higher resolution mapping is therefore needed to obtain an unambiguous picture of the clouds in the outer Galaxy.

1.2 A Cold, Massive Molecular Cloud, G216-2.5

A large molecular cloud at galactic coordinates, $l = 216.°5$, $b = -2.°5$ was identified in the Columbia survey of the third quadrant of the Galaxy by Maddalena and Thaddeus (1985: hereafter, we call this cloud G216-2.5). Based on the ^{12}CO and radio continuum data, they suggested that the cloud may be relatively young and had not yet extensively formed stars. The cloud was estimated to have a mass of $\sim 10^6$ $M_\odot$ and was distinguished by being very cold, with no signs of recent star formation. However the resolution of the Columbia survey (8.′7 beamwidth) was not adequate to determine the structure of the cloud, and no higher resolution

observations in any molecular species have been published, leaving unresolved the extent with which this cloud differs from other GMCs.

The outer Galaxy is not warped at this location (Henderson, Jackson, and Kerr 1982), so the cloud's Galactic latitude probably corresponds to a true displacement from the galactic midplane. At the distance to the G216-2.5 ($d \simeq 2.2$ kpc; Chapter 3), this displacement is 100 pc, or a little larger than the half-thickness at the half-maximum of molecular material at the solar circle (Thaddeus and Chanan 1985).

POSS prints at the location of the cloud show a slight hint of optical obscuration, which is consistent with the cloud's large distance and with many observable stars in the foreground. There is also an H I enhancement (Weaver and Williams 1973) toward the cloud, and an excess of gamma-ray emission which cannot be entirely accounted for by the interaction of cosmic rays and the gas implied by the 21 cm observations (Bloemen *et al.* 1984). There is also slight enhancement in the continuum at 408 MHz toward the cloud (Haslam *et al.* 1981).

The cloud is not a strong source of FIR emission. All the previous infrared sources (before IRAS point sources were released) have been attributed to nearby stars (Maddalena and Thaddeus 1985). If H II regions or OB stars existed on the near side of the cloud, they should be readily visible as the cloud itself is optically visible. In addition, S287, which lies near G216-2.5, should have similar foreground obscuration and is readily visible. There are no H II regions of OB stars toward this cloud in the standard catalogs (Sharpless 1959; Humprey 1978; and Blitz, Fich, and Stark 1982). Weak FIR emission is found associated with G216-2.5 in this work,

however, the emission is much weaker than found in other star forming GMCs (Blitz 1991). FIR emission at 100 μm is well matched with the ^{12}CO emission of the cloud, although the upper region of the cloud is severely contaminated by background emission from the H II region S286, which lies substantially behind G216-2.5.

1.3 Scientific Objectives

The objective of this study is to understand the nature of the cold and massive cloud G216-2.5 by mapping the molecular gas with high ($\sim$ 50″) resolution and full sampling, and to probe its star forming activity through far-infrared and near-infrared observations. To address these issues, we proceeded as follows.

While studies of the relationship between ^{13}CO column density and visual extinction have been used to establish the ^{13}CO abundance in local dark clouds, such studies have seldom been attempted for more distant clouds. We have made star count measurements and determined the ^{13}CO abundance for G216-2.5.

The ^{12}CO emission can be used to estimate the gas kinetic temperature and can be combined with ^{13}CO to determine the gas column density. The temperature of G216-2.5, hydrogen molecule density, and dust temperature were compared with the properties of other GMCs. Cloud kinematics were also analyzed and compared with the high-mass star forming clouds. The hope is that a detailed analysis of these physical parameters and comparison with other GMCs will provide a substantial

information on molecular clouds, and ultimately, on the evolution of molecular clouds.

Another major question to be addressed is why G216-2.5 is not forming massive stars. So far, no evidence for star formation of any kind has been reported; however, IRAS has identified a number of point sources in the direction of this cloud, which may be young stars. We investigated these sources in detail and imaged them at high angular resolution in the near-infrared J, H, and K bands. These near-IR images permit us to search for embedded T-Tauri stars, even at the distance of this cloud.

Together, these results are the first high resolution observations of a cold, massive cloud in the outer Galaxy. The results of this study should yield a substantial information on such objects, and will extend our knowledge of GMCs which have either evolved differently from most clouds in the solar neighborhood or which are in a much earlier or later stage of their development.

The outline of the remainder of this work is as follows. In Chapter 2 we present data acquisition and reduction procedures. This includes molecular line data, far-infrared data, and near-infrared imaging. Chapter 3 presents the determination of distance to this cloud, and describes the star counting technique used to obtain the relation between visual extinction and ^{13}CO column density. In Chapter 4 the molecular line data are analyzed, concentrating especially on the determination of temperature, density, kinematics, and mass of the cloud. A radiative transfer model is also introduced to check the validity of the standard LTE assumptions. The main focus of Chapter 5 is the emission from the dust at far-infrared wavelengths. Star

forming activities are investigated in Chapter 6 through near-infrared imaging. In Chapter 7 all the above results are combined and discussed, including a discussion of the evolutionary status of G216-2.5. A summary of this dissertation is presented in Chapter 8.

CHAPTER 2

OBSERVATIONS AND DATA REDUCTIONS

2.1 Millimeter-Wave Observations

2.1.1 ^{12}CO and ^{13}CO Observations

Maps of the G216-2.5 cloud have been obtained in the J = 1–0 transitions of ^{12}CO and ^{13}CO using the QUARRY fifteen-beam array receiver at the FCRAO 14 m radio telescope between February 1991 to February 1992. Spectra obtained were spaced by 50″, and covered $\sim$ 11 square degrees from $l = 214°$ to 218°.5, and from $b = -1°$ to $-4.5°$. Each map consists of 57,300 spectra, or 3,820 pointings of the telescope. Two filterbanks with thirty-two channels, with frequency resolutions of 250 KHz, and 1 MHz were used for each beam. A velocity coverage of 21 km s^{-1} and the resolution of 0.65 km s^{-1} is provided with 250 KHz filterbank at the frequency of the ^{12}CO $J = 1 - 0$ line. This filterbank provides adequate velocity coverage for G216-2.5. The 1 MHz filterbank provides a velocity coverage of 85 km s^{-1} with a resolution of 2.6 km s^{-1}, and used for checking if emission at other velocities were detectable in this direction. The QUARRY fifteen-beam receiver (Erickson *et al.* 1992) provides a powerful means to map a substantial area of the sky with high sampling rate in a relatively short time.

To achieve an rms noise level of 0.25 K and 0.15 K in ^{12}CO, and ^{13}CO, respectively, on-source integration times of 30 to 90 seconds for ^{12}CO, and 60 seconds to 180 seconds for ^{13}CO were required, depending on the weather conditions. The ^{12}CO system temperature was typically 700 to 1100 K; however, data were taken at temperatures as high as 1300 K. The ^{13}CO system temperature ranged from 500 K to 800 K. All observations were made by position switching to one of several reference positions confirmed to have no CO emission. Each reference observation was shared with observations of 4 to 8 map positions, depending on the sky stability. Calibration was accomplished by frequently observing an ambient temperature load. All antenna temperatures quoted are corrected for atmospheric extinction and for the forward spillover and scattering losses of the antenna and radome (η_{fss} = 0.7 at 110 to 115 GHz), and are therefore on the $T_{\rm R}^{*}$ temperature scale defined by Kutner and Ulich (1981). The observations required 75 hours for the ^{12}CO map, and 105 hours for the ^{13}CO map. The final average rms noise of the data was 0.3 K in ^{12}CO and 0.16 K in ^{13}CO($T_{\rm R}^{*}$). All data were spatially smoothed to a resolution of 120″, however no velocity-smoothing was done. After spatial smoothing, the rms noise in the ^{12}CO data was reduced to 0.09 K, and 0.05 K for ^{13}CO.

Between December 1989 and February 1990 preliminary observations were conducted toward a region of strong ^{12}CO emission, identified in the map of Maddalena and Thaddeus (1985) to determine ^{13}CO column density, and to correlate it to the visual extinction. A 0.25 square degree region centered on l = 216.°45 to 216.°95, b = −2.°45 to −2.°95 was mapped in the J = 1–0 transition of both ^{12}CO and ^{13}CO using a single-beam 3 mm receiver on the 14 m telescope. The

sampling rate was 1′ and the FWHM beam size was 45″ at 115.27 GHz and 47″ at 110.2 GHz. All observations were made by position switching between the observed positions and a reference position located at $l = 216.°5$, $b = -4°$. Each reference observation was shared with observations of four positions within the map. A 256 channel filterbank with a spectral resolution of 250 kHz was used, which provided a resolution of 0.65 km s^{-1} at the frequency of ^{12}CO. The data were smoothed and resampled at 1 km s^{-1} resolution. The rms noise ($T_{\rm R}^{*}$) of the 0.25 square degree region mapped was 0.28 K and 0.18 K in ^{12}CO and ^{13}CO, respectively. The spectra obtained from two observation runs with the single-beam receiver and the QUARRY fifteen-beam array receiver are consistent within ± 5 %.

Two H II regions lie near G216-2.5: S287 and S286. The $V_{\rm LSR}$ of the ^{12}CO emission toward S286 (this is also IRAS point source 06520-0428; see below and Table 2.1) is 50 km s^{-1}, substantially different from the velocity of the emission in G216-2.6. The velocity of the emission in S287 is $V_{\rm LSR} = 27$ km s^{-1}, which is the same as that of G216-2.5. More extended CO mapping of S287 was conducted to check its possible association with G216-2.5. A 2.4 square degree region centered on the position of the S287 H II region ($l = 218°.1$, $b = -0°.4$) was mapped in ^{12}CO J = 1–0 with the QUARRY fifteen beam array receiver on June 1992. A 0.8 square degree was mapped in ^{13}CO J = 1–0, which encompasses most of ^{12}CO emission. The mapping procedure was the same as for G216-2.5. The average rms noise of the data was 0.38 K in ^{12}CO, and 0.21 K in ^{13}CO.

Five IRAS point sources with flux densities > 15 Jy at 100 μm are located within ~ 1 degree of the boundary of the main body of the cloud, but were not

included in the main observation of G216-2.5. Additional ^{12}CO observations were conducted toward these sources to check for any possible connection with G216-2.5. These sources are listed in Table 2.1 along with their Galactic coordinates, and FIR flux densities in units of Janskys (1 Jansky = 10^{-26} W m^{-2} Hz^{-1}). The 12 μm, fluxes followed by an 'L' represent lower limits. The eighth column in Table 2.1 is the $V_{\rm LSR}$ of the CO emission observed toward the IRAS sources, when detected, and the last column is the peak temperature of the CO emission on the $T_{\rm R}^{*}$ scale. Among these sources is the H II region S286 (IRAS point source 06412-0105), which is located just above the main body of the cloud and which has a substantial FIR flux. The distance of S286 is estimated to be 4.8 kpc, and lies far beyond S287 (Blitz, Fich, and Stark 1982) and G216-2.5. Weak ^{12}CO emission was detected toward two other IRAS point sources, but the velocities are much higher than that of G216-2.5 and they are unlikely to be associated.

Table 2.1 Table of IRAS point sources located within 1 degree of G216-2.5 boundary, which are observed in ^{12}CO J = 1–0.

Name	l	b	S_{12}	S_{25}	S_{60}	S_{100}	V_{LSR}	T_{pk}
06356-0139	213.09	-2.22	2.76	4.28	61.10	109.25	52	3 K
06404-0414	215.78	-3.85	0.25L	0.24	6.67	25.47	-	-
06450-0619	218.18	-3.77	0.25L	0.25	5.57	16.52	-	-
06412-0105	213.06	-2.23	13.92	159.11	612.03	532.55	52	4 K
06520-0428	217.32	-1.37	1.59	2.88	32.76	132.60	50	6 K

2.1.2 *CS, $C^{18}O$, HCO^+ Observations*

The three brightest ^{13}CO emission regions were observed in the CS J = 2–1 transition, the $C^{18}O$ J = 1–0 transition and the HCO^+ J = 1–0 transition (Table 2.2). Two of these regions are toward IRAS point sources, which were also imaged in the near-infrared, and $C^{18}O$, HCO^+, and CS emission was detected in all three regions. A $13' \times 15'$ region centered on $l = 216.75$, $b = -2.65$ was mapped in the CS J = 2 - 1 transition. A smaller region $4'.2 \times 5'$ in extent was observed in HCO^+, and $C^{18}O$J = 1–0. Typical system temperatures were 350 K - 500 K. The average rms noise (T_R^*) for these observations is $\sim$ 0.07 K. The results of these observations are tabulated in Table 2.2.

Table 2.2 List of positions observed in CS (J = 2–1), $C^{18}O$ (J = 1–0), and HCO^+ (J = 1–0).

l	*b*	*Size*	CS(2–1)	HCO^+ (1-0)	$C^{18}O$	^{13}CO	*IRAS Name*
216.75	-2.65	$13' \times 15'$	0.3	0.1	0.2	2.0	-
214.49	-1.81	$4'.2 \times 5'$	0.4	0.7	0.4	2.3	06453-0209
216.79	-1.04	$4'.2 \times 5'$	0.2	0.1	0.1	4.3	06522-0350

2.2 Far-Infrared Data

2.2.1 *IRAS Point Sources*

A sensitive probe for any embedded stellar objects and of the extended dust emission is the IRAS all sky infrared survey. The IRAS survey was carried out

between January and November 1983. The limiting sensitivity in unconfused regions is roughly 1 Jy at all four bands. To investigate possible star forming sites, all sources in the IRAS Point Source Catalogue within the mapped boundary were selected. They are tabulated in Table 2.3 All have a flux density at 100 μm greater than 13 Janskys. The 10 IRAS point sources found within the boundary of the CO emission from G216-2.5 are marked with asterisks.

Table 2.3 IRAS point sources toward G216-2.5.

Name	l	b	S_{12}	S_{25}	S_{60}	S_{100}
06453-0209*	214.49	-1.81	1.12	6.10	22.21	36.86
06522-0350*	216.79	-1.04	1.45	3.56	23.12	69.62
06471-0329*	215.89	-2.01	1.82	6.46	15.85	23.79
06481-0517*	217.60	-2.62	1.51	7.58	20.06	32.05
06416-0352*	215.60	-3.41	0.74	1.02	10.63	26.11
06428-0257*	214.93	-2.72	1.08	1.40	17.28	38.41
06471-0353*	216.24	-2.19	0.50	0.54	7.38	26.24
06492-0349*	216.43	-1.72	0.27	0.47	9.82	30.56
06507-0519*	217.93	-2.07	0.58	0.53	8.31	31.26
06401-0318*	214.92	-3.48	0.54	0.59	10.74	36.77
06404-0414	215.78	-3.85	-0.25	0.24	6.67	25.47
06405-0356	215.53	-3.67	0.31	0.65	4.38	13.75
06424-0237	214.58	-2.67	0.67	0.75	4.69	13.76
06435-0153	214.06	-2.09	-0.25	0.47	8.80	27.00
06450-0619	218.18	-3.77	-0.25	0.25	5.57	16.52
06452-0601	217.93	-3.60	0.52	0.85	6.79	18.48
06486-0110	214.02	-0.61	0.48	0.54	5.88	23.50
06514-0424	217.19	-1.50	0.52	0.45	4.46	15.44
06519-0424	217.26	-1.38	0.45	0.41	6.80	39.85
06520-0428	217.32	-1.37	1.59	2.88	32.76	132.60

2.2.2 *Big Map Images*

While information on star formation activity can be extracted from the IRAS Point Source Catalog, we have also acquired $8° \times 8°$ BIGMAP images in all four IRAS bands centered on the position of G216-2.5 from Infrared Processing and Analysis Center. The $8° \times 8°$ area also includes S287. A 100 μm image of this region is presented in Figure 2.1. The G216-2.5 region is outlined by a large box, and S287 is outlined by the smaller box. One bright spot within the large box at $\alpha = 06^h20^m$, $\delta = -04°28'$ represents S286, which is not associated with G216-2.5. Only the regions within these two boxes were extracted at all four IRAS wavelength bands to study the extended emission from the dust. These maps are presented in Figure 2.2–2.5. At 12 and 25 μm, there appears to be little emission associated with G216-2.5.

There are two main sources of contamination of the far-infrared data; zodiacal emission and the background Galactic emission. In the BIGMAP images the zodiacal emission is believed to have been effectively removed, and the region lies sufficiently far away from the ecliptic ($\sim$ 25 degree from ecliptic plane), that contamination by zodiacal light may never be large.

The identification of the far-infrared emission (FIR) from G216-2.5 would be straightforward if the cloud was well isolated. Spatial coincidence and close morphological similarity is found between the CO emission for isolated clouds, especially after subtraction of the extended Galactic FIR emission (Heyer *et al.* 1987; Langer *et al.* 1989; and Mooney 1992). In regions of the Galactic plane where there are substantial overlap of molecular clouds along the line of sight, however, it is much more

difficult to extract the FIR emission from individual clouds. G216-2.5 is located just below (100 pc) the Galactic plane. In Figure 2.6 a contour map of the 100 μm flux is overlayed on the ^{12}CO integrated intensity grey scale map. As presented in Figure 2.6, the upper part of the cloud close to the Galactic plane is contaminated by the emission from a more distant H II region S286 at $l = 217°.3, b = -1°.4$. The emission from G216-2.5 is also blended with the emission from the dust associated with S287 at $l = 218°.1, b = -0°.4$. The lower part of G216-2.5, between $b = -3°$ and $b = -4°$, however, is thought to be almost free of contamination from other sources and the emission corresponds well with the map of the CO integrated intensity of the cloud (see Figure 2.6). FIR emission from the satellite cloud centered on $l = 214°.5, b = -1°.7$ is also obvious.

2.3 Near-Infrared Imaging

The poor angular resolution of the IRAS observations makes the identification of individual low luminosity stars difficult. Optical images of the IRAS sources with arcsecond resolution can be obtained, but the high levels of visual extinction in the cloud would prevent the detection of associated young stars. However, the extinction at near-infrared wavelengths is up to an order of magnitude lower than at the visual wavelengths and thus, such observations will be more sensitive to an embedded population of stars. Even at a distance of 2.2 kpc, it is possible to detect embedded populations of low mass stars in the near infrared. Nine IRAS

point sources have been imaged at J, H, and K bands marked with asterisks in Table 2.3.

Near-infrared observations were conducted at two observatories; Kitt Peak National Observatory and Observatorio Astronomical Nacional, San Pedro Martir, Baja California, Mexico. Seven IRAS sources, which are located in the main body of G216-2.5, were observed at J, H, and K bands with a 58×62 array on the 1.5 m telescope at the Kitt Peak National Observatory in February 1991. The Kitt Peak data has an angular resolution of $1''.35$ per pixel. To improve our photometric accuracy, adjacent images of the nine frames in the mosaic were overlapped by 1/3 of a frame so that many of the stars would be observed more than once. The region mosaicked around each source has an angular extent roughly $3'.3 \times 3'.3$. The standard star HD40335 was observed to provide photometric calibration.

The two brightest IRAS sources were observed with the 64×64 element UMass HgCdTe array with a platescale of $0''.8$ per pixel on the 2.1 m telescope at Observatorio Astronomical Nacional, San Pedro Martir, Mexico in January 1992. Mosaics were made at K-band in a 3×3 frame grid centered on the IRAS sources. Only one frame was obtained at J and H bands centered for each source. The standard star HD22686 was observed at least three times to improve the photometric accuracy.

2.3.1 Data Reduction Procedure of NIR Imaging

For the Kitt Peak data, flat fields were obtained by median filtering the mosaicked frames, and subtracting the appropriate dark current image. Median filtered mosaic frames also served as source-free reference frames for background

subtraction. Total exposure times were 60 seconds per frame at J, H, and K bands. For the San Pedro data, J and H frames were flat-fielded and linearized by combining standard star frames, and flat fields were obtained by median filtering the mosaic frames in K band, and subtracting the appropriate dark current. Exposure times were 90 seconds per frame in all bands.

As some of fields are relatively crowded, we used the DAOPHOT data reduction package to obtain photometry for the all the 9 fields which were observed. An aperture radius of 3 pixels (4″) was used, which included most of the light from a point source at all three wavelengths. The sky background was computed from the mode of the distribution in an annulus that extended from a radius of 15 pixels to 19 pixels. The instrumental magnitudes for the standards stars (HD40335 and HD22686) were consistent to within 3% throughout each observing run. The completeness limit of the photometry was estimated by computing the rms noise of the pixels within a radius of 14 pixels over an emission-free region of the sky-subtracted, flat-fielded reference field and by assuming that the minimum detection is 5σ. Based on this assumption, the detection limit are 16.0, 15.2, and 14.8 magnitude at J, H, and K, respectively for the Kitt Peak data and 16.1, 15.6, and 15.0 magnitude, for the San Pedro Martir data.

One source of photometric error in the Kitt Peak data is due to tracking errors. Thus some images show elliptical shapes instead of circular shapes. This made it difficult to build a good point spread function. By iterating the process of building the point spread function, we were able to reduce the measuring errors. All photometric measurement with estimated errors less than magnitude were used.

The typical uncertainty in the photometry was $0.1 \sim 0.2$ magnitude in all three bands.

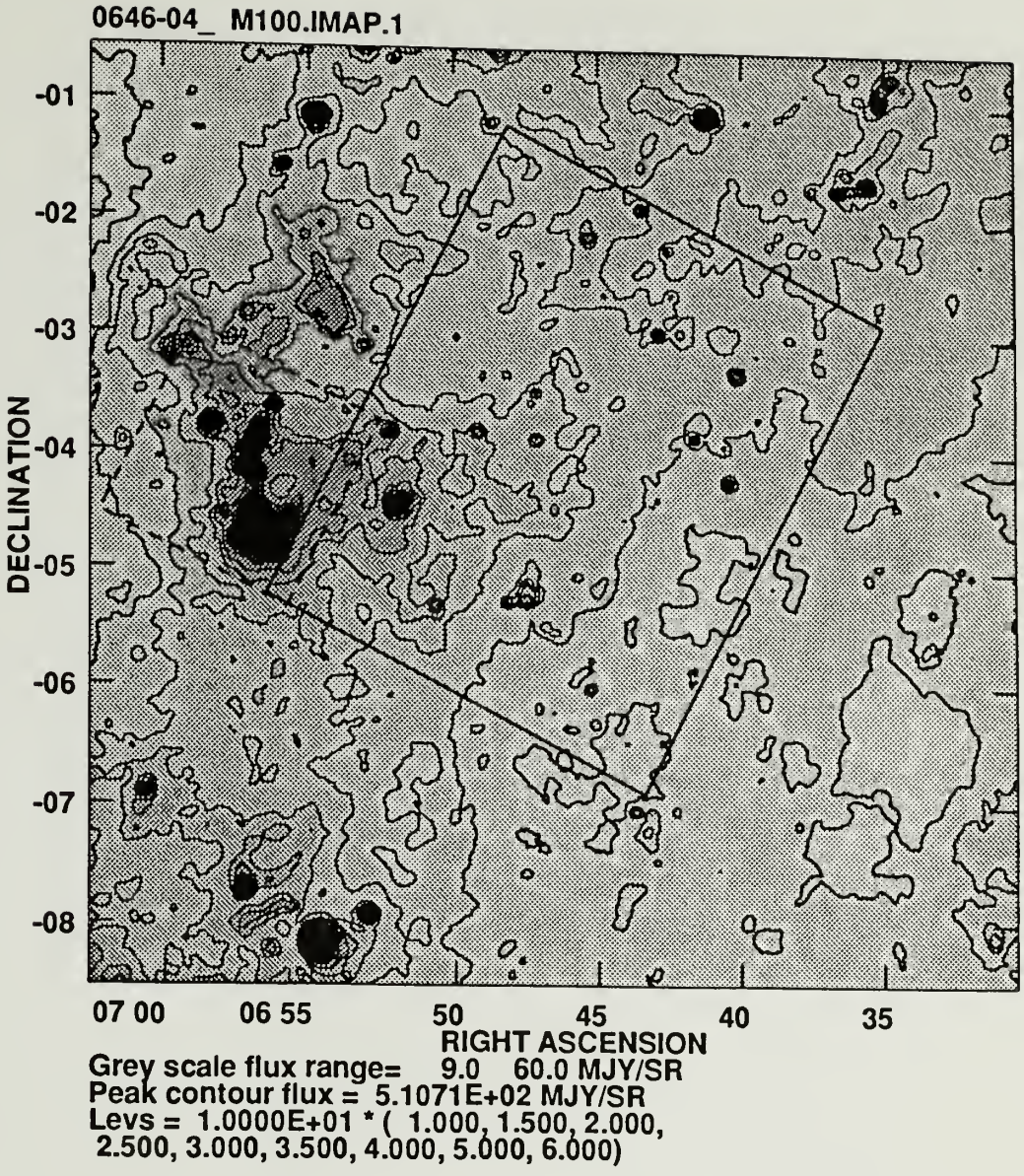

Figure 2.1 The 100 μm BIGMAP image of an 8° × 8° region centered on G216-2.5. The location of G216-2.5 is marked with solid-outlined box. The smaller dashed-outlined box indicates the position of the S287 H II region. The lowest contour level is 10 MJy/sr, and the increment between levels is 5 MJy/sr.

Figure 2.2 A 12 μm intensity image around G216-2.5. The lowest contour level is 2.2 MJy/sr, and the increment between levels is 0.195 MJy/sr.

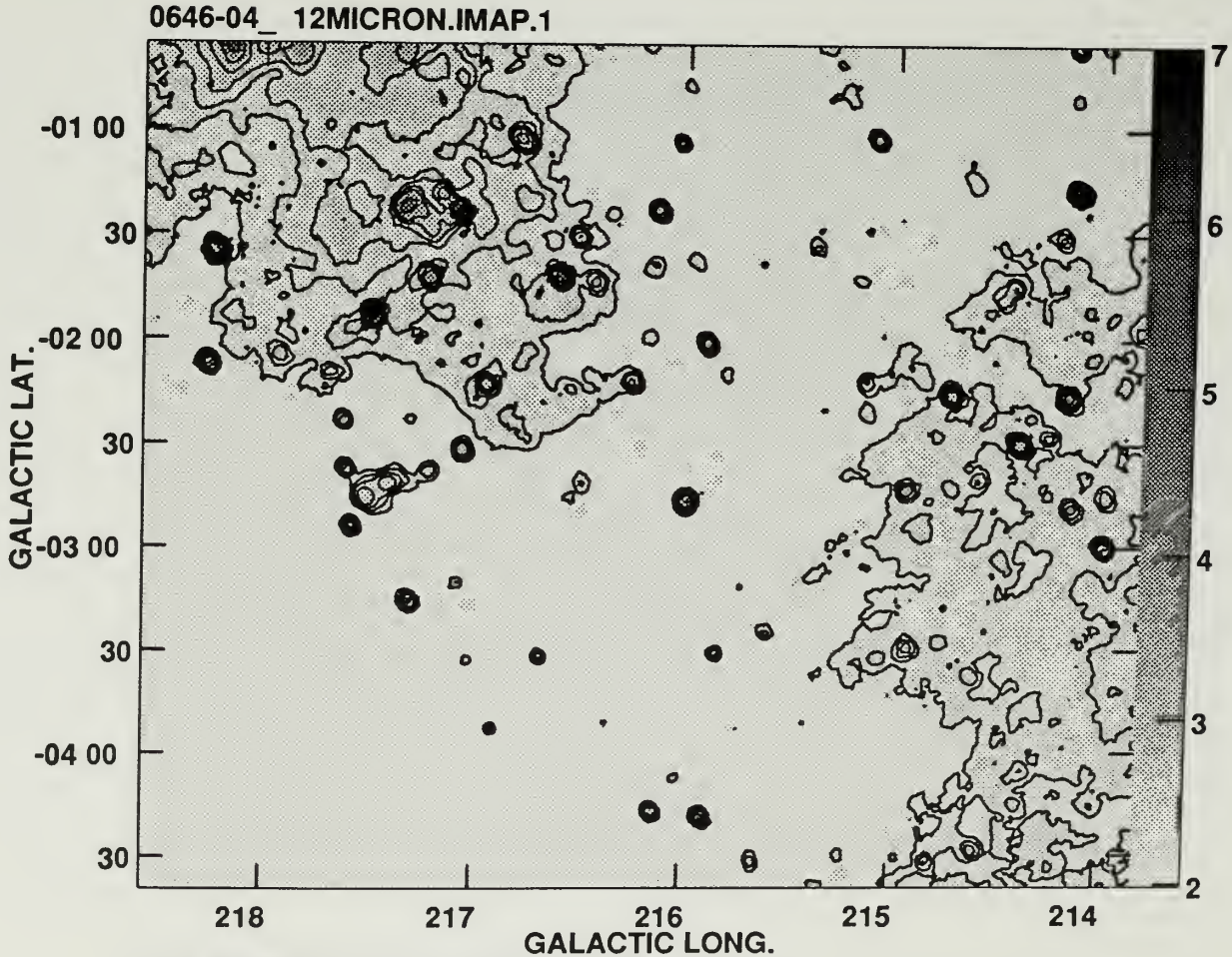
0646-04_ 12MICRON.IMAP.1
-01 00
30
-02 00
30
-03 00
30
-04 00
30
GALACTIC LAT.
218
217
216
215
214
GALACTIC LONG.
7
6
5
4
3
2
Grey scale flux range= 2.000 7.000 MJY/SR
Peak contour flux = 1.1392E+01 MJY/SR
Levs = 1.3000E+00 * (1.700, 1.850, 2.000,
2.200, 2.500, 3.000, 4.000)

Figure 2.3 A 25 μm intensity image around G216-2.5. The lowest contour level is 4.25 MJy/sr, and the increment between levels is 0.375 MJy/sr.

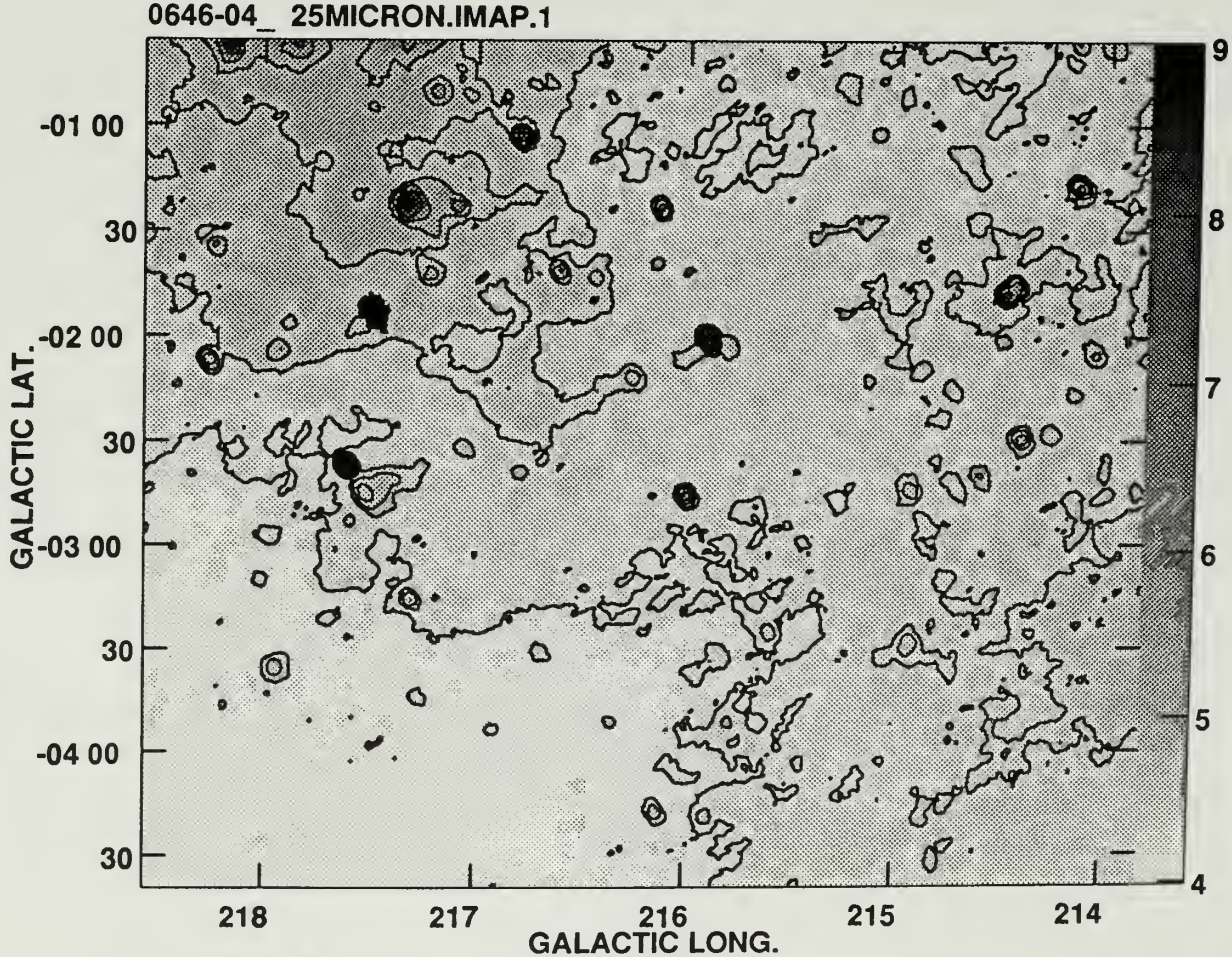
0646-04_ 25MICRON.IMAP.1
-01 00
30
-02 00
30
-03 00
30
-04 00
30
GALACTIC LAT.
218
217
216
215
214
GALACTIC LONG.
9
8
7
6
5
4
Grey scale flux range= 4.000 9.000 MJY/SR
Peak contour flux = 1.4751E+01 MJY/SR
Levs = 2.5000E+00 * (1.700, 1.850, 2.000,
2.200, 2.500, 3.000, 4.000)

Figure 2.4 A 60 μm intensity image around G216-2.5. The lowest contour level is 2 MJy/sr, and the increment between levels is 1 MJy/sr.

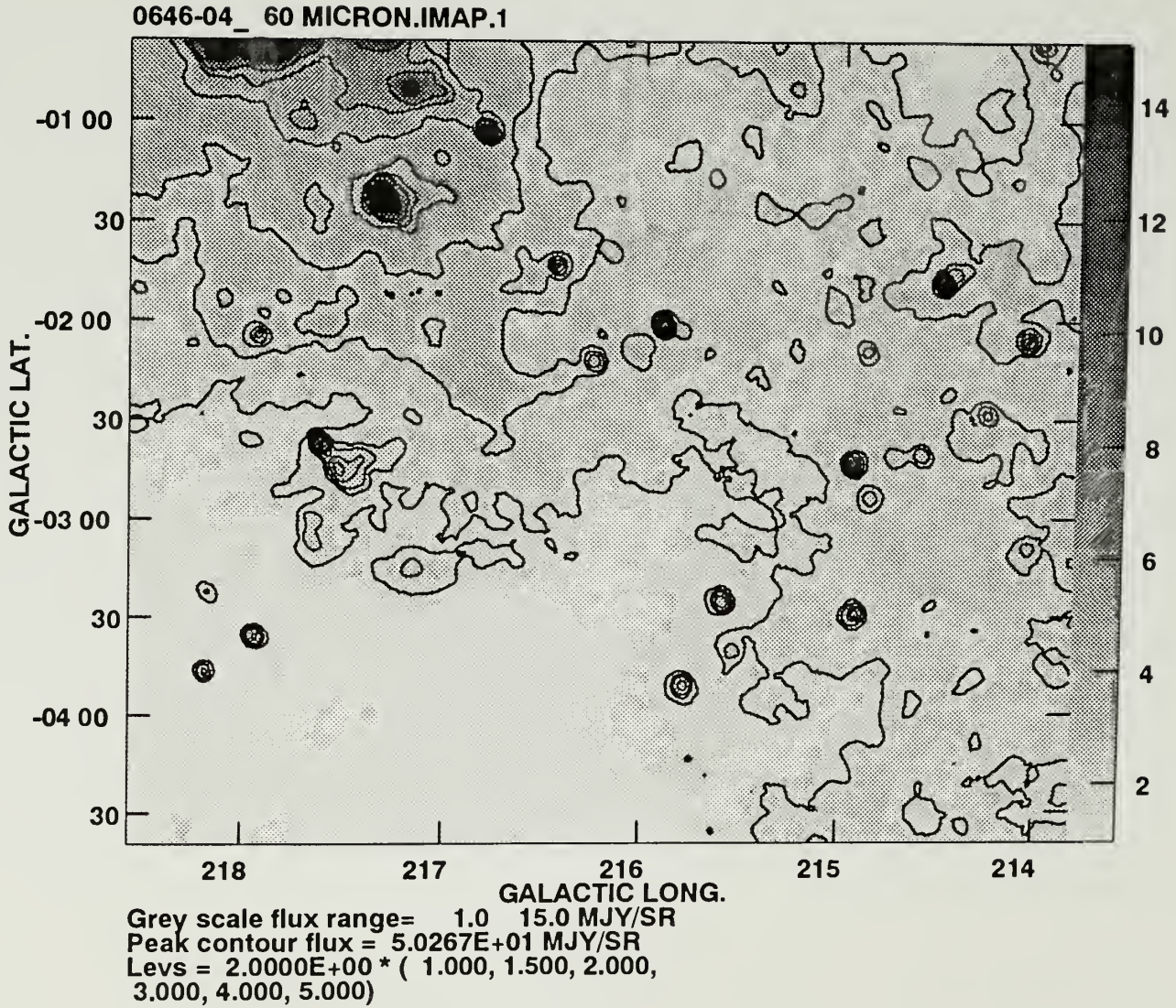
0646-04_ 60 MICRON.IMAP.1
-01 00
30
-02 00
30
-03 00
30
-04 00
30
GALACTIC LAT.
218
217
216
215
214
GALACTIC LONG.
14
12
10
8
6
4
2
Grey scale flux range= 1.0 15.0 MJY/SR
Peak contour flux = 5.0267E+01 MJY/SR
Levs = 2.0000E+00 * (1.000, 1.500, 2.000,
3.000, 4.000, 5.000)

Figure 2.5 A 100 μm intensity image around G216-2.5. The lowest contour level is 20 MJy/sr, and the increment between levels is 5 MJy/sr.

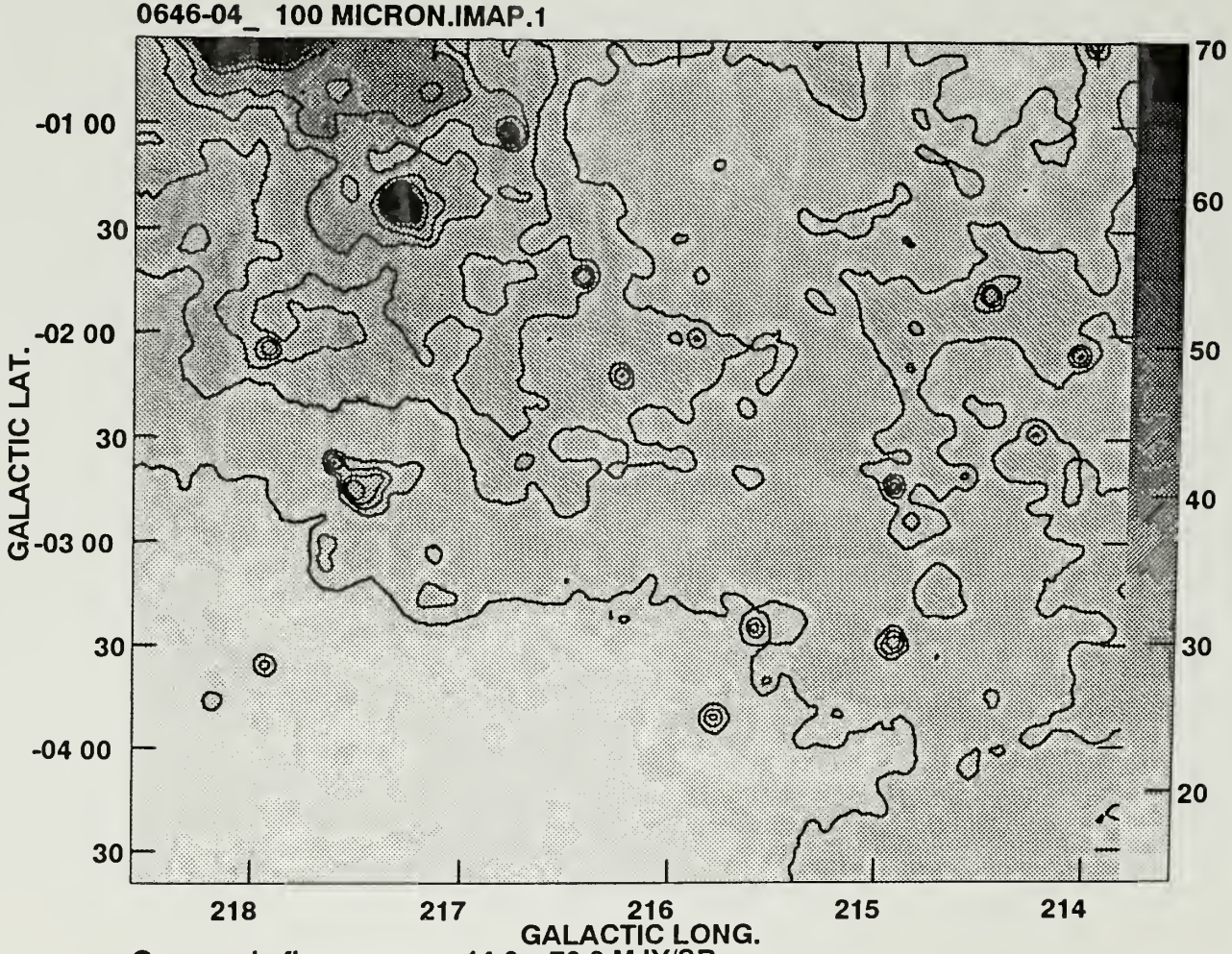

Grey scale flux range= 14.0 70.0 MJY/SR
Peak contour flux = 1.4471E+02 MJY/SR
Levs = 1.0000E+01 * (2.000, 2.500, 3.000,
3.500, 4.000, 5.000, 6.000, 7.000)

Figure 2.6 A contour map of the 100 μm intensity overlayed on a grey-scale image of the ^{12}CO integrated intensity. The contour levels for the 100 μm intensity are the same as Figure 2.5.

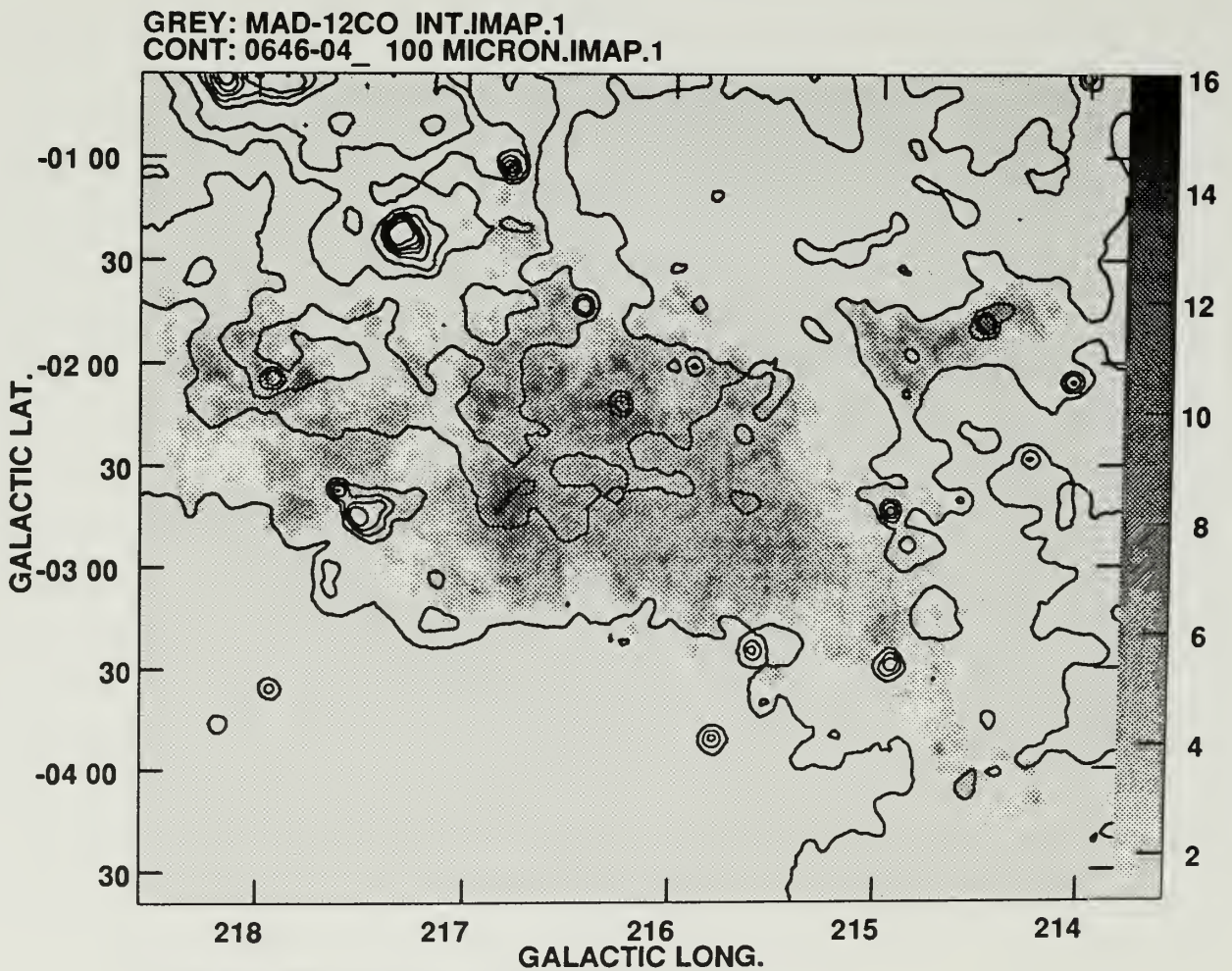
GREY: MAD-12CO INT.IMAP.1
CONT: 0646-04_ 100 MICRON.IMAP.1
-01 00
30
-02 00
30
-03 00
30
-04 00
30
GALACTIC LAT.
218
217
216
215
214
GALACTIC LONG.
16
14
12
10
8
6
4
2
Grey scale flux range= 1.2 16.0 K
Peak contour flux = 1.4471E+02 MJY/SR
Levs = 1.0000E+01 * (2.000, 2.500, 3.000,
3.500, 4.000, 5.000, 6.000, 7.000, 8.000,
10.00)

CHAPTER 3

STAR COUNTS AND DISTANCE DETERMINATION

3.1 Introduction

Knowledge of the CO isotope abundances in the interstellar medium is valuable in delineating the structure of molecular clouds and calculating their masses. Many efforts have been devoted in the last decade to the determination of the CO abundance (Encrenaz *et al.* 1975; Dickman 1978a; Frerking *et al.* 1982; Duvert *et al.* 1986; Cernicharo and Guélin 1987). Unfortunately, these studies have yielded results only for the immediate Solar neighborhood, and their universality - frequently assumed - has yet to be demonstrated. Generally, the column densities of the CO isotopes are calculated from observations of the millimeter wavelength rotational transitions using simple radiative transfer models. A detailed comparison between CO column density and visual extinction (A_V) can then be made when A_V has been determined over large portions of the same cloud. While in local clouds, straightforward star counts from photographic plates suffice to derive the visual extinction with a spatial resolution comparable to that of radio observations, the technique has seldom been attempted for more distant clouds. Using the density function in the Galactic plane (Herbst and Sawyer 1981) to estimate the number of foreground

stars, we are able to apply the star count method to the relatively distant cloud G216-2.5, and determine the visual extinction. By combining these results with our CO maps we can study the carbon monoxide abundance of the cloud.

3.2 Star Counts

The basic procedure used for the star counts follows that given by Bok and Cordwell (1973), and Dickman (1975, 1978b). Star counts were made by superimposing a transparent grid ('reseau') with rulings every $2.'2 \times 2.'2$ (2 mm × 2 mm) on the Palomar Observatory Sky Survey red print. Stars were counted in each grid element of a 0.25 square degree region centered on $l = 216°.7, b = -2°.7$ using a 30× microscope. Red and blue prints of three reference fields were counted at adjacent positions, in order to determine a fiducial star density. All stars in a given reseau square were counted, with no attempt to sort them into magnitude intervals based upon image size. We repeated the counts twice to check for counting consistency. Positioning and alignment errors were minimized by several procedures utilizing computer-generated transparent plate overlays, and it is estimated that as a result of these precautions the error in the location of any reseau square is less than $0.'2$. The extinctions for each square derived from the star counts are computed relative to the nearby reference fields. The presence of any residual obscuration in the reference fields leads to a systematic underestimate of the background stars and thus, of cloud extinction.

3.3 Distance Determination

An accurate distance determination is important for estimating the number of foreground stars used for deriving the cloud extinctions, and for estimating cloud parameters, such as size, mass, and luminosity. Kinematic distances of 2.7 and 2.14 kpc have been estimated for G216-2.5 by Maddalena and Thaddeus (1985) and Sodroski (1991); the differences arise due to the use of slightly different rotation curves and cloud radial velocities. However, due to uncertainties in the rotation curve in the outer Galaxy, the fact that the cloud lies near the anti-center, and the random motions of clouds, the distance to G216-2.5 is not well established by kinematics.

Using a model of the Galactic radial velocity field (Feitzinger and Spicker 1987), Neckel *et al.* (1989) obtained a distance of 2.3 kpc for the H II region/molecular cloud, S287 (or NS14), which is located close to G216-2.5; the H II region has a radial velocity based on its CO emission nearly identical to G216-2.5. They also estimated a photometric distance of 2.1 kpc for S287. The agreement between the radial velocities of G216-2.5 and the molecular cloud associated with the H II region suggests the two are at the same distance.

Another method for estimating distance is based on the reddening of bright stars (see, for example, Snell 1981). Given MK spectral types, visual magnitudes, and $(B - V)$ colors for the stars in the vicinity of a cloud, one can calculate their color excess, E_{B-V}, and distance, based upon the intrinsic color $(B - V)_o$ and absolute magnitude associated with their spectral type and luminosity class. Figure 3.1 shows a plot of color excess versus distance for 42 stars in the vicinity of

G216-2.5; since MK spectral data and colors are available for only a rather limited number of stars from the Kennedy and Buscombe Catalogue (1977), quite a large area ($7.°5 \times 6°$) had to be employed to obtain this sample. Figure 3.1 shows that at a distance of approximately 2 kpc there is a rapid rise in the visual extinction.

In consideration of the uncertainties the distances are all in reasonable agreement. By combining all the above estimates, we thus adopt 2.2 kpc as the distance of G216-2.5.

3.4 CO Column Density

The column density of ^{13}CO at each map position may be estimated from our observations of the ^{12}CO and ^{13}CO line temperatures and from the linewidth of the ^{13}CO emission, assuming LTE (Dickman 1978a; Penzias 1975). When both ^{12}CO and ^{13}CO lines have been observed toward each line of sight, the ^{13}CO column density can be determined. All data used for estimating ^{13}CO column density were obtained using single beam receiver at the FCRAO 14 m telescope. A detailed description of the observations was presented in Chapter 2. The assumptions inherent in this technique are: (1) ^{12}CO is optically thick, (2) the molecules along the line of sight possess a uniform excitation temperature (3) the excitation temperature of the two isotopic species are equal (This assumption will be addressed in more detail in Chapter 4) and (4) the cosmic background radiation is not important. With these assumptions, the common excitation temperature T_{ex} can be obtained from the peak ^{12}CO antenna temperature. The column density of ^{13}CO in the i-th

pixel of a cloud is given:

$$N(^{13}CO)_i = \frac{2.42 \times 10^{14} \Delta V_i \, T_{ex} \, \tau^{13}}{1 - \exp[-5.29/T_x]} \quad [\mathrm{cm}^{-2}], \tag{3.1}$$

where ΔV_i is the full width at half-intensity in km s^{-1}, τ^{13} is the line center optical depth of ^{13}CO , and T_{ex} is the excitation temperature;

$$\tau^{13} = -\ln\left[1 - \frac{T_R^{13}}{\frac{5.29}{e^{5.29/T_{ex}}-1} - 0.93}\right], \tag{3.2}$$

$$T_{ex} = \frac{5.53}{\ln[1 + \frac{5.53}{T_R^{12}+0.876}]}. \tag{3.3}$$

The above equation was used for all the pixels with emission in ^{13}CO greater than the 3 σ noise level. For pixels with emission weaker than the 3 σ noise level, we assumed optically thin emission and used the integrated intensity of ^{13}CO :

$$N(^{13}CO)_i = \frac{3.76 \times 10^{14}}{f_u} \int T_R^*(^{13}CO) \, dv \quad [\mathrm{cm}^{-2}], \tag{3.4}$$

where f_u is the fraction of ^{13}CO in the upper state ($J = 1$). We take $f_1 = .55$ assuming $T_{ex} = 5$ K. Most of column density, and thus mass, are produced in regions with strong ^{13}CO emission. A contour map of N(^{13}CO) is shown in Figure 3.2(a) for the 0°.5 × 0°.5 region that was sampled every 1′. The map has been smoothed to the resolution of the star counts of 2′.2. Column densities shown range from 1 to 8×10^{15} cm^{-2} . The peak ^{13}CO column density of 8×10^{15} cm^{-2} is a lower limit, as it is smoothed over larger area than the telescope beam; the peak ^{13}CO column density before smoothing was 12.4×10^{15} cm^{-2} .

3.5 Visual Extinction

Determining extinctions in distant clouds using star counts is made difficult by the presence of foreground stars. A completely opaque region, which in a nearby cloud will show a total absence of stars, becomes increasingly difficult to distinguish at progressively larger distances, since the presence of interposed foreground stars reduces the contrast between the cloud and the unobscured, adjacent sky. Accordingly, once star counts have been carried out on a distant object, the raw counts in each reseau element must be reduced by the mean number of foreground stars expected within the solid angle subtended by each grid element at the distance of the cloud. Note that this procedure invariably reduce the dynamic range of the counts and, owing to the reduction in star numbers, unavoidably increases the statistical $(\sqrt{n})$ errors associated with the counts.

We have generally followed Herbst and Sawyer (1981)'s method for estimating foreground stars. They calculated foreground star numbers for samples of distant opaque clouds within $b = \pm 10°$ as well as those of nearby clouds, using the following method. The fundamental equation of general star-count analysis for an opaque cloud at distance r may be written as:

$$N_{ct} = \omega \int_{-\infty}^{m_{lim}} \int_{0}^{r} D(r') \times \Phi[m - 5logr' + 5 - E(r')]r'^2 dr' dm, \qquad (3.5)$$

where N_{ct} is the number of stars counted, ω is the solid angle and m_{lim} is the limiting magnitude of the counts. $D(r)$ represents the volume density of stars at distance r in units of the corresponding stellar density near the sun, $\Phi(M)$ is the luminosity function, and $E(r)$ is the extinction out to r along the line of sight.

The limiting magnitude for the star counts is estimated to be 20.5 mag, based on an extrapolation of the van Rhijn (1929) tables. By using observed values of N_{ct}, such as those of van Rhijn (1929), Equation 3.5 can be solved analytically for $D(r)$ by differentiating both sides with respect to r. However, an average density of stars can be determined from star counts to a known limiting magnitude in the direction of an opaque cloud. For NGC 2175 at a distance and direction ($d = 2.1$ kpc; $l = 190°, b = 0°$) similar to G216-2.5, Herbst and Sawyer (1981) calculated averaged density of stars $\overline{D(r)} = .25$, wherein the interstellar extinction is assumed to be evenly distributed along the line of sight.

Using Equation 3.5 with the adopted general color excess of $E_{B-V} = 0.1$ magnitude from Figure 3.1, an average density of 0.25, a cloud distance of 2.2 kpc, and the luminosity function of Wielen *et al.* (1983), we estimate the number of foreground stars in $2.'2 \times 2.'2$ reseau as 6.8. We are able to compare our value to that of NGC 2175 ($d = 2.1$ kpc, $l = 190°, b = 0°$), 5.7, and that of IC 1085 ($d = 2.4$ kpc, $l = 136°, b = +2°$), 7.1 (Herbst and Sawyer 1981). In consideration of their limiting magnitude of 21.1, our value of 6.8 seems to be a proper one.

The visual extinction distribution is shown as a gray scale (and contour) map in Figure 3.2(b). An inspection of Figures 3.2(a) and 3.2(b) shows a good correlation between ^{13}CO emission and visual extinction. Condensations with $A_V \geq 3$ magnitudes are visible, and a hole appears around the central portion of the cloud ($l = 216.°7, b = -2.°65$) in both maps. Some differences appear in the lower right and central parts of the map, possibly caused by noise in the data. Comparing visual extinction map with the integrated intensity map of ^{13}CO emission (Figure

3.2(c)) and ^{12}CO peak temperature map (Figure 3.2(d)), the apparent thickness and shape of the cloud are found to be in generally good agreement in all 3 maps. Note that the maps of visual extinction and ^{13}CO column density have 2.′2 resolution, and the maps of ^{12}CO peak temperature and ^{13}CO integrated intensity have 1′ resolution.

3.6 ^{13}CO and A_V

Figure 3.3 shows the observed correlation of N(^{13}CO) versus A_V. A regression line to describe the relationship between these quantities can be obtained in many ways (Isobe 1990), including the usual least squares fit, which minimizes the quantity $\sum[N(^{13}CO)_i - aA_{V_i} - b]^2$, where N(^{13}CO)$_i$ and A_{V_i} are individual values of column density and visual extinction, and a and b are the slope and the intercept of the fitted line. This method, however, fixes the x axis, A_V, and sometimes gives an unrealistic fit. The results of this fit to the data is shown by the dotted line in Figure 3.3. The points have a large dispersion, but this is expected, since we have applied star counts to an object a factor of four or five more distant than clouds in the solar neighborhood.

One can exchange the axes N(^{13}CO)$_i$ and A_{V_i} with each other, and minimize the quantity $\sum[A_{V_i} - aN(^{13}CO)_i - b]^2$. In this case, the ^{13}CO column density is fixed. The regression line of A_V on N(^{13}CO) is shown as the dashed line in Figure 3.3 and is given by $N(^{13}CO) = 3.0 \times 10^{15}(A_V - 1.5)$.

If the two parameters in a regression fit have a good correlation, the slopes obtained by the above two ways are, ideally, inversely proportional to each other. However, in most cases, the two slopes are not inversely matched precisely, because the two fit parameters will typically have different error ranges. Recently, Isobe *et al.* (1990) showed that these two slopes are the two extreme cases in a more general fit; one has the steepest slope and the other the smallest. Isobe *et al.* also introduced three other fits and calculated the dispersions of those slopes. They suggest that the bisector of the two extreme slopes performs significantly better than the other methods. In adopting Isobe *et al.* 's technique, we have therefore used traditional least squares fits to obtain the bisector regression line, which is given by

$$N(^{13}CO) = (1.73 \pm .09) \times 10^{15}(A_V - 0.95), \tag{3.6}$$

The bisector fit is shown as the solid line in Figure 3.3.

In Table 3.1 the slopes and intercepts of various published regression lines of column densities relative to visual extinctions for nearby clouds are listed. Slopes range from 1.3×10^{15} to 3.8×10^{15} cm^{-2} mag^{-1} and Dickman and Clemens (1983) derived 1.9×10^{15} cm^{-2} mag^{-1} for a large sample of local dark clouds. Since the slopes given in Table 1 were obtained by least squares fits, they should be regarded as lower limits, according to Isobe *et al.* (1990). In any case our results indicate that the ^{13}CO column density to visual extinction ratio in G216-2.5 is similar to (or slightly less than) that found in local molecular clouds. This suggests that if the gas to dust ratio is normal, the CO abundance in this object is similar to

that of clouds near the sun. A ^{13}CO abundance relative to molecular hydrogen of 1.7×10^{-6} is implied by the slope of the above fit.

Table 3.1 The results of least-square fits of N(^{13}CO) and A_V for nearby clouds of G216-2.5. The slope is in units of 10^{15} cm^{-3}, and the distance is in parsecs.

Name	*Slope*	*Intercept*	*Distance*	*Reference*
ρ Oph	2.5		160	Encrenaz *et al.* (1975)
L1344	3.8	...	150	Tucker *et al.* (1976)
L43	1.5	...	160	Elmegreen and Elmegreen (1979)
Taurus	1.4	1.0	100	Frerking *et al.* (1982)
ρ Oph	2.7	1.6	160	Frerking *et al.* (1982)
-	2.2	1.4	160	Dickman and Herbst (1990)
HCL2	1.3	0.5	100	Cernicharo and Guélin (1987)
L1495	2.0	0.5	100	Duvert *et al.* (1985)
Perseus	2.5	0.8	100	Bachiller and Cernicharo (1986)
Local clouds	1.9	...	...	Dickman and Clemens (1983)
G216-2.5	1.7	0.95	2200	This Work

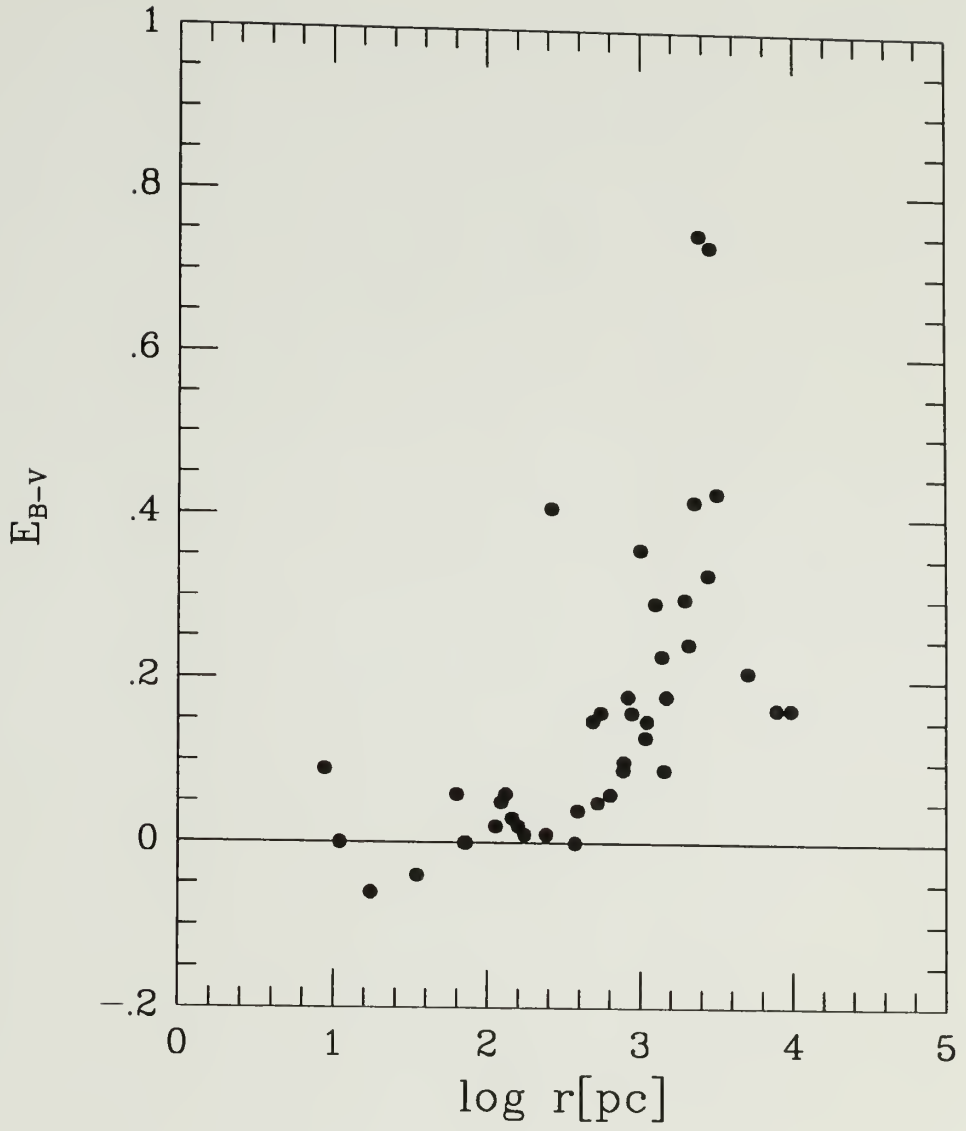

Figure 3.1 Color excess versus distance for 42 stars in the vicinity of G216-2.5.

Figure 3.2 (a) The ^{13}CO column density map of the 0.25 square degree region with 2′.2 resolution; contour levels are 1, 2, 3, ..., $8 \times 10^{15} cm^{-2}$. (b) Visual extinction map with 2′.2 resolution; contour levels are 1, 2, 3, 4, and 5 magnitude. (c) ^{13}CO integrated intensity map with 1′ resolution; contour levels are 3, 4, 5, ... 9, 10 K km s^{-1}. (d) ^{12}CO peak temperature map with 1′ resolution; contour levels are 2, 2.5, ..., 4.5, 5 K.

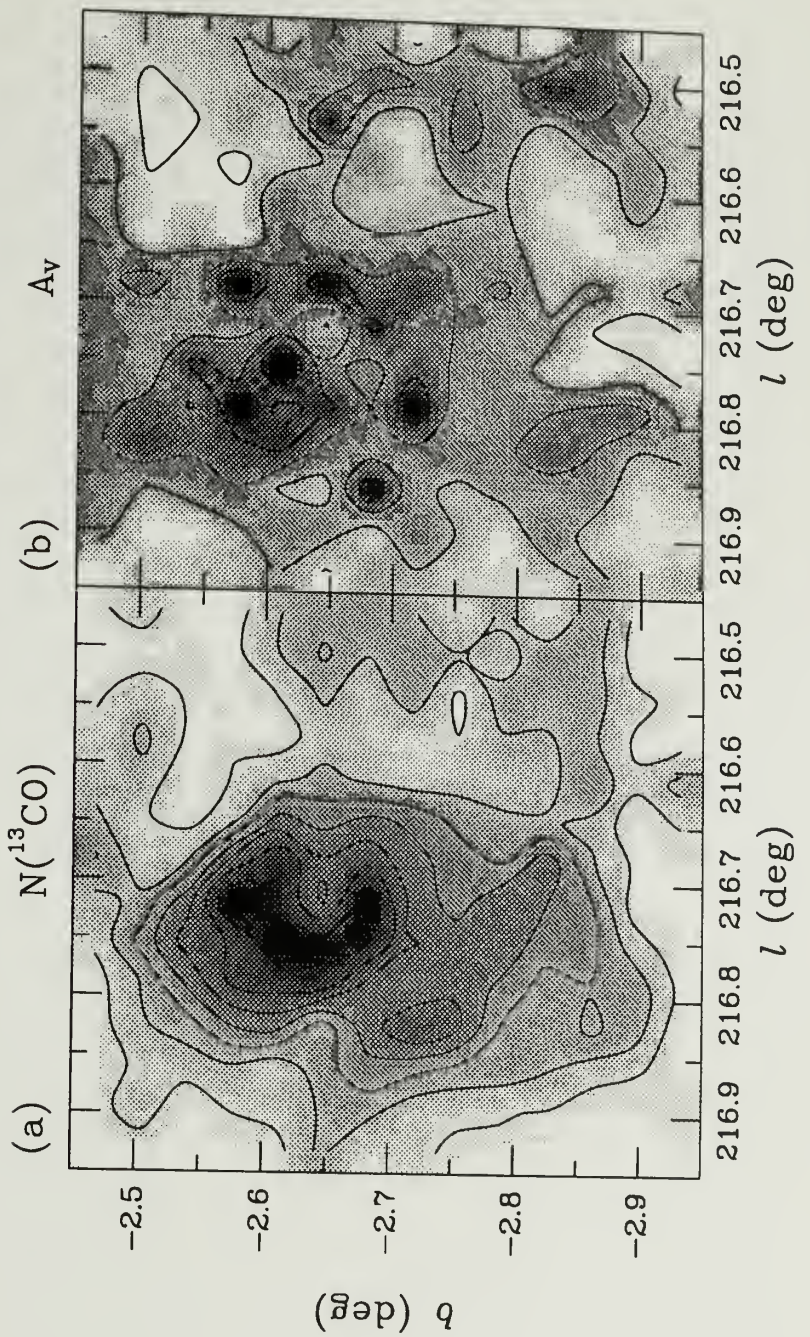
(a)
N(13CO)
(b)
AV
b (deg)
−2.5
−2.6
−2.7
−2.8
−2.9
216.9
216.8
216.7
216.6
216.5
216.9
216.8
216.7
216.6
216.5
l (deg)
l (deg)

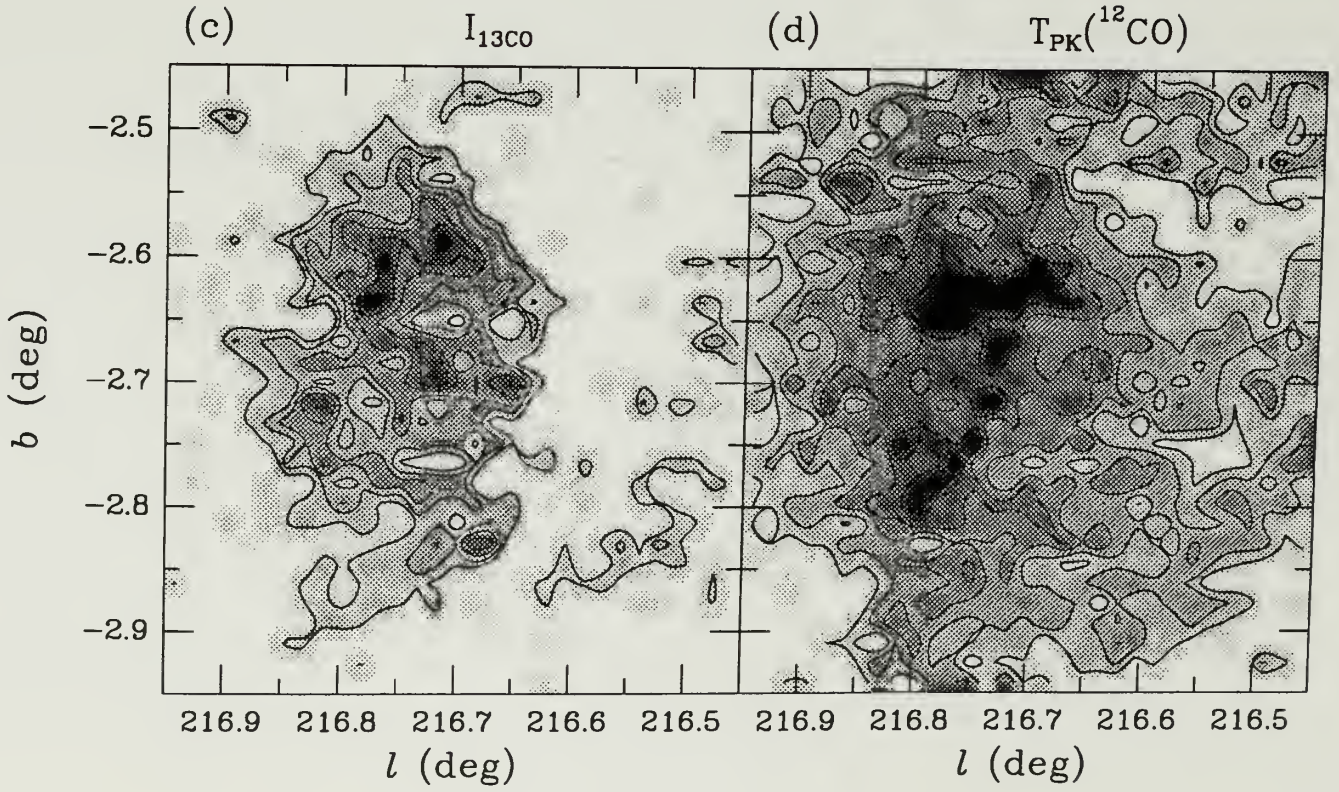
(c)
I_{13CO}
(d)
$T_{PK}(^{12}CO)$
−2.5
−2.6
−2.7
−2.8
−2.9
b (deg)
216.9
216.8
216.7
216.6
216.5
l (deg)
216.9
216.8
216.7
216.6
216.5
l (deg)

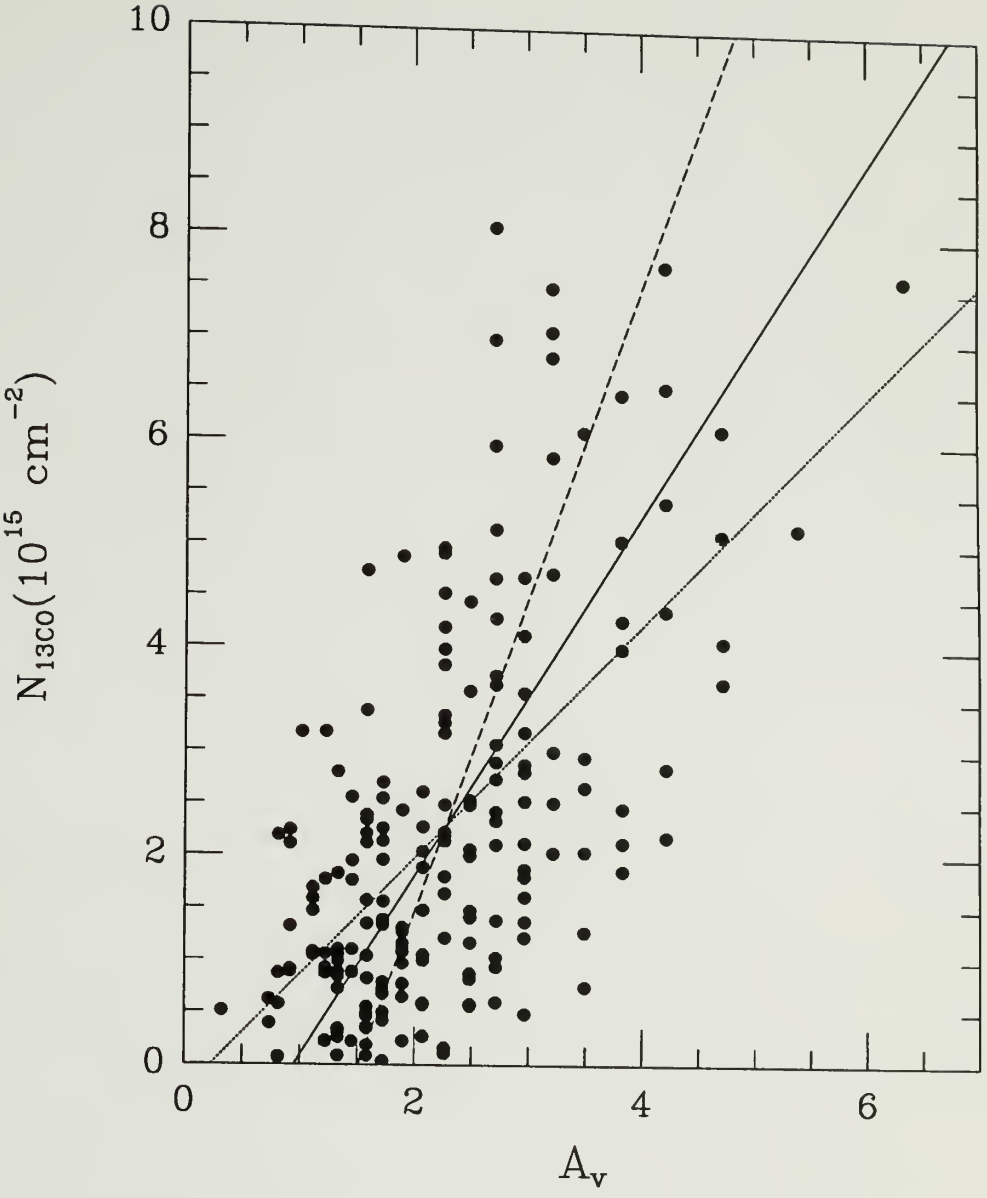

Figure 3.3 Extinction versus ^{13}CO column density correlation. Dotted line represents a traditional least-squares fitted line (LSQ), dashed line is LSQ case when the axes of x and y are changed. Solid line represents the bisector of these two lines; its slope is 1.73×10^{15}.

CHAPTER 4

ANALYSIS OF MOLECULAR LINE DATA

4.1 Introduction

In this Chapter the fundamental physical properties of G216-2.5 will be derived based on molecular line data. The characteristics of molecular clouds can be described according to their physical properties, such as cloud morphology, size, temperature, density, mass, and kinematics. As these properties are not all independent of one another, it is not always possible to derive them separately. The cloud temperature and density are the main descriptors, as they are very important in understanding the structure and evolution of molecular clouds. The temperature and density are dependent upon a wide variety of macroscopic and microscopic processes such as collisional process, radiative processes, heating and cooling. While the collisional and radiative processes are relatively local, the heating and cooling may depend on the global cloud structure. Thus, a reasonably accurate model for cloud temperature and density requires understanding the whole problem of molecular cloud structure.

Another important question to ask about molecular clouds is their velocity structure which governs the dynamics of the molecular gas and thus, the evolutionary process. While the temperature and density of these objects could be inferred

by molecular intensities, the velocity structure manifest itself in the details of the line profiles. Indeed, CO line profiles can provide quite specific and decipherable information on the structure and dynamics of the emitting region.

One of the most important issue for molecular clouds is the determination of cloud mass. It has been generally been assumed, and demonstrated that molecular clouds are gravitationally bound and in virial equilibrium. A mass estimate based on the virial expression has been appealing as it is simple to apply. However, there are other independent methods to estimate mass; the LTE technique, and a mass based on the ^{12}CO luminosity

In the following sections a detailed description will be presented on the morphology, velocity structure, and kinematics of G216-2.5. An explanation for cloud's cold temperature, unusual velocity field, and kinematics is attempted. The mass of the cloud will be estimated using three different methods.

4.2 Gas Temperature

4.2.1 CO Observation

One of the important parameters of molecular clouds is its kinetic temperature. Usually the kinematic temperature of the cloud is derived from the ^{12}CO observations assuming the ^{12}CO emission is optically thick and thermalized. Maddalena and Thaddeus (1985) originally observed G216-2.5 with Columbia 1.2 m telescope. Their FWHM beamwidth, 8′.7 provides relatively low angular resolution. Thus,

the peak temperature (< 2 K) of the cloud that they observed may severely underestimate the highest temperature regions.

Figure 4.1 shows a map of ^{12}CO peak antenna temperature of G216-2.5 with $2'$ resolution. The highest antenna temperature is found at the edge of the cloud ($l = 216°.8, b = -1°.06$), and has an antenna temperature of $T_R^* = 8.4$ K. This is in the direction of an embedded star cluster that will be discussed in Chapter 6. The peak antenna temperature in the main body of G216-2.5 is $T_R^* = 5.8$ K. However, most of the cloud has antenna temperatures less than 4 K. Thus, this cloud has substantially weaker CO emission than most GMCs. Figure 4.2 shows a ^{13}CO peak temperature map of G216-2.5. The ^{13}CO emission strength, on average, is roughly one-tenth of the ^{12}CO emission strength. The ^{13}CO peak antenna temperature is $T_R^* = 4.4$ K and is at the same position as the the ^{12}CO peak temperature. The highest ^{13}CO peak antenna temperature in the main body of the cloud is 2.6 K. A histogram of the ^{12}CO antenna temperatures is presented in Figure 4.3. The histogram shows the number of pixels versus ^{12}CO temperature in 0.14 K bins for the all of the individual 1,833,600 velocity channels. The hatched part of the histogram represents the true ^{12}CO emission after noise subtraction.

The radiation temperature is related to the corrected antenna temperature by the following relation: $T_R = T_R^* / \eta_c$, where η_c is the source coupling efficiency. For the large angular extent of G216-2.5, we have assumed η_c is approximately unity. The corrected antenna temperature is given by:

$$T_R = [\frac{h\nu/k}{e^{h\nu/kT_{ex}} - 1} - \frac{h\nu/k}{e^{h\nu/kT_{bg}} - 1}](1 - e^{-\tau}), \tag{4.1}$$

where T_{ex} is the excitation temperature, T_{bg} is the equivalent radiation temperature of cosmic background (2.78 K), and τ is the optical depth. For the ^{12}CO J = 1–0 transition ($h\nu/k = 5.53$) the emission is usually optically thick so that the excitation temperature is then given by:

$$T_{ex} = \frac{5.53}{\ln(1 + \frac{5.53}{T_R + 0.876})}. \tag{4.2}$$

The excitation temperature is related to the kinetic temperature only if the gas is thermalized and optically thick. For a ^{12}CO peak temperature of 5 K (T_R^*), the calculated kinetic temperature is 8.3 K. In the next subsection, the assumption of thermalization of CO will be tested by using a non-LTE model.

4.2.2 NLTE Model Predictions of the ^{12}CO Excitation Temperature

Non-LTE (NLTE) models of the molecular excitation have been computed to test the validity of the standard LTE assumptions for conditions appropriate to G216-2.5. To include radiative trapping in the excitation calculations, a large velocity gradient radiative transfer model (LVG) will be used. The first applications of the LVG model to molecular clouds were made by Goldreich and Kwan (1974), and Scoville and Solomon (1974). The computational simplicity of the model has been a major factor in its widespread use for determining the excitation of molecules in clouds, although it is now generally accepted that the velocity gradient required by the model is unlikely to be real. For the purposes of checking the LTE-derived results, however, the LVG model is acceptable in that it provides a method for solving the statistical equilibrium equations, which in turn determine the emitted

radiation temperatures of the two carbon monoxide species ^{12}CO and ^{13}CO. Further, the model explicitly accounts for radiative trapping effects – a feature which may be important for ^{12}CO and which LTE, by definition, cannot address.

The collision rate coefficients for CO-H_2 collisions come from Green and Thaddeus (1976). A dipole moment of 0.112 Debye for CO has been used. The free parameters for the NLTE model are kinetic temperature, density, CO column density, and line width. The velocity width was fixed at 5 km s^{-1}. Thus, the excitation and emission can be predicted as a function of density and CO column density for a fixed kinetic temperature. Densities ranging from 10 to 10^5 cm^{-3} were used and three ^{13}CO column densities were used (1×10^{16} cm^{-2}, 3×10^{15} cm^{-2}, and 1×10^{15} cm^{-2}) covering the range of column densities estimated by the LTE technique. The ^{12}CO column densities were assumed to be 100 times larger.

The model results are presented in Figure 4.4 and show that the ^{12}CO J = 1–0 transition is thermalized and optically thick for densities greater than 300 – 1000 cm^{-3} depending on the column density. However, when the ^{13}CO emission is stronger than 0.5 K, it is very likely that the ^{12}CO is a good measure of the kinetic temperature. Thus in directions where strong ^{13}CO emission is observed ($T_R^* > 0.5$ K), Equation 4.2 can be used to solve for the kinetic temperature from the ^{12}CO observations.

4.3 Mass of G216-2.5

The determination of masses and mass distribution of molecular clouds is a fundamental, yet poorly-understood problem (e.g., Dickman 1988). A widely used method to estimate cloud masses is through a virial equilibrium analysis that assumes the clouds are gravitationally bound and dynamically relaxed. The method is appealing largely due to its simplicity in application. Although there have been arguments made that the virial analysis using ^{12}CO linewidths overestimates GMC masses (MacLaren, Richardson, and Wolfendale 1988), most mass estimates of molecular clouds are derived using the virial assumption. Kutner (1984) and Myers (1987) have suggested that dark clouds are close to virial equilibrium, but that physical conditions in GMCs are quite different from those in the dark clouds and that GMCs are more likely to receive severe disturbances on time scales much shorter than their dynamical relaxation times. However, Scoville *et al.* (1987) have shown that there seems to be no difference between the relation between CO luminosity and virial mass for clouds with and without H II regions, although this does not prove that the virial assumptions are correct. Carpenter *et al.* (1990) argued that the virial mass estimate is in good agreement with the LTE mass estimate for star forming clouds with moderate masses ($10^3 \sim 10^4$ $M_\odot$), and Lee *et al.* (1990) found discrepancies between these two mass estimates for the molecular clouds toward the Galactic molecular ring.

Three different techniques for estimating the mass of G216-2.5 are discussed below.

4.3.1 *LTE Mass Estimate*

A technique that has been widely used to estimate cloud masses is the LTE method. A brief discussion of this technique and the assumptions inherent in its use were presented in Chapter 3. When both ^{12}CO and ^{13}CO lines have been observed toward each line of sight, the ^{13}CO column density can be determined. In Chapter 3, we derived a correlation between the visual extinction and ^{13}CO column density for the core region of G216-2.5. This technique has been used often in estimating ^{13}CO abundances especially in dark clouds in the solar neighborhood.

To check the validity of the LTE technique, we have used a NLTE model, as described in previous section, to predict the emission from clouds with a wide range of densities and CO column densities. The radiation temperatures predicted by this model were then analyzed using the LTE technique to determine how successful the LTE method was at recovering the original model column density. Figure 4.5 shows the excitation temperature of ^{12}CO and ^{13}CO predicted by NLTE model as a function of density and column density. We note that the LTE assumption of equal excitation temperatures of ^{12}CO and ^{13}CO is not valid at densities below $\sim$ 3000 cm^{-3}. Since at densities below $\sim$ 3000 cm^{-3}, the excitation temperatures are not equal, then the LTE underestimates the optical depth of ^{13}CO and consequently the ^{13}CO column density. This effect is illustrated in Figure 4.6 which shows the ratio of LTE derived ^{13}CO column density to the original model column density as a function of density. For densities less than 3000 cm^{-3}, the column density can be severely underestimated using the LTE technique. This will also affect the estimate of the ^{13}CO abundance.

So far, only the slope of the visual extinction to ^{13}CO column density was used in estimating the CO abundance. Most studies of $N(^{13}CO)$ and visual extinction showed that there exists a non-zero intercept (see Table 3.1). Molecular clouds may have outer regions in which either the CO is photodissociated by the interstellar radiation field or the density is insufficient to excite ^{13}CO emission. In either case, the dust in this region will contribute to the visual extinction; however, the region will not contribute any ^{13}CO emission and would explain the non-zero intercept of the above relation. Thus, in estimating the total gas column density of the cloud the intercept should be included. The following equations present a connection between visual extinction and hydrogen column density (Bohlin, Savage, and Drake 1978) using the relation between ^{13}CO column density and visual extinction which we obtained in Chapter 3:

$$N(HI) + 2N(H_2) \simeq 2 \times 10^{21} A_V \tag{4.3}$$

$$N(^{13}CO) = 1.73 \times 10^{15}(A_V - 0.95) \tag{4.4}$$

$$N(HI)/2 + N(H_2) = 10^{21} \left[\frac{N(^{13}CO)}{1.73 \times 10^{15}} + 0.95 \right] \tag{4.5}$$

$$N(HI)/2 + N(H_2) = \frac{N(^{13}CO)}{X(^{13}CO)} + 0.95 \times 10^{21}. \tag{4.6}$$

From Equation 4.6 we can determine the H_2 column density and total mass (the LTE masses are multiplied by a factor of 1.36 to account for the contribution of He by mass). An LTE mass of 1.1×10^5 $M_\odot$ is estimated for G216-2.5. Most of the column density, and thus the mass, are produced in regions with strong ^{13}CO emission.

4.3.2 *Virial Mass Estimate*

Virial Analysis

If a molecular cloud is gravitationally bound, and has had enough time to be dynamically relaxed, then the partition of energy will be governed by the virial theorem. In its simplest form it says that the cloud kinetic energy, T, is related to the gravitational potential energy, U (ignoring external pressure) by:

$$2T + U = 0 \tag{4.7}$$

From this equation, the virial mass is given by

$$M_{VIR} = \frac{3\beta\sigma_{tot}^2}{2G}\, D, \tag{4.8}$$

where D is cloud diameter, and σ_{tot} is total velocity dispersion of the cloud, which represents all forms of kinetic motion within the cloud. The constant β is usually dependent on the density model of the cloud.

It is convenient to decompose the gas motions within molecular clouds into two terms. These are discussed by Dickman and Kleiner (1985) and represent two measurable motions within clouds: The first is an 'internal velocity dispersion' which represents the spread of velocities observed along each line of sight, and second is a 'centroid velocity dispersion' which is usually associated with point-to-point bulk motions of the gas within the cloud traced in a map.

The centroid velocity dispersion is simply the ensemble variance of the line of sight average velocities. The centroid velocity of each line of sight in the cloud is

given by:

$$v_c^i = \frac{\sum_j T_j v_j}{\sum_j T_j}, \tag{4.9}$$

where the summation is over the entire velocity range associated with the cloud in that line of sight. The average centroid velocity of a cloud is thus

$$< v_c >= \frac{\sum_i v_c^i}{N}, \tag{4.10}$$

where the summation is over all lines of sight through the cloud, N. Therefore the centroid velocity dispersion is given by

$$\sigma_c^2 = \frac{\sum_i (v_c^i - < v_c >)^2}{N}. \tag{4.11}$$

The internal velocity dispersion characterizes the magnitudes of gas motions along individual lines of sight with respect to the average velocities along those directions. The internal dispersion along the line of sight, σ_i^k, can be calculated from the following equation:

$$(\sigma_i^k)^2 = \frac{\sum_j T_j (v_j - v_c^k)^2}{\sum_j T_j}, \tag{4.12}$$

where the summation is over all velocities, and the cloud internal velocity dispersion, σ_i, is given by:

$$\sigma_i^2 = \frac{\sum_k (\sigma_i^k)^2}{N}. \tag{4.13}$$

Size Definition

Since clouds are irregularly shaped, it is not straightforward to define a cloud size. We adopt as a measure of mean cloud diameter the following:

$$D = \sqrt{(4A/\pi)} \quad [pc], \tag{4.14}$$

where A is the area in units of square parsecs.

Other definitions of size will be discussed in Chapter 7.

Results

If we assume a uniform density distribution and a spherical cloud ($\beta \sim 1.6$), the virial mass is given by:

$$M_{VIR} = \frac{5\ \sigma_{tot}^2}{2G}\ D, \tag{4.15}$$

where D is the diameter, and $\sigma_{tot} = \sqrt{\sigma_i^2 + \sigma_c^2}$, the one dimensional velocity dispersion. If D is measured in pc and σ_{tot} in km s^{-1}, we get:

$$M_{VIR} = 582\ D\ \sigma_{tot}^2 \quad [M_\odot]. \tag{4.16}$$

The internal and centroid dispersions for G216-2.5 are estimated to be $\sigma_i = 1.82$ km s^{-1}, $\sigma_c = 2.75$ km s^{-1}. Thus, the total velocity dispersion, σ_{tot}, is 3.29 km s^{-1}, which corresponds to $\Delta V = 7.75$ km s^{-1}. The area of the cloud is defined to be that covered by all pixels with ^{12}CO emission greater than 5σ of ^{12}CO integrated intensity. Using Equation 4.14, the size of G216-2.5 is 100.8 pc assuming a distance of 2.2 kpc. From Equation 4.16, a virial mass of $6.36 \times 10^5\ M_\odot$ is obtained for G216-2.5.

4.3.3 *Mass from the CO Luminosity*

Another mass estimate can be obtained by using the relationship between the CO integrated intensity and molecular hydrogen column density or equivalently the relationship between CO luminosity and mass. The constant of proportionality then represents the conversion factor of CO luminosity or integrated intensity to mass or column density and implicitly assumes that such a factor has a general applicability. The relationship has been studied by a number of investigators and reviewed in Scoville and Sanders (1987). Usually the virial mass is used to calculate the conversion factor. In fact, if clouds are virialized, a relation between total CO luminosity and cloud mass can be theoretically demonstrated to exist (Dickman, Snell, and Schloerb 1986). Empirical estimates of the conversion constant based on molecular observations vary between 1 and 5×10^{20} cm^{-2} (K km s^{-1})$^{-1}$(Scoville and Sanders 1987); the lack of agreement for this quantity is the dominant source of uncertainty in deriving molecular gas masses by this knowledge.

The conversion factor has also been established through γ-ray analysis. Several γ-ray studies (Lebrun *et al.* 1983; Bloemen *et al.* 1984; and summary by Bloemen 1989) found similar conversion constants; ranging from 2 to 3 $\times$ 10^{20} cm^{-2} (K km s^{-1})$^{-1}$. Also the γ-ray analysis indicates that the conversion factor is roughly constant as a function of Galactic radius (except possibly for the center of Galaxy) (Bloemen 1987). One merit of this method for determining the conversion function is that it is independent of virial mass estimates; the γ-ray flux directly probes the H_2 column density.

The ^{12}CO luminosity of G216-2.5 is $6.1 \times 10^4\ L_\odot$. Thus, if we use the most recent estimate of the conversion factor, 2.3×10^{20} cm^{-2} (K km s^{-1})$^{-1}$(Bloemen 1989), we obtain a mass: $M_{CO} = 3 \times 10^5\ M_\odot$.

4.4 Cloud Density

Mass estimates were presented in the previous section, and with a plausible assumption about geometry, the average spatial density can be estimated. The cloud volume has been estimated assuming it is a cylinder 100 pc in length and 50 pc in diameter. Assuming a mass between 10^5 and $6 \times 10^5\ M_\odot$, the average number density of the cloud is between 10 and 60 cm^{-3}. This is much lower than most GMCs which have densities of a few 100 cm^{-3} (Solomon *et al.* 1987). However, while the average density based on global cloud properties is useful, it may be far from giving a reasonable accurate picture of inhomogeneous molecular clouds (Snell *et al.* 1984).

Another method to estimate the density is based on the measurement of the column density and an estimate of the line of distance. Estimate of the column densities were described in Chapter 3. The highest ^{13}CO column density is approximately 10^{16} cm^{-2}; thus, the total H_2 column density is roughly 6×10^{21} cm^{-2}. The high column density region has an angular size of $\sim 0°.1$ (see Chapter 3); if it is spherical then the line of sight distance is approximately 3.8 pc. The average density in this region is roughly 500 cm^{-3}. However, densities of 500 cm^{-3} are

insufficient to explain the strength of the observed ^{13}CO emission, thus the cloud would be very inhomogeneous.

CS J = 2–1 emission was also observed in regions with strong ^{13}CO emission. Of the six positions observed, conspicuous CS emissions was detected in only three positions, including two star forming sites (these will be discussed in Chapter 6). One of these three positions, a $13' \times 15'$ region centered on $l = 216°.75$, $b = -2°.65$ was mapped in CS J = 2–1. The CS peak temperature contours are overlayed on a ^{13}CO integrated intensity grey scale map in Figure 4.7. At least two elongated clumpy structures are found. This fact reinforces the idea that the density in G216-2.5 is very inhomogeneous. The strongest CS emission ($T_R^* = 0.29$ K) arises at $l = 216°.47$, $b = -2°.39$. A composite plot of ^{12}CO, ^{13}CO and CS spectra is shown in Figure 4.8. With a kinetic temperature of 8 K, X(CS) = 10^{-8}, and ΔV = 3 km s^{-1}, the model can match the observed antenna temperature of 0.3 K, if the hydrogen molecule density is larger than 3×10^3 cm^{-3} (see Figure 4.9).

4.5 Morphology and Velocity Structure

G216-2.5 has an extent of 4.5 degrees in Galactic longitude, and 2.5 degrees in Galactic latitude, centered on $l = 216.°5$, $b = -2.°5$. Assuming a distance of 2.2 kpc (see Chapter 3), the full extent of the cloud is 170 × 100 pc. The size is larger than the average GMC. In Table 4.1, the physical parameters of typical GMC are given in comparison to G216.-2.5.

G216-2.5 is comprised of an elongated main cloud and a smaller cloud, the size of which is about one fifth the size of the main cloud. This smaller cloud, located just one-half degree away from the border of the main cloud, has similar properties as those of main cloud. Both clouds are very cold, as originally pointed by Maddalena and Thaddeus (1985), and have the same velocity of $V_{\rm LSR} = 27$ km s^{-1}. Thus, the smaller cloud is almost certainly associated with the main cloud.

The CO linewidths found in G216-2.5 (ΔV is ~ 8 km s^{-1}) are very broad and are matched only by linewidth found in the larger GMCs (Table 4.1). Maps of the cloud at individual velocities are shown in Figure 4.10. Two spectrometer channels were binned together for each map (the velocity resolution per channel is 0.65 km s^{-1}, thus the velocity coverage of each map is 1.3 km s^{-1}) and the velocity range covered by the maps is 18 to 34 km s^{-1}. These maps reveal a rather complicated velocity structure. The most striking features are an oval-shaped structure seen in Figure 4.10(a) and a ring-like structure seen in Figure 4.10(c) centered at $l = 216°.5, b = -2°.5$. The ring is almost 50 pc in diameter at $V_{\rm LSR} = 27$ km s^{-1}, and at higher velocities it is much larger and the emission is found preferentially on the left-hand side of the ring.

Figure 4.11 represents a series of position-velocity maps covering the entire l and b of the cloud. Each box in Figure 4.11 is a position-velocity map, spaced equally across the cloud in galactic longitude. The spacing between position-velocity maps is 20′. The velocity coverage for each map is 16 to 38 km s^{-1} , running from left to right. Figure 4.12 is another series of position-velocity maps with a spacing of 15′ in Galactic latitude. These position-velocity maps show substantial systematic

Table 4.1 Physical parameters of typical GMCs

Parameters	*Scoville and Sanders* (1987)	*Goldsmith* (1987)	G216-2.5
Diameter (pc)	40	20-80	100
Mass ($M_\odot$)	4×10^5	$8 \times 10^4 - 2 \times 10^6$	1.1×10^5
n(H_2) (cm^{-3})	180	$100 - 300$	$10 - 50$
T_K (K)	10	$7 - 15$	< 8
Linewidth (km s^{-1})	9	$6 - 15$	8

velocity structure within the cloud. One of more striking features is the structure at $l = 216.7$ and $b = -2.2$ in Figure 4.11 and Figure 4.12. In both position-velocity maps the emission splits into blue-shifted and red-shifted components as one would expect for an expanding shell. The angular size of this structure is about 0°.5 or a linear size of 20 pc. The expansion velocity is a few km s^{-1}, suggesting a dynamical age of about 3×10^6 years.

In addition to this expanding shell, the overall cloud velocity structure shows a systematic behavior. Both longitude and latitude position-velocity cuts through the center of the cloud show an arc-shaped structure; the largest blue-shifted velocity are found at the center of the cloud, while at the edges the gas is more red-shifted relative. This velocity structure is more obvious in the position-velocity map made diagonally across the cloud ($l = 217°.3$, $b = -3°.4$ to $l = 215°.4$, $b = -1°.8$) shown in Figure 4.13. The most plausible explanation for such a systematic velocity structure, is that the cloud forms part of a large expanding shell. The largest approaching velocity is found at the center of the cloud. Note that the difference between two extreme velocities is almost 10 km s^{-1}, suggesting that the expansion

velocity of the shell is at least 10 km s^{-1}. Figure 4.14 is a grey-scaled map that indicates the mean velocity of the cloud in each direction. This figure clearly shows the systematic velocity variations across the cloud.

Figure 4.15 is a position-velocity map of the small cloud located in the upper-righthand corner (the satellite cloud) of Figure 4.1 ($l = 214°.5, b = -1°.75$); this object continues the same trend of velocity structure seen in the main cloud (Figure 4.10).

Overall, the velocity structure of the cloud is dominated by large scale motions; it appears that the cloud may have been severely disrupted and material is being sheared or torqued. The broad linewidths that we see may be largely due to these systematic motions. Further discussion of the kinematics of the cloud will be presented in detail in Chapter 7.

4.6 S287 and the Associated Molecular Cloud

The H II region S287, and its associated molecular cloud, is located at $l = 218°.1$, $b = -0°.4$. This is the only H II region, which we believe is associated with G216-2.5. The V_{LSR} of the molecular cloud is the same as that of G216.2.5. The projected distance from the center of G216-2.5 is $\sim$ 100 pc. The ^{12}CO peak temperature is 12 K and the ^{13}CO peak temperature is 5 K. In Figure 4.16 a ^{12}CO integrated intensity map of S287 cloud along with G216-2.5 is shown. The morphology of the cloud is quite different from that of G216-2.5. The cloud is filamentary and has three dense cores, which are preferentially located at the ends of the long filament. Along with

the brightest star at the center of S287 (an O9.5 star which is marked by a filled triangle in Figure 4.17), a few young stars (B0 – A5) are also forming (Neckel *et al.* 1989) near these dense cores. The filamentary structure of the cloud is probably being shaped by the strong stellar winds from these young stars. The mass of the cloud has been estimated in two different ways. The virial mass estimate is $6 \times 10^4 M_\odot$ (S287 has a size of 26 pc, and a linewidth of 4.5 km s^{-1}) and the LTE mass estimate is 1.3×10^4 $M_\odot$. Comparison with G216-2.5 and the possibility of association of two clouds will be discussed in Chapter 7.

Figure 4.1 The ^{12}CO peak temperature map of G216-2.5. The range of the grey scale is 0.3 to 3 K. The lowest contour level and the increment between levels is 0.6 K.

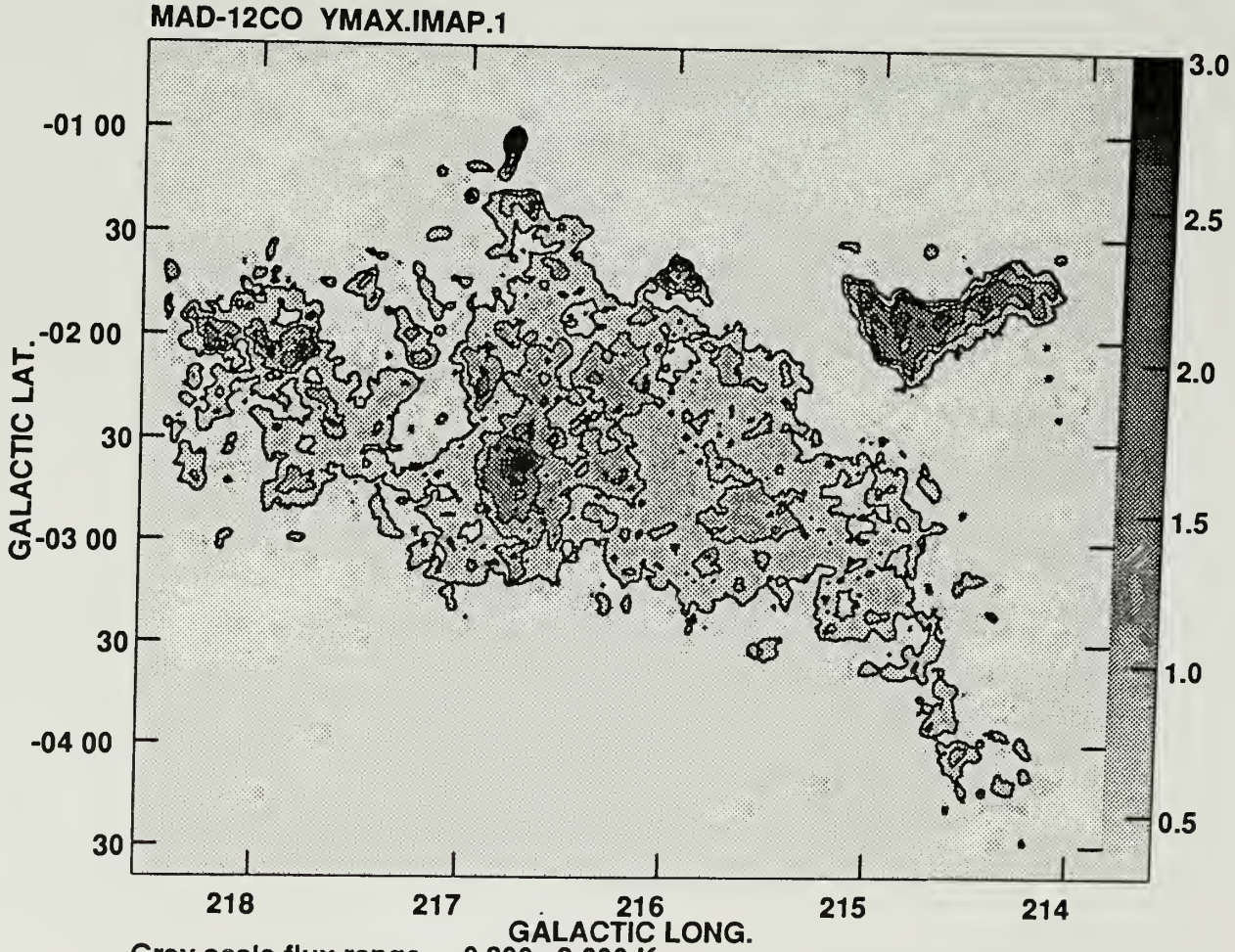
MAD-12CO YMAX.IMAP.1
-01 00
30
-02 00
30
-03 00
30
-04 00
30
GALACTIC LAT.
218
217
216
215
214
GALACTIC LONG.
3.0
2.5
2.0
1.5
1.0
0.5
Grey scale flux range= 0.300 3.000 K
Peak contour flux = 4.3511E+00 K
Levs = 6.0000E-01 * (1.000, 2.000, 3.000,
4.000, 5.000, 6.000, 7.000)

Figure 4.2 The ^{13}CO peak temperature map. The range of the grey scale is 0.08 to 1 K. The lowest contour level and the increment between levels is 0.15 K.

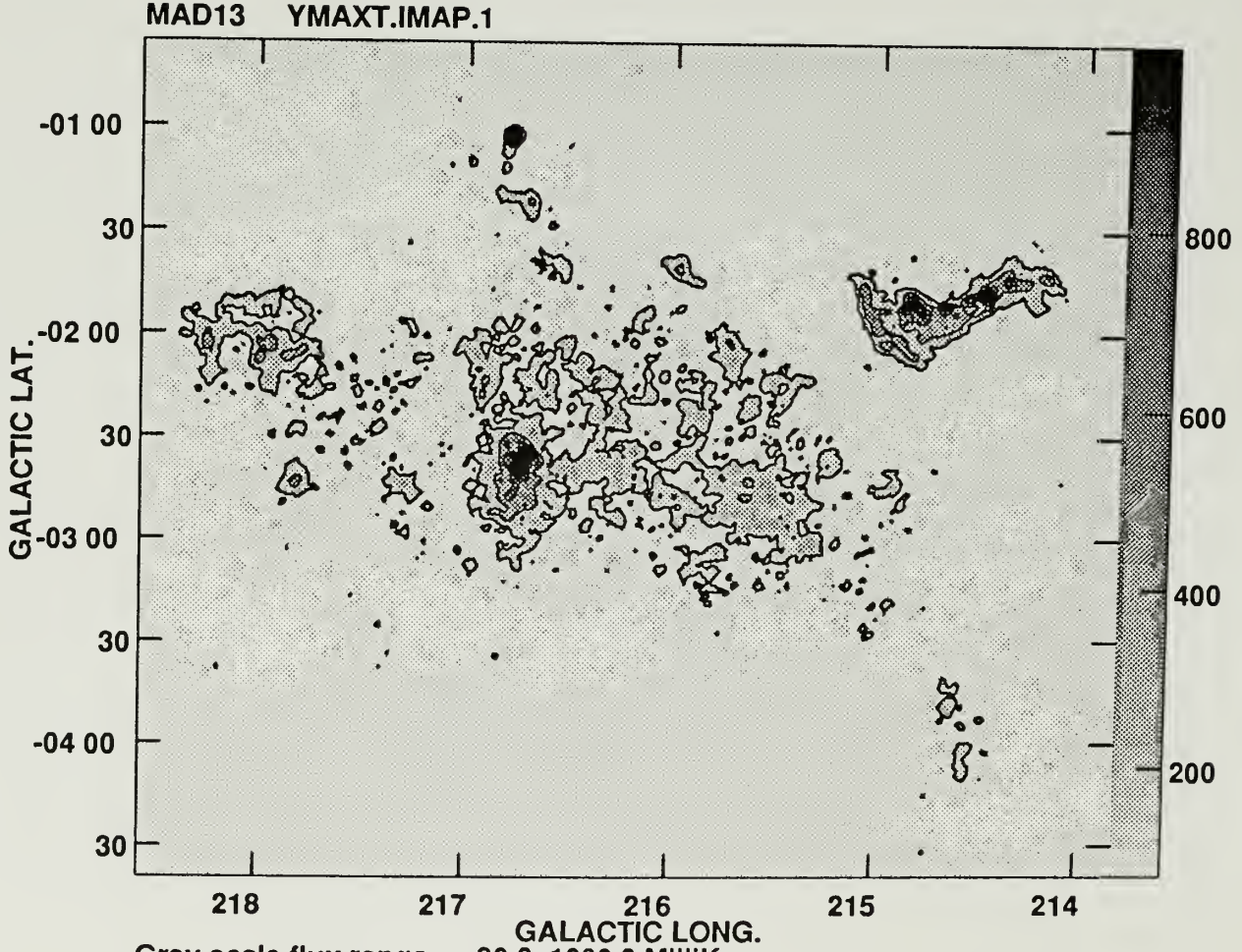
MAD13 YMAXT.IMAP.1
-01 00
30
-02 00
30
-03 00
30
-04 00
30
GALACTIC LAT.
218
217
216
215
214
GALACTIC LONG.
800
600
400
200
Grey scale flux range= 80.0 1000.0 MIIIIK
Peak contour flux = 1.5698E+00 K
Levs = 1.5000E-01 * (1.000, 3.000, 5.000,
7.000, 9.000)

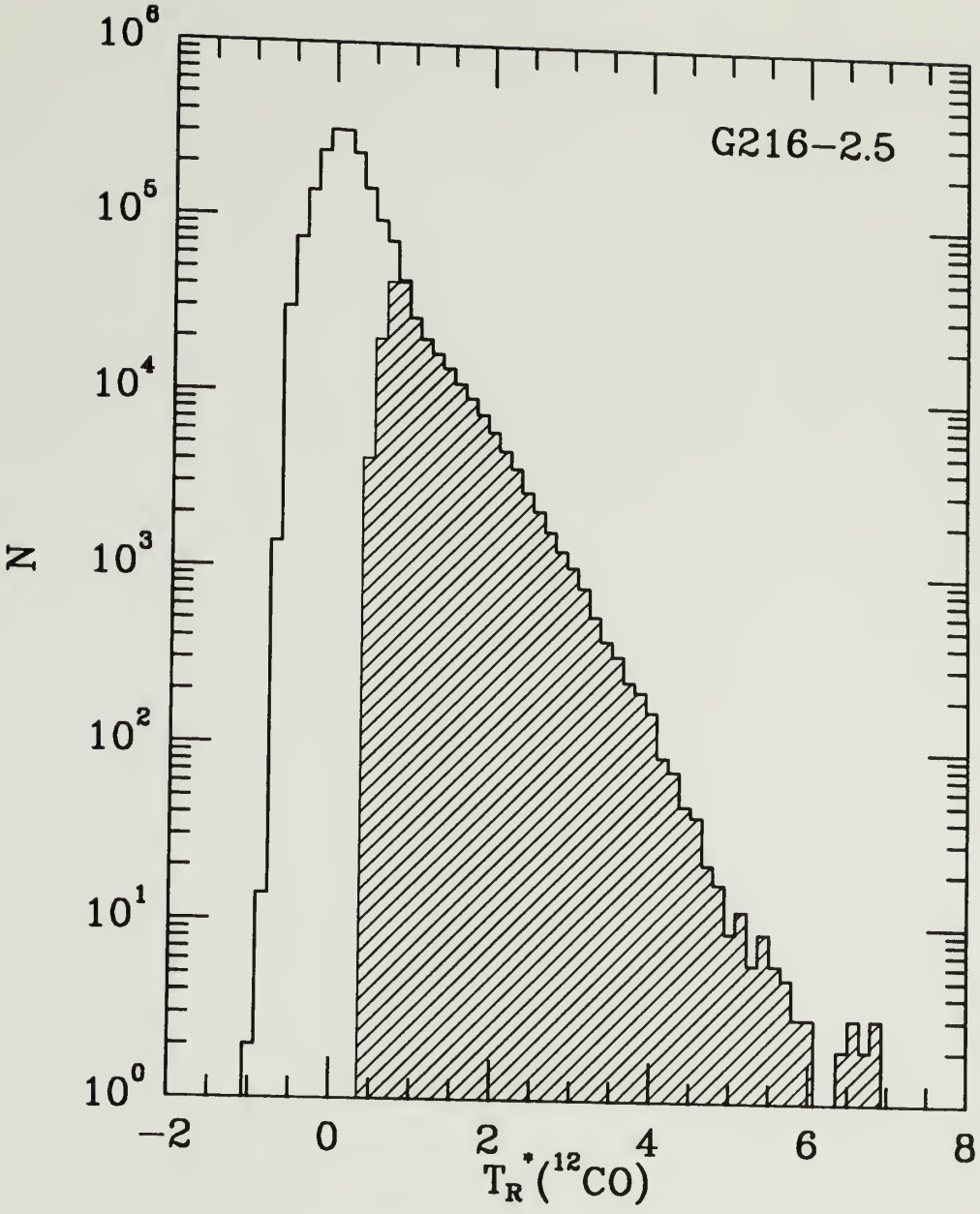

Figure 4.3 Histogram of ^{12}CO corrected antenna temperature for all the individual positions and velocity channels, totaling $\sim$ 1.8 million points. The temperatures are binned in 0.14 K intervals. The hatched part of the histogram represents the true ^{12}CO emission after the noise subtraction: Emission is detected in only 13% of the 1.8 million spatial and velocity points.

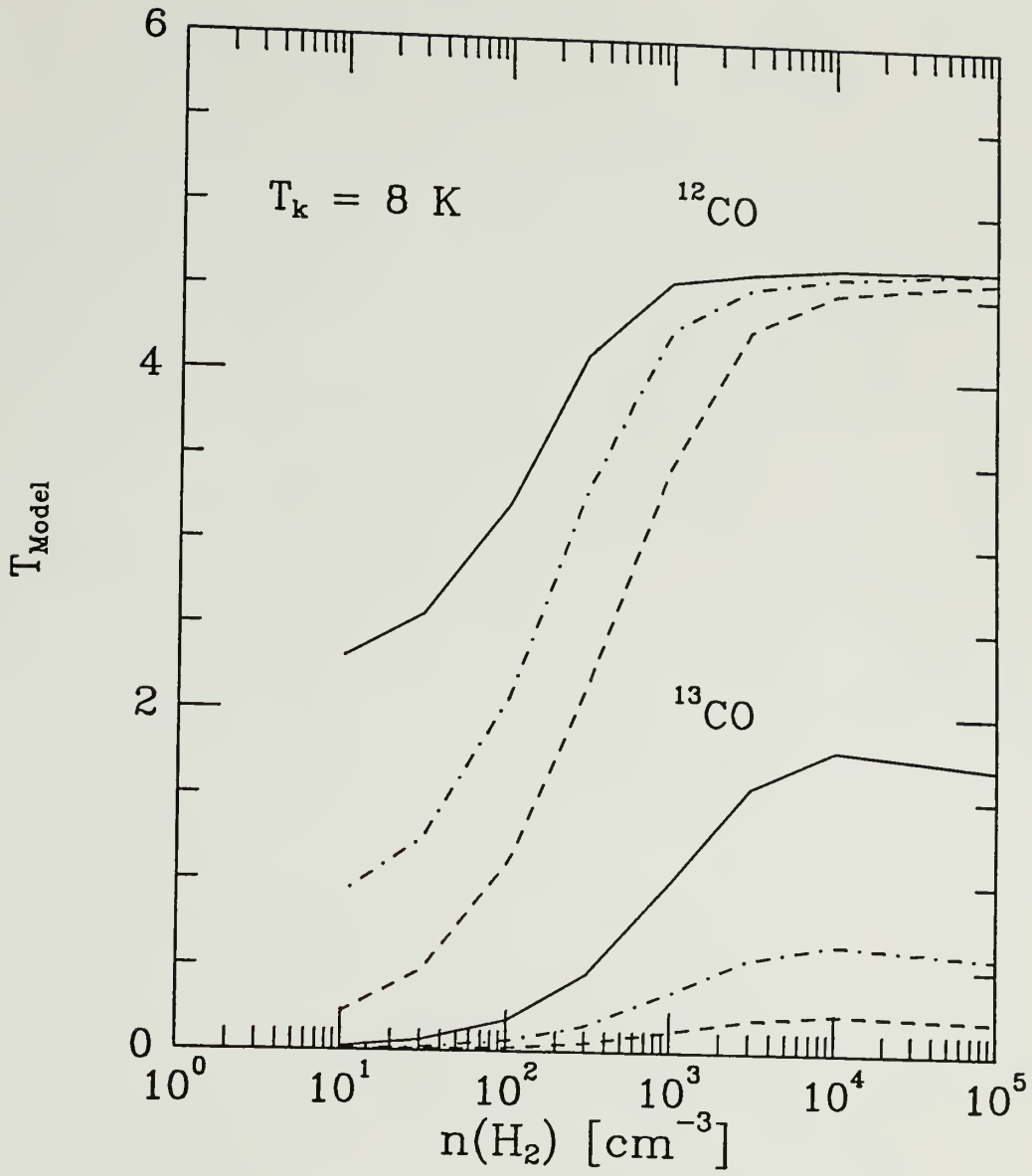

Figure 4.4 The corrected antenna temperature for ^{12}CO and ^{13}CO predicted from the NLTE model as a function of density for three different column densities. For ^{13}CO the column densities were 1×10^{16} (solid line), 3×10^{15} (dot-dashed line), and 1×10^{15} cm^{-3} (dashed line). The ^{12}CO column densities are 100 times larger.

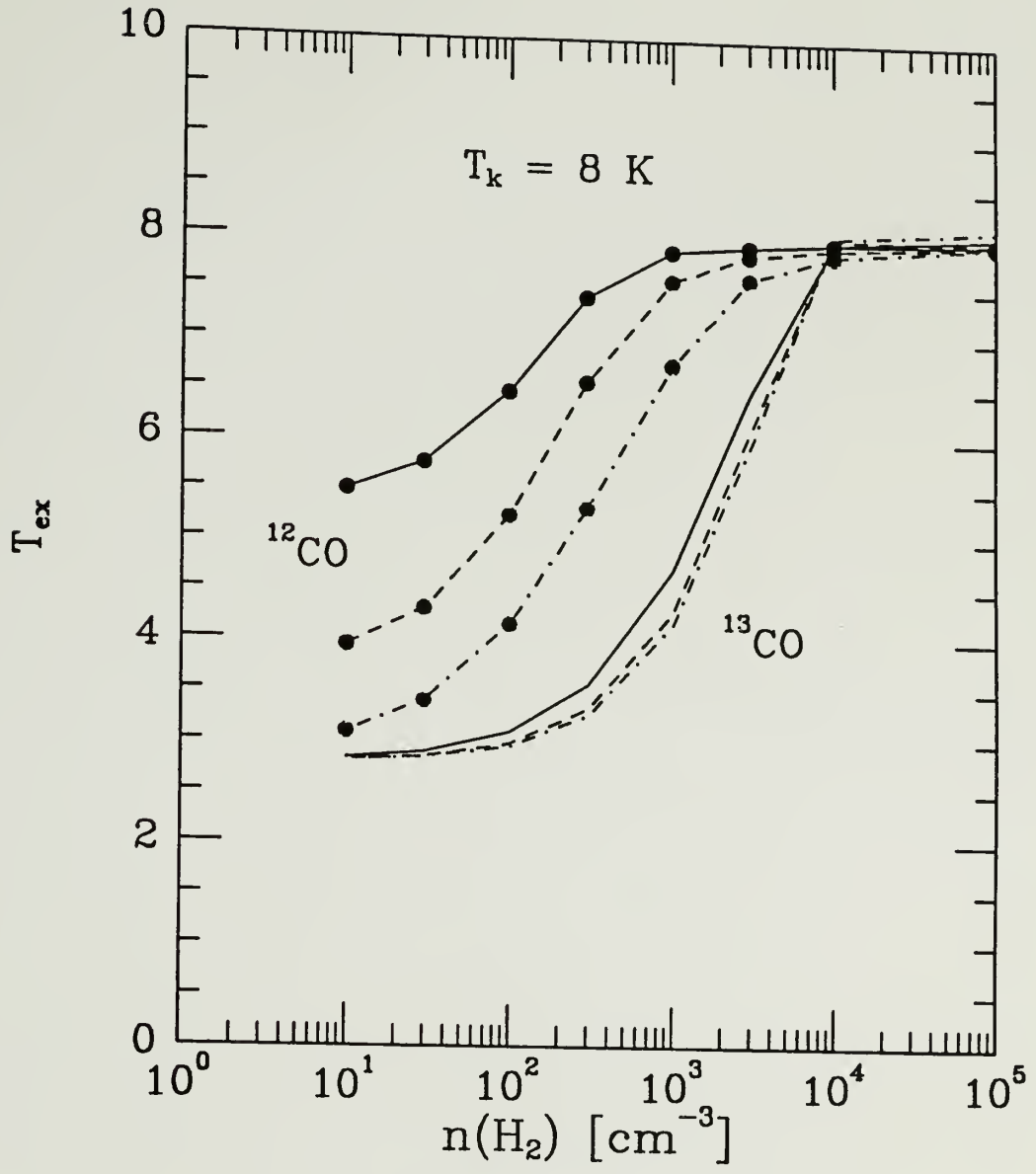

Figure 4.5 The NLTE model derived excitation temperatures for ^{12}CO and ^{13}CO as function of density for the same column densities as shown in Figure 4.4

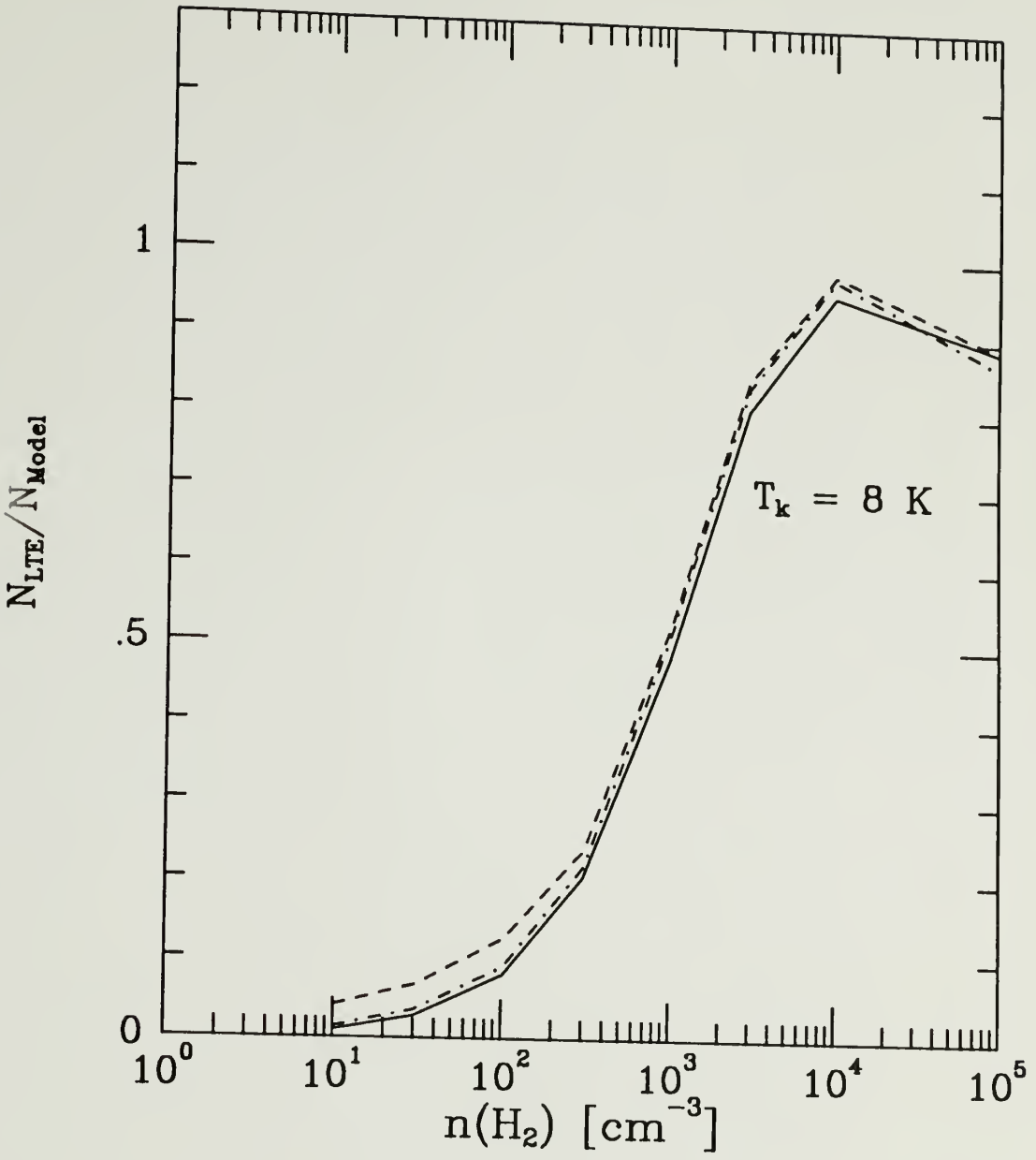

Figure 4.6 The ratio of the LTE ^{13}CO column density to model ^{13}CO column density as a function of density. The ratio was calculated for three model column densities: 1×10^{16} (solid line), 3×10^{15} (dot-solid line), and 1×10^{15} cm^{-3} (dashed line).

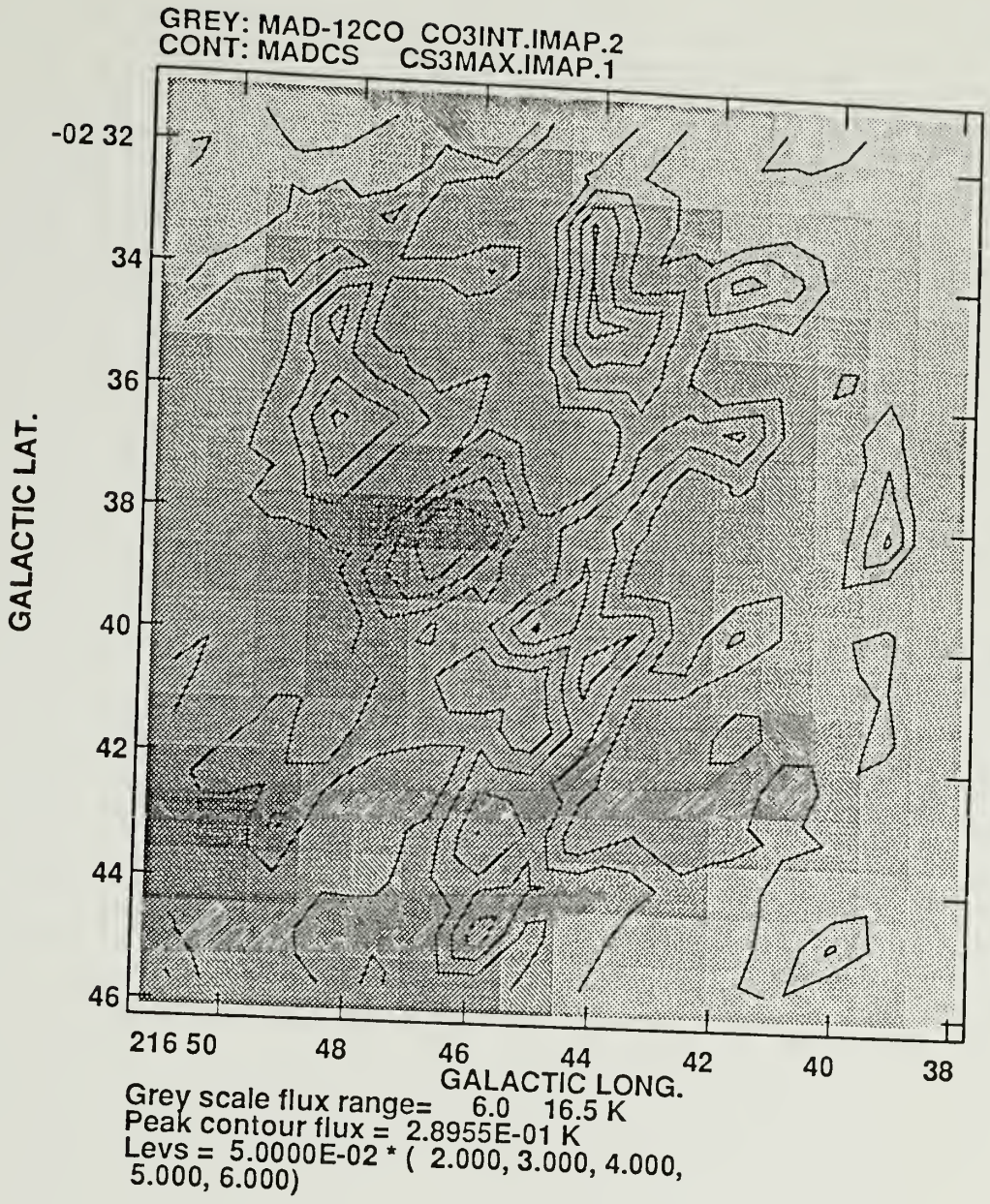

Figure 4.7 A contour map of CS peak antenna temperature overlayed on a grey-scaled image of the ^{13}CO integrated intensity. This is one of the strongest ^{13}CO emitting region in the cloud. The range of the grey scale image is 0.3 to 4 K km s^{-1}, and the lowest contour level is 0.1 K, and the interval between contours is 0.05 K.

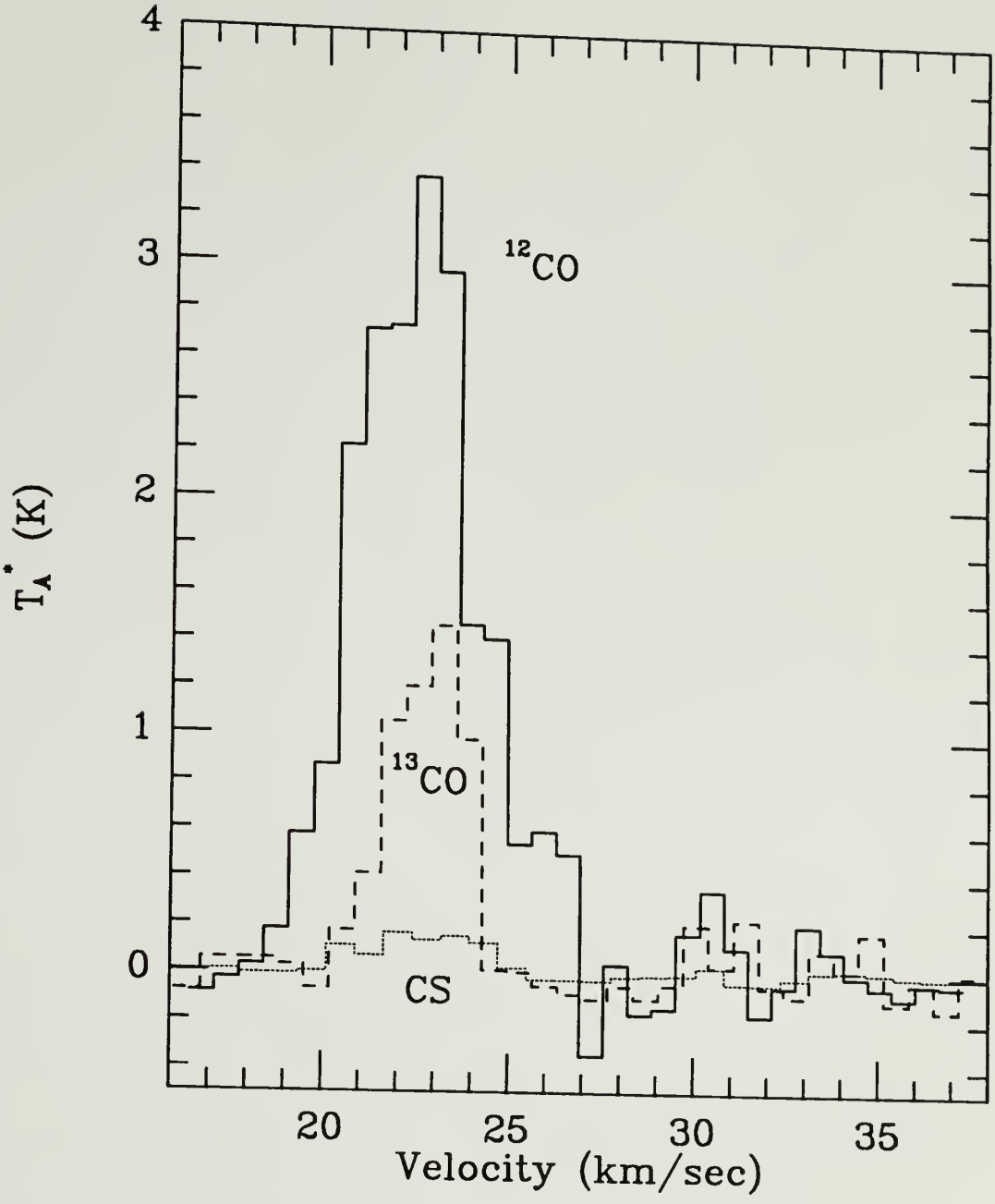

Figure 4.8 Spectra of ^{12}CO, ^{13}CO, and CS lines for one of strongest emission regions at $l = 216°.75$, $b = -2°.65$. The solid line is ^{12}CO, dashed line is ^{13}CO, and dotted line is CS.

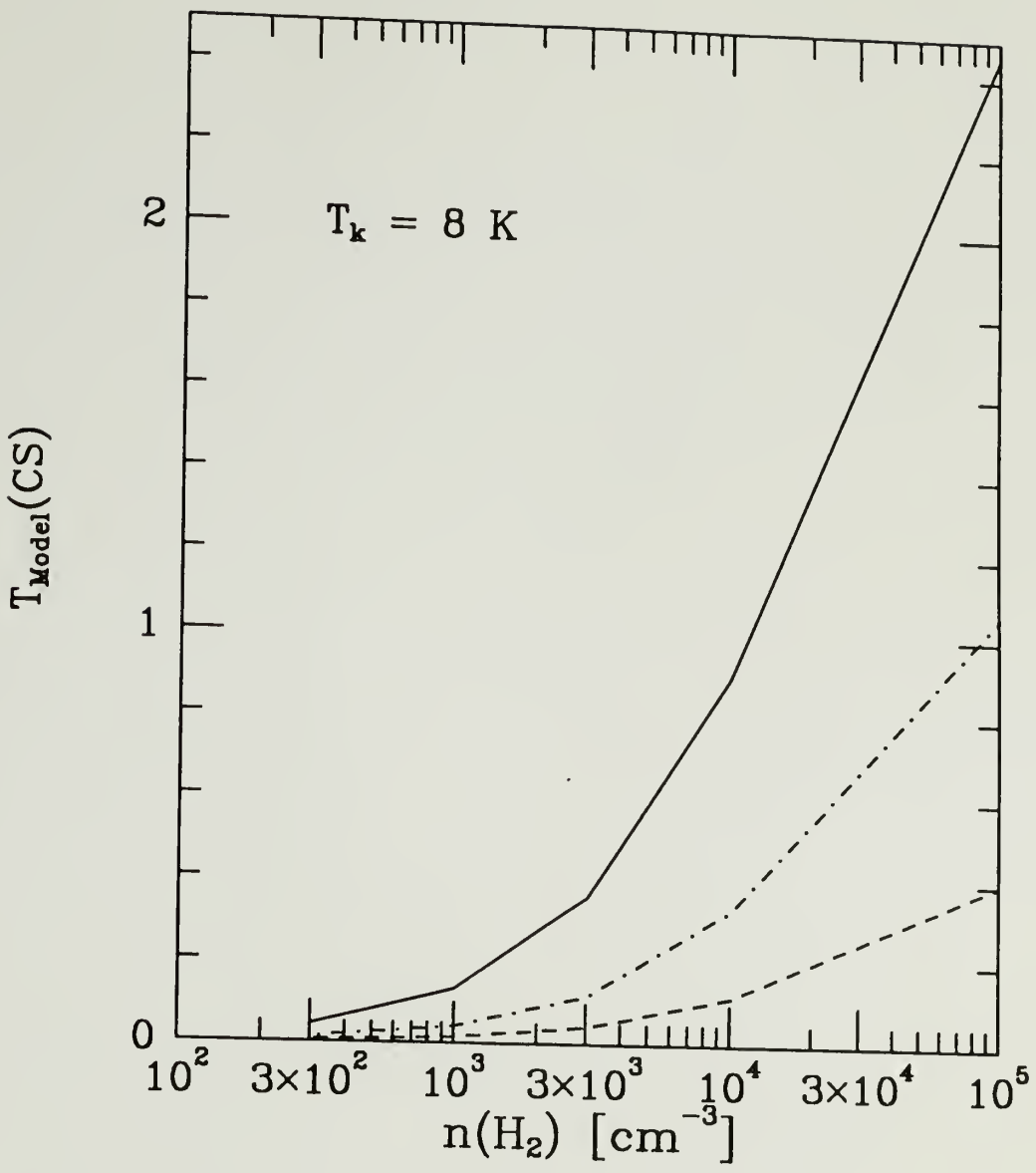

Figure 4.9 The CS antenna temperature predicted by the NLTE model as a function of density for three different column densities: 1×10^{14} (solid line), 3×10^{13} (dot-dashed line), and 1×10^{13} cm^{-3} (dashed line).

Figure 4.10 The ^{12}CO velocity maps of G216-2.5 with 50″ resolution. Two velocity channels are binned together in each map, thus each map has V_{LSR} range of 1.3 km s^{-1}, centered at (a) V_{LSR} = 19.85 km s^{-1} (top), V_{LSR} = 21.15 km s^{-1} (center), and V_{LSR} = 22.45 km s^{-1} (bottom) (b) V_{LSR} = 23.75 km s^{-1} (top), V_{LSR} = 25.05 km s^{-1} (center), and V_{LSR} = 26.35 km s^{-1} (bottom) (c) V_{LSR} = 27.65 km s^{-1} (top), V_{LSR} = 28.95 km s^{-1} (center), and V_{LSR} = 30.25 km s^{-1} (bottom) (d) V_{LSR} = 31.55 km s^{-1} (top), V_{LSR} = 32.85 km s^{-1} (center), and V_{LSR} = 34.15 km s^{-1} (bottom).

(Figure 4.10 continued)

(a)

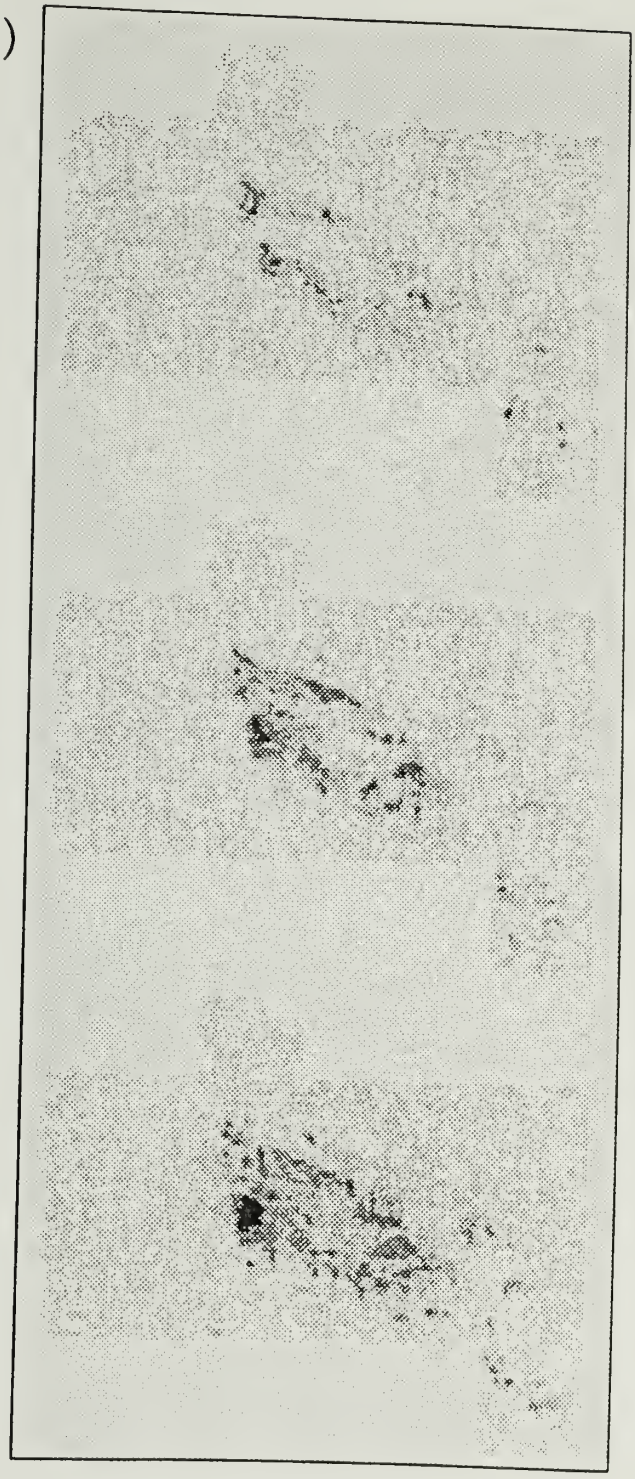

(Figure 4.10 continued)

(b)

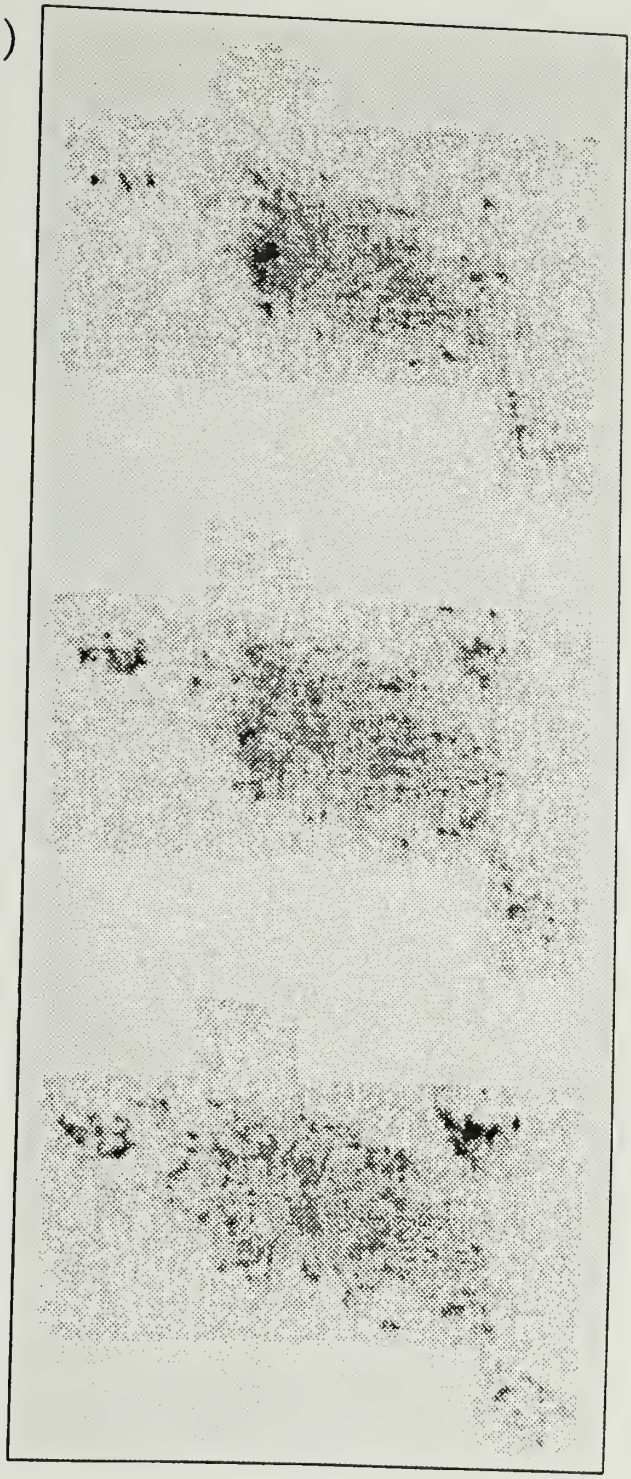

(Figure 4.10 continued)

(c)

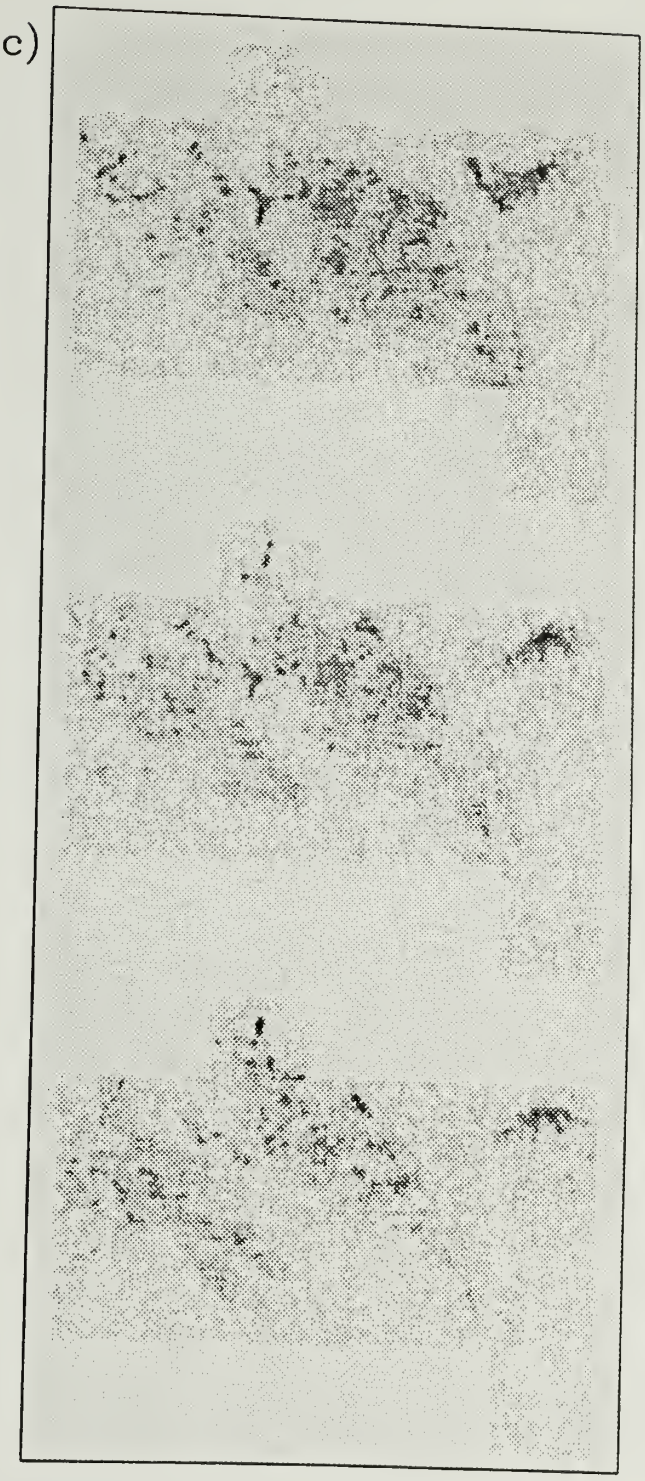

(d)

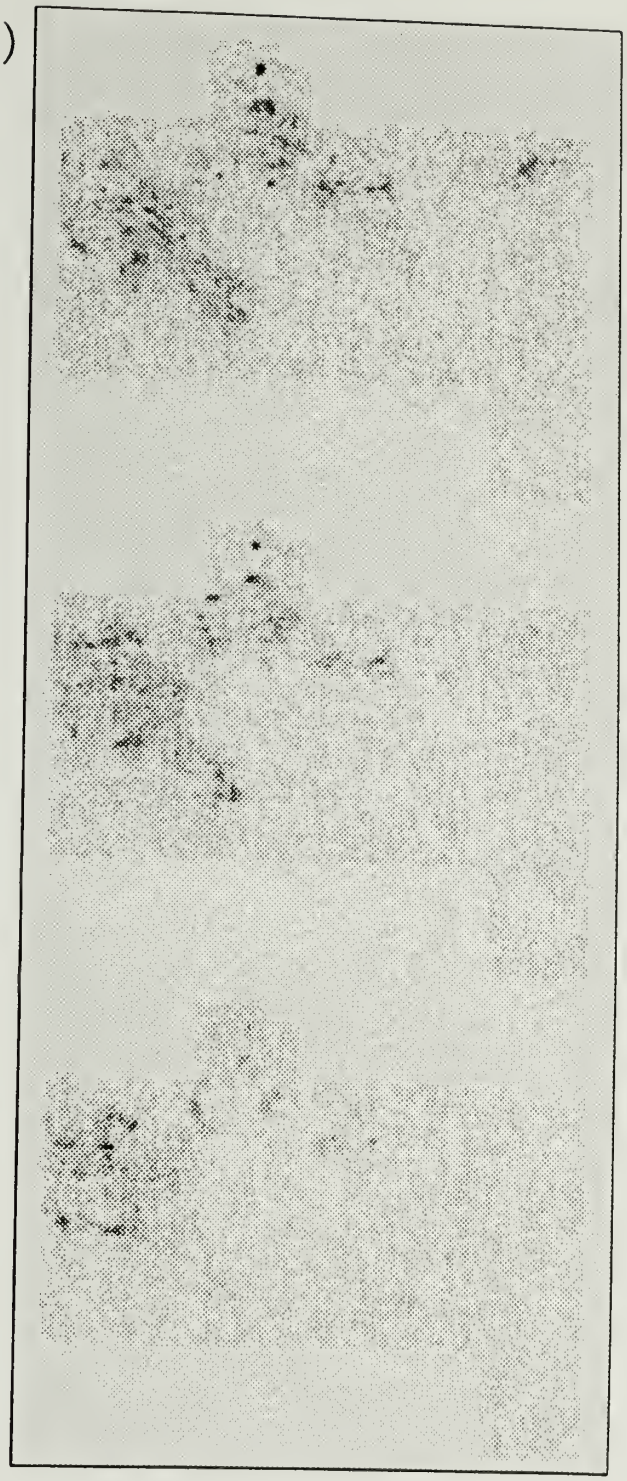

Figure 4.11 A series of ^{12}CO latitude-velocity maps at different Galactic longitudes. The maps are spaced by 20′ in Galactic longitude and the velocity range of each map is 16 to 38 km s^{-1} from left to right.

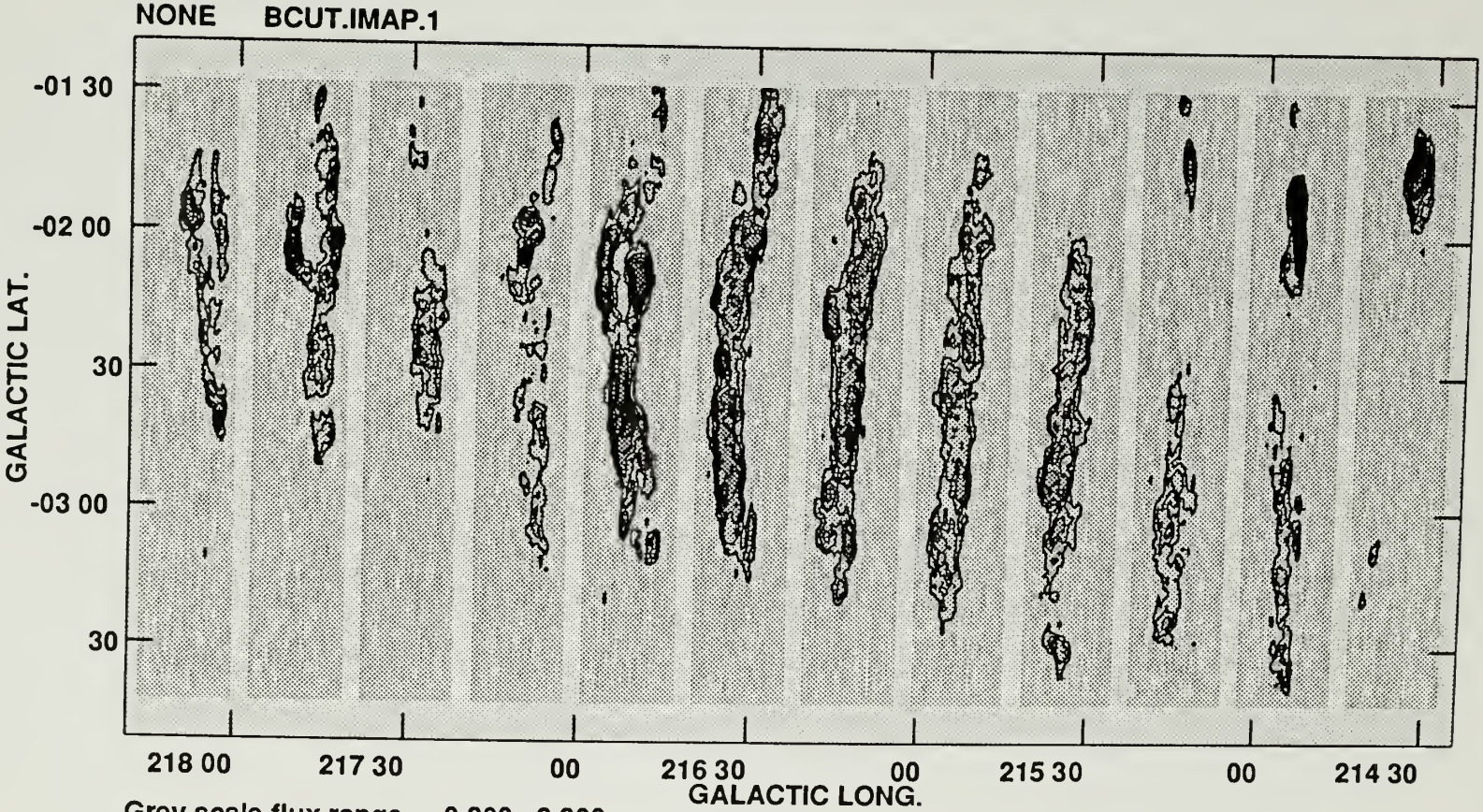

Grey scale flux range= -0.200 2.200
Peak contour flux = 2.4405E+00
Levs = 3.0000E-01 * (1.000, 2.000, 3.000,
4.000, 5.000, 6.000, 7.000)

Figure 4.12 A series of ^{12}CO longitude-velocity maps at different Galactic latitudes. The maps are spaced by 15′ in Galactic latitude and the velocity range of each map is 16 to 38 km s^{-1} from top to bottom.

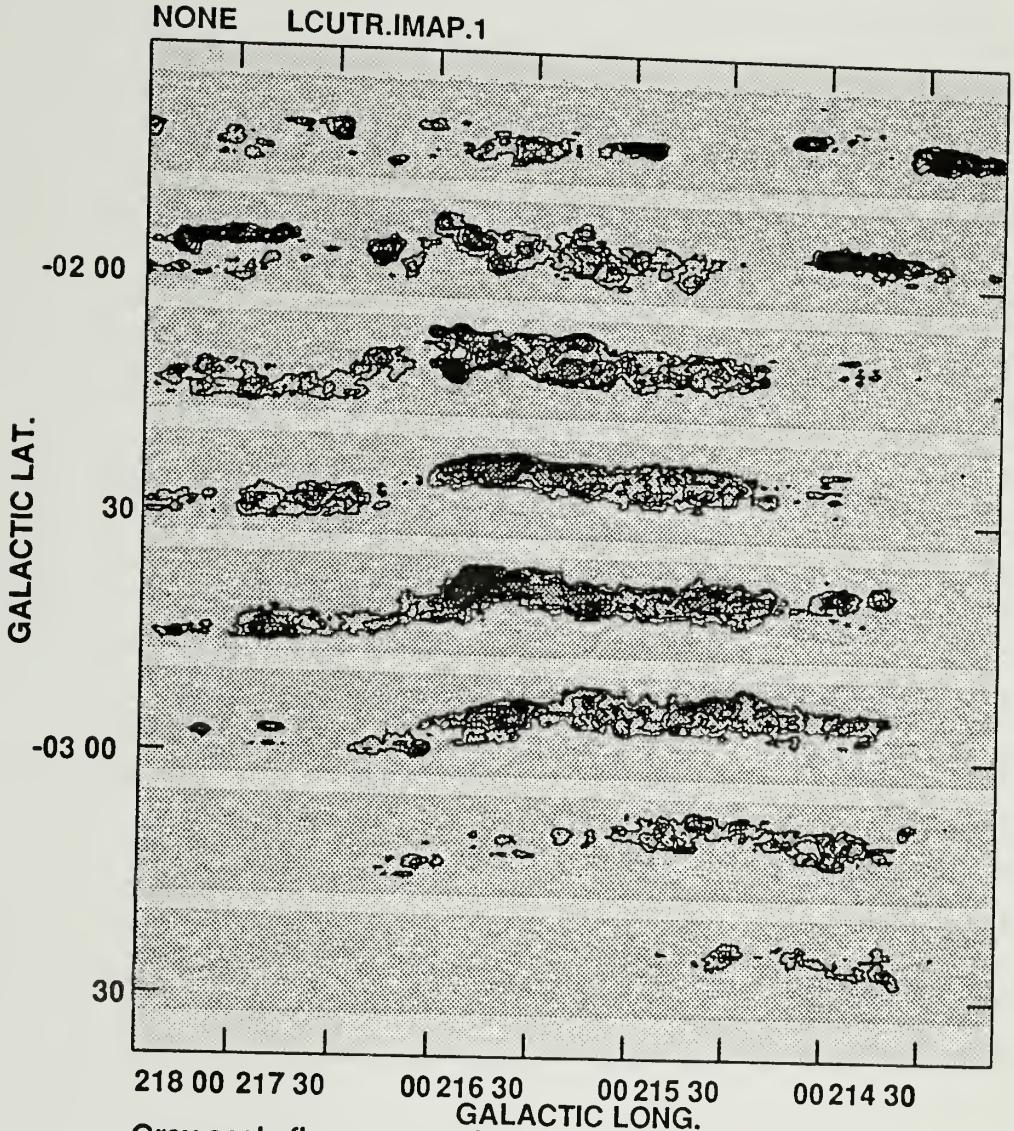

Grey scale flux range= -0.200 2.200
Peak contour flux = 2.4141E+00
Levs = 3.0000E-01 * (1.000, 2.000, 3.000,
4.000, 5.000, 6.000, 7.000)

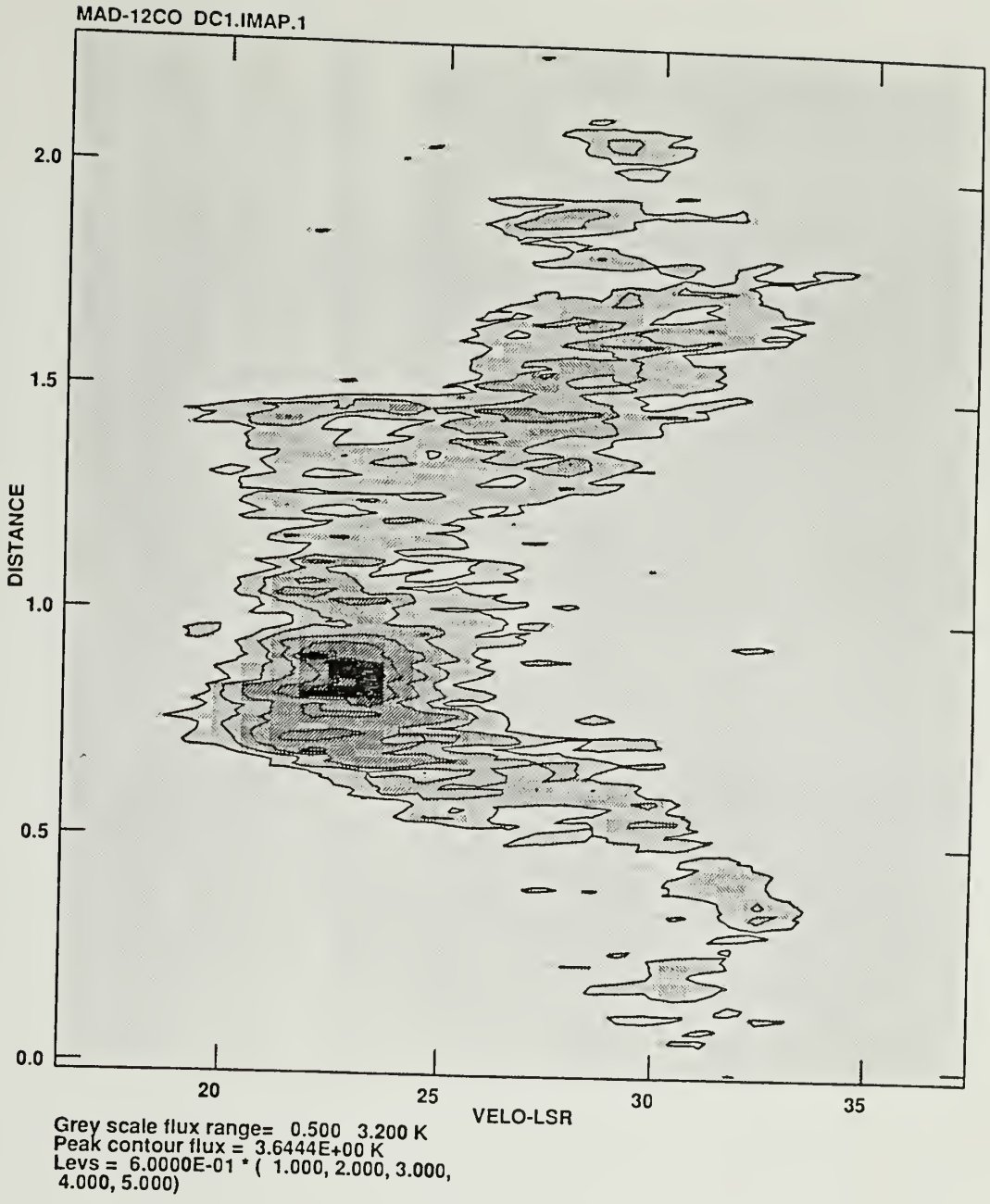

Figure 4.13 A ^{12}CO position-velocity map for the diagonal cut across the main body of G216-2.5. The velocity range is 16 to 38 km s^{-1}, and the position goes from $l = 217°.3$, $b = -3°.4$ (bottom) to $l = 215°.4$, $b = -1°.8$ (top). The lowest contour and increment between contours is 0.6 K.

Figure 4.14 Mean ^{12}CO velocity map. The mean velocity is computed only for the regions where the integrated intensity is greater than 5σ. Darker colors represent higher velocities, and the contour levels span the velocity range 18 to 34 km s^{-1} in 2 km s^{-1} increments.

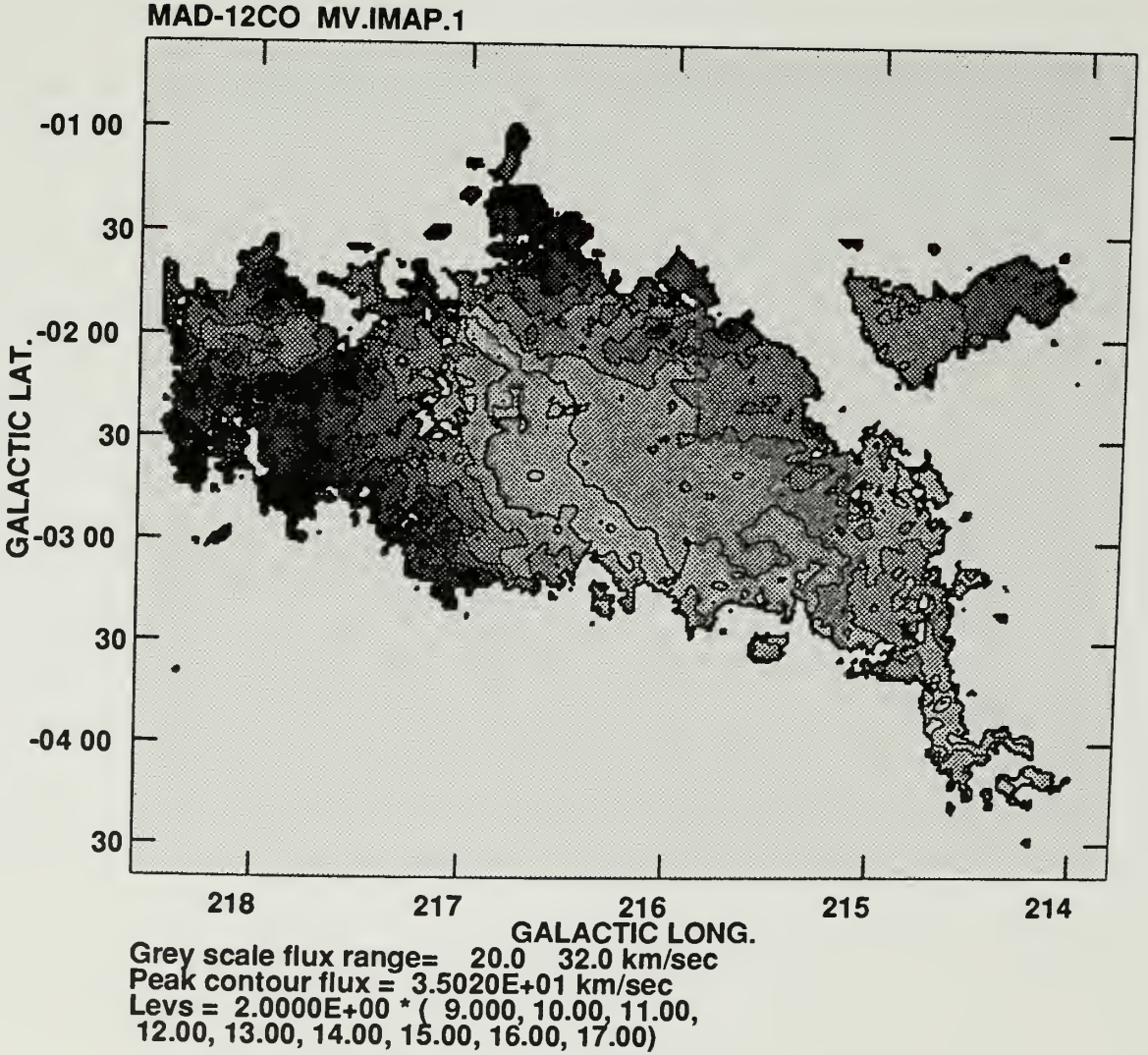
MAD-12CO MV.IMAP.1
-01 00
30
-02 00
30
-03 00
30
-04 00
30
GALACTIC LAT.
218
217
216
215
214
GALACTIC LONG.
Grey scale flux range= 20.0 32.0 km/sec
Peak contour flux = 3.5020E+01 km/sec
Levs = 2.0000E+00 * (9.000, 10.00, 11.00,
12.00, 13.00, 14.00, 15.00, 16.00, 17.00)

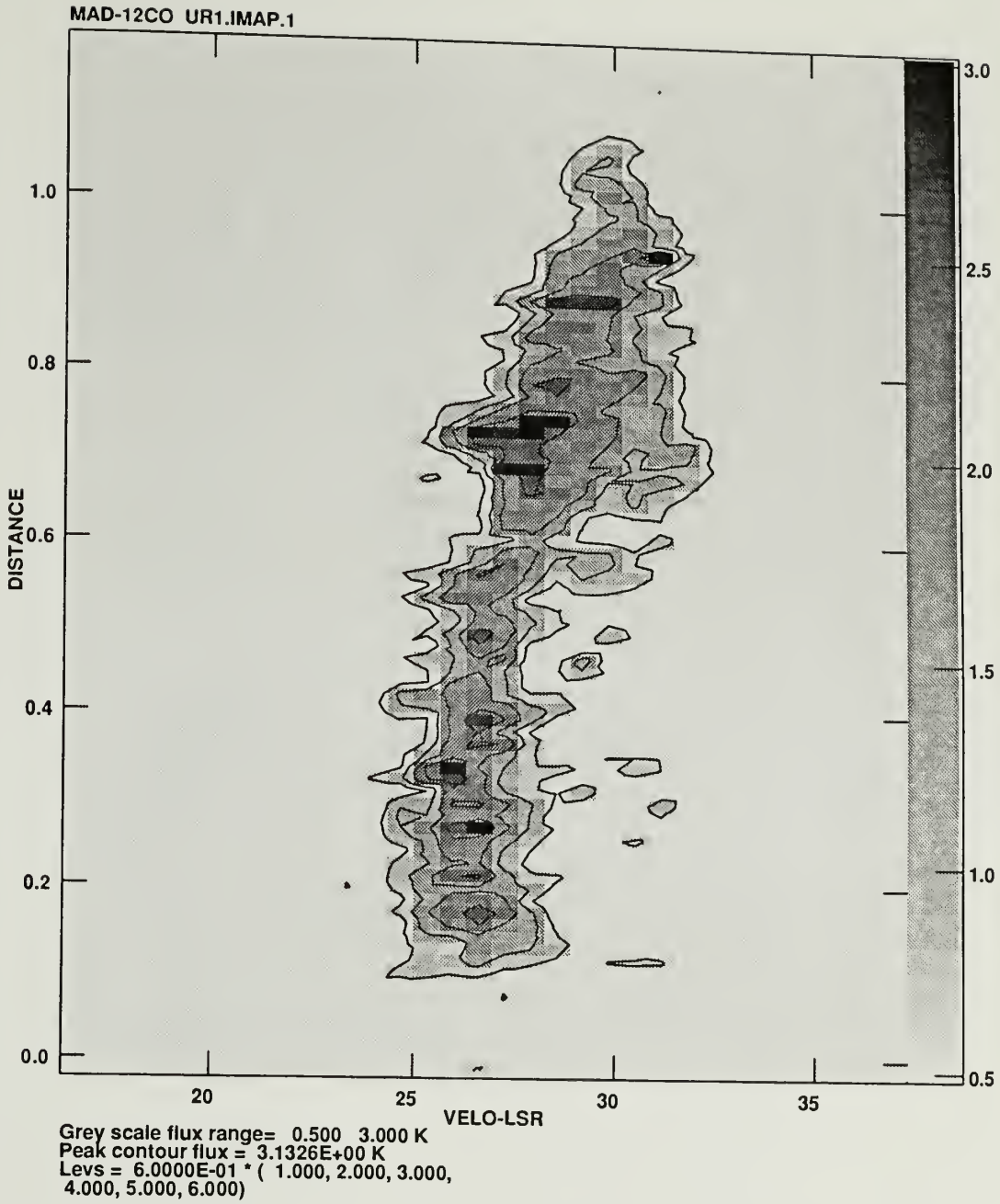

Figure 4.15 A ^{12}CO position-velocity map for a diagonal cut across satellite cloud. Contour levels are the same as Figure 4.13.

Figure 4.16 The ^{12}CO integrated intensity map of S287 and G216-2.5. The grey scale ranges from 0.5 to 16 K km s^{-1}. The lowest contour level is 2 K km s^{-1}, and the increments between contours is 3 K km s^{-1}.

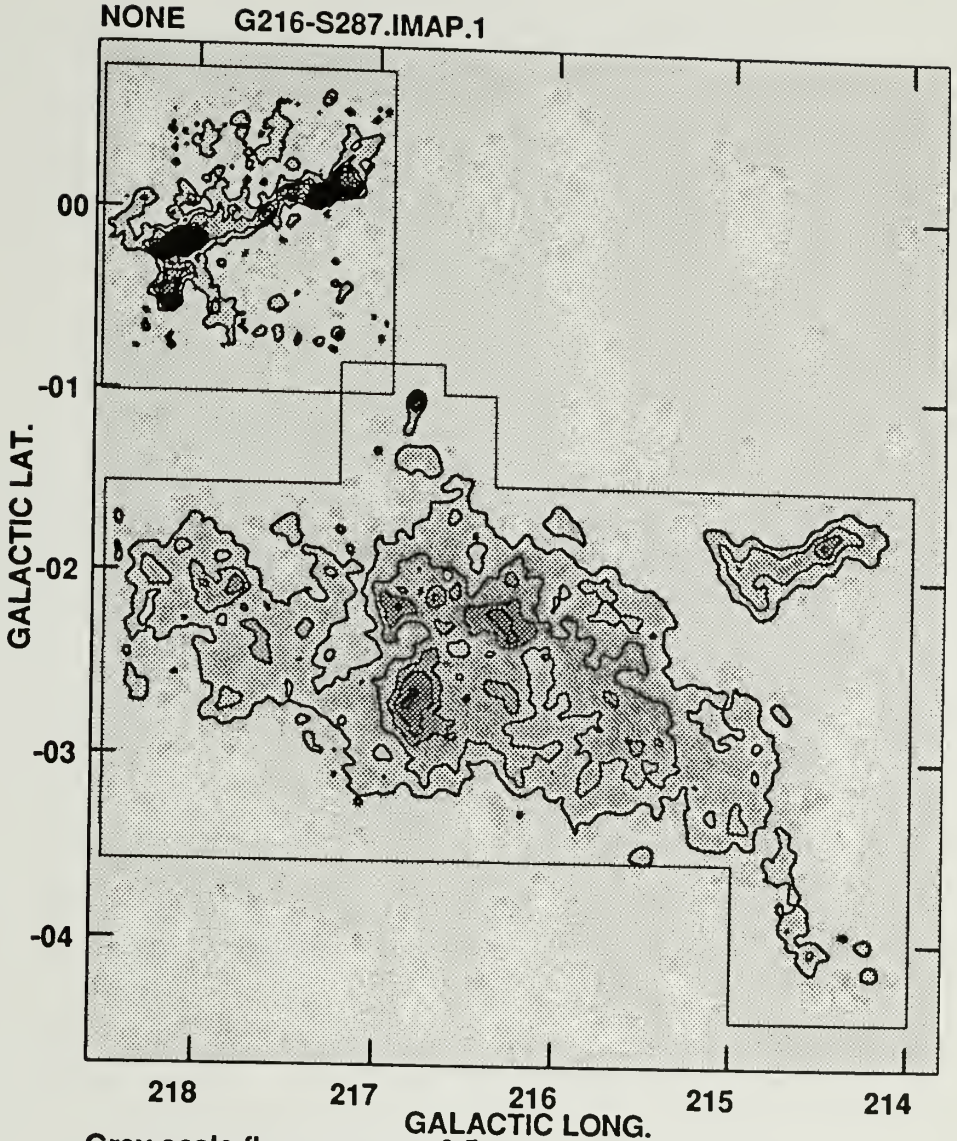

Grey scale flux range= 0.5 16.0
Peak contour flux = 3.0104E+01
Levs = 2.0000E+00 * (1.000, 2.500, 4.000, 5.500, 7.000, 9.000)

Figure 4.17 The ^{12}CO peak antenna temperature map of the molecular cloud associated with the H II region S287. The location of the H II region is marked by the filled triangle at $l = 218°.1$, $b = -°.4$. The grey scale ranges from 0 to 8 K. The contour levels ranges from 1 to 10 K in 1 K increments.

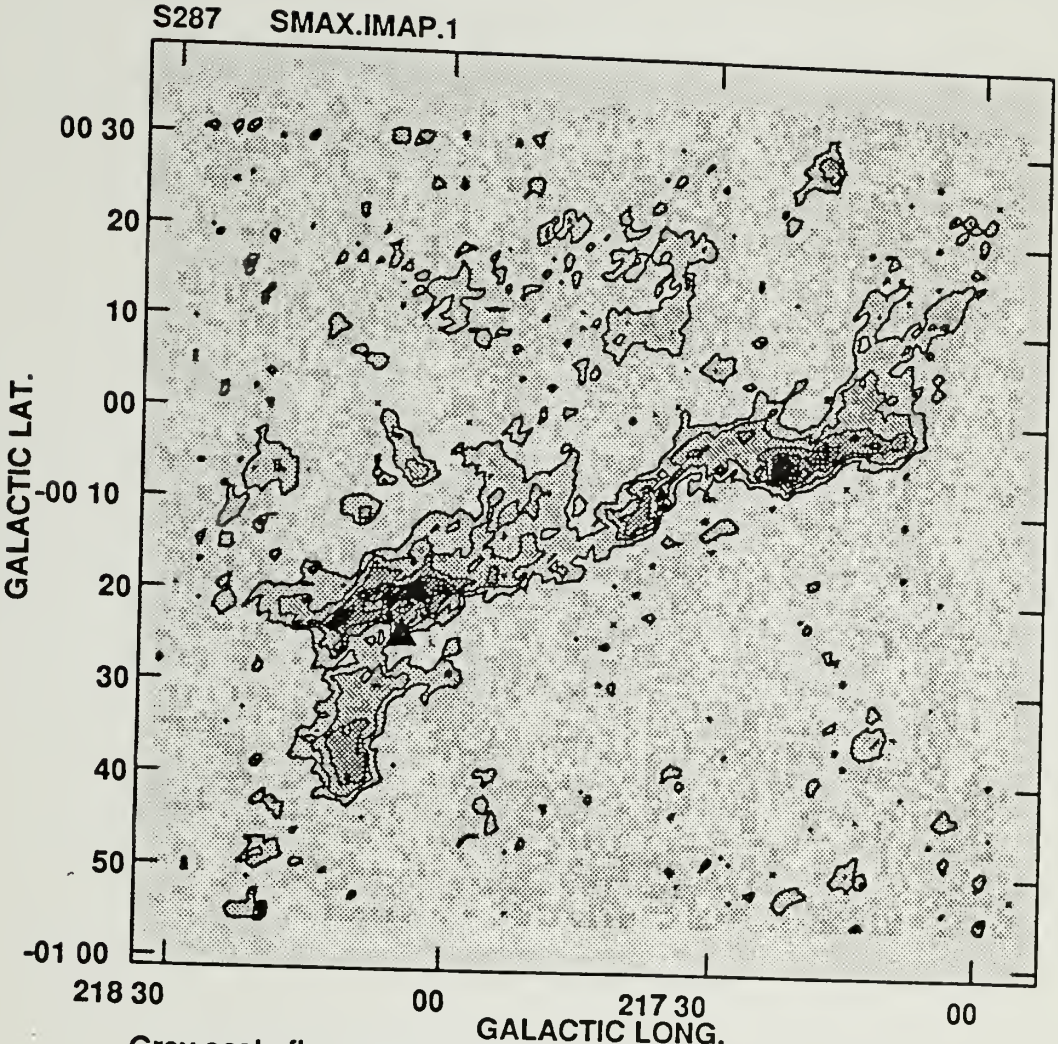

Grey scale flux range= 0.500 8.000 K
Peak contour flux = 1.0216E+01 K
Levs = 1.0000E+00 * (1.500, 3.000, 4.500,
6.000, 7.000, 8.000, 9.000, 10.00)

CHAPTER 5

FAR-INFRARED DATA ANALYSIS

5.1 Introduction

It is believed that dust comprises just a small fraction ($\sim$ 1%) by mass of the interstellar medium in the Galaxy. However, the dust is very effective at absorbing starlight and reemitting this energy at much longer wavelengths, mostly in the far-infrared. Thus information on embedded stars as well as properties of the dust can be extracted from the far-infrared (FIR) emission. The relationship between the dust emission in the infrared, the dust absorption at visible and ultraviolet wavelengths, and the column density of carbon monoxide in interstellar clouds deserves study for a number of reasons. First, carbon monoxide emission and the infrared emission from dust both should be useful tracers of the distribution of mass within molecular clouds. Second, the infrared and carbon monoxide emission can be used to investigate models of interstellar grains, grain heating mechanisms, and the photochemistry of carbon monoxide. Third, both infrared continuum emission from dust and carbon monoxide spectral line emission can be used to estimate the mass of interstellar clouds, and the FIR data can be compared for consistency and/or calibration with that of the carbon monoxide.

In the following sections, we will use the FIR data obtained from IRAS to identify young stellar objects associated with G216-2.5 and to correlate the dust and the CO emission. The temperature and the mass of dust will also be estimated.

5.2 Point Sources

All sources in the IRAS Point Source Catalog (Lonsdale *et al.* 1985) with 100 μm flux densities greater than 13 Jy found within the region mapped around G216-2.5 have been identified. The sources, with their positions in Galactic coordinates (1950 epoch), their 12, 25, 60, and 100 μm flux densities, are tabulated in Table 5.1. The first 10 sources are located within the boundary of the CO emission and the rest of them (10 objects) are outside the CO boundary. These sources are presented in Figure 5.1 overlayed on ^{12}CO intensity map. The location of the IRAS point sources are indicated on an outline of the CO emission from G216-2.5, the plus signs are the sources images in the near-infrared and one source (06401-0318) that lie within the boundary of the cloud, and filled circles are those sources that lie outside boundary of the cloud. FIR luminosities were calculated for each of these sources using the following equation (Lonsdale *et al.* 1985):

$$L_{FIR} = 4\pi d^2[1.26R(1.00 \times 10^{12} S_{100} + 2.58 \times 10^{12} S_{60})], \qquad (5.1)$$

where S_ν is the flux density at IRAS band ν, d is the distance to the object, and R is the color correction factor. Luminosities were obtained assuming that the distance of IRAS point sources is 2.2 kpc; the color corrections and FIR luminosities are presented in Table 5.1.

A color-color diagram (S_{25}/S_{12} vs S_{60}/S_{25}) for all of these IRAS sources is presented in Figure 5.2. The filled circles are the IRAS point sources seen toward G216-2.6, and the open circles are sources outside the CO boundary of the cloud. The location of the embedded core sources (solid-outlined box) and T Tauri stars (dashed-outlined box) in the color-color diagram are also indicated (Emerson 1985). The big asterisk represents the average value for T Tauri stars given by Walker *et al.* (1989). Figure 5.2 shows that four of these objects associated with G216-2.5 have colors similar to embedded protostars (these are first four objects in Table 5.1). These objects will be discussed in more detail in the next Chapter.

5.3 Extended Emission

5.3.1 Correlation with CO Emission

An accurate separation of the Galactic background FIR emission from the cloud emission is necessary to use the IRAS data to estimate the FIR luminosity of the cloud accurately. To do this, the cloud was divided into four regions according to the degree of contamination and spatial location: Region I is comprised of the part of G216-2.5 contaminated by the emission from the two H II regions, S286 and S287, and is at $l = 216°$ to $218°.5, b = -0°.5$ to $-2°.4$. Region II is a small satellite cloud centered at $l = 214°.5, b = -1°.7$. Region III is very small but has the strongest CO emission within the map and is centered at $l = 216°.8, b = -1°.05$. Region IV is the remaining part of the cloud, which has little contamination by S286 and

Table 5.1 FIR flux densities and luminosities of IRAS point sources. R is the color correction factor.

Name	l	b	S_{12}	S_{25}	S_{60}	S_{100}	R	$L_{FIR}[L_\odot]$
06453-0209*	214.49	-1.81	1.12	6.10	22.21	36.86	1.385	188.9
06522-0350*	216.79	-1.04	1.45	3.56	23.12	69.62	1.60	299.5
06471-0329*	215.89	-2.01	1.82	6.46	15.85	23.79	1.378	129.1
06481-0517*	217.60	-2.62	1.51	7.58	20.06	32.05	1.38	167.5
06416-0352*	215.60	-3.41	0.74	1.02	10.63	26.11	1.48	114.7
06428-0257*	214.93	-2.72	1.08	1.40	17.28	38.41	1.45	174.3
06471-0353*	216.24	-2.19	0.50	0.54	7.38	26.24	1.70	111.5
06492-0349*	216.43	-1.72	0.27	0.47	9.82	30.56	1.62	131.1
06507-0519*	217.93	-2.07	0.58	0.53	8.31	31.26	1.74	132.8
06401-0318*	214.92	-3.48	0.54	0.59	10.74	36.77	1.69	157.8
06404-0414	215.78	-3.85	-0.25	0.24	6.67	25.47	1.74	107.5
06405-0356	215.53	-3.67	0.31	0.65	4.38	13.75	1.63	59.1
06424-0237	214.58	-2.67	0.67	0.75	4.69	13.76	1.60	59.9
06435-0153	214.06	-2.09	-0.25	0.47	8.80	27.00	1.62	116.6
06450-0619	218.18	-3.77	-0.25	0.25	5.57	16.52	1.60	71.6
06452-0601	217.93	-3.60	0.52	0.85	6.79	18.48	1.54	80.3
06486-0110	214.02	-0.61	0.48	0.54	5.88	23.50	1.78	99.7
06514-0424	217.19	-1.50	0.52	0.45	4.46	15.44	1.68	65.6
06519-0424	217.26	-1.38	0.45	0.41	6.80	39.85	2.30	191.1
06520-0428	217.32	-1.37	1.59	2.88	32.76	132.60	1.79	563.0

S287. These four regions are marked on a map of the 100 μm intensity truncated at the 5σ detection level of the CO integrated intensity (Figure 5.3).

A good correlation is found between the FIR emission in Region IV and the ^{12}CO integrated intensity (Figure 5.4 and Figure 5.5). Pixels with ^{12}CO integrated intensity above 7 K km s^{-1} have been fit by least-squares to determine the relation between CO integrated intensity and FIR flux, the equation of the fitted lines are given below and illustrated in Figure 5.4 and Figure 5.5:

$$I_{100} = 0.36 I_{^{12}CO} + 20.411 \tag{5.2}$$

$$I_{60} = 0.058 I_{^{12}CO} + 1.549 \tag{5.3}$$

The non-zero intercept values most likely represents emission from dust that lies in front of or behind G216-2.5, and therefore is unrelated to G216-2.5 and should be subtracted off. The slope represents the true relation between ^{12}CO integrated intensity and FIR intensity.

The relation between ^{12}CO integrated intensity and FIR intensity are shown in Figure 5.6 and Figure 5.7 for Region II. A good correlation is also found for most of the positions in this region, however, the positions associated with the IRAS point sources are obvious. The least square fitted lines to both the 100 and 60 μm data (shown in Figure 5.6 and Figure 5.7) are given by:

$$I_{100} = 0.343 I_{^{12}CO} + 24.944 \tag{5.4}$$

$$I_{60} = 0.035 I_{^{12}CO} + 2.879, \tag{5.5}$$

Region III has too few points to attempt any correlation and in addition the FIR emission is dominated by the IRAS point source. The correlation between FIR

emission and ^{12}CO integrated intensity in Region I is presented in Figure 5.8 and Figure 5.9. No correlation is found, however, this is not surprising since the region is severely contaminated by the two H II regions. The solid line in Figure 5.8 and Figure 5.9 are the fits found for the Region IV. Most of the points lie above this line supporting the idea that most of the FIR emission does not arise from G216-2.5, but from the H II region S286 that lies behind G216-2.5.

A number of authors have found a linear relationship between 100 μm intensity and either the H I column density in regions of atomic gas or the CO column density in molecular clouds (Boulanger and Pérault 1988; Snell, Heyer, and Schloerb, 1989). Boulanger and Pérault (1988) found ratios between the 100 μm intensity and CO integrated intensity in the range 0.6 to 2.5 (MJy/sr)/(K km s^{-1}) with an average value of 1.4 (MJy/sr)/(K km s^{-1}) for regions outside of star forming sites. This value can be compared with the average slope found for G216-2.5 of 0.36 (MJy/sr)/(K km s^{-1}). Based on the slope of the least-squares fit to the data, we have computed the ratio of 100 μm intensity to total hydrogen column density. The hydrogen column density was calculated using the conversion factor given by the γ-ray analysis (Bloemen 1989), of 2.3×10^{20} H$_2$ cm^{-2} (K km s^{-1})$^{-1}$. Expressing this ratio in terms of the hydrogen, the values found are $I_{100\mu m}$/N(H) = 0.08 MJy/sr (10^{20} H cm^{-2})$^{-1}$ and $I_{60\mu m}$/N(H) = 0.013 MJy/sr (10^{20} H cm^{-2})$^{-1}$. These values can be compared to those for dark clouds; $I_{100\mu m}$/N(H) is 0.07 for B18, and 0.10 for HCL2, and $I_{60\mu m}$/N(H) of both B18 and HCL2 are 0.012 MJy/sr (10^{20} H cm^{-2})$^{-1}$ (Snell, Heyer, and Schloerb 1989). The values for warmer GMCs are totally different; for example in Orion: $I_{100\mu m}$/N(H) = 1.3 and $I_{60\mu m}$/N(H) = 0.27 MJy/sr (10^{20}

H $cm^{-2})^{-1}$ (Boulanger and Pérault 1988). The values for Orion are a factor of 20 larger than that found in G216-2.5. Snell, Heyer, and Schloerb (1989) attributed this low value of the ratio to dust heated exclusively by the interstellar radiation field. In fact, the dominant heating source for the dust in IR-quiet clouds was also attributed to the interstellar radiation field (Mooney 1992). Thus, these facts may support the hypothesis that G216-2.5 is heated by only the interstellar radiation field. More detailed discussion of dust heating will be presented in Chapter 7.

5.3.2 Dust Temperature and Mass

The temperature of interstellar dust is thought to be determined by a balance between radiative processes. Heating occurs primarily by the absorption of stellar UV photons, and cooling by reradiation in the FIR.

A dust color temperature using the integrated flux density ratio at 60 and 100 μm can be defined by using the following equation, assuming a dust emissivity law proportional to $\lambda^{-\beta}$:

$$\frac{S_{100}}{S_{60}} = \left(\frac{\lambda_{100}}{\lambda_{60}}\right)^{3+\beta} \left[\frac{\exp(hc/\lambda_{60}k\overline{T_d}) - 1}{\exp(hc/\lambda_{100}k\overline{T_d}) - 1}\right]. \tag{5.6}$$

However, this expression does not include the color correction for the IRAS data. While the color corrections could be made iteratively, we have used the tabulated values provided by Lonsdale *et al.* (1985). Hildebrand (1983) estimated the emissivity index $\beta = 1$ for $\lambda = 50$ to 250 μm, and $\beta = 2$ for $\lambda > 250$ μm. Cox and Mezger (1989) assumed $\beta = 2$ for $\lambda > 100$ μm, and $\beta = 1.5$ for $\lambda = 40 - 100$ μm. Here we adopt $\beta = 1$. The ratio of the 60 μm integrated flux density to the 100

μm integrated flux density is 0.21. The dust temperature obtained from this ratio is 26 K.

The average flux density ratio from star forming clouds is 0.53 (Carpenter, Snell, and Schloerb 1990) and corresponds to a color temperature of 37 K. Thus, the dust in G216-2.5 is much colder than in star forming GMCs. Even in the H II region S287 the flux density ratio is 0.34. The dust temperature of G216-2.5 can also be compared with the large scale of GMCs studied by Mooney (1992). Mooney arbitrarily divided GMCs into two groups, IR-strong GMCs, and IR-quiet GMCs, and obtained dust temperature of 37 K for IR-strong clouds, and 31 K for IR-quiet clouds. The dust temperature of G216-2.5 is even lower than the average for the IR-Quiet clouds in the inner Galaxy.

We can now investigate the efficiency of the FIR emission as a tracer of the mass of G216-2.5. The mass of radiating dust can be estimated using the expression given by Hildebrand (1983); based on the integrated flux density at 100 μm, S_{100}, and the average dust temperature, T_d, the mass of the dust is given by:

$$M_d = \frac{S_{100} d^2}{B(\nu, T_d)} \frac{4 < a > \rho}{Q_{100}} \frac{}{3} \quad [M_\odot] \tag{5.7}$$

where d is distance of cloud, Q_{100} is emission efficiency at 100 μm, and B(ν, T_d) is Planck function. If it is assumed that the dust grains have a mean size $< a > \sim 10^{-5}$ cm, a dust density $\rho \sim 3$ gm cm^{-3}, and an emission efficiency, $Q_{100} \sim 10^{-3}$, the estimated dust mass of the cloud is $\sim 50\ M_\odot$, or about 1/2000 of the gas mass. The canonical value of the dust to gas ratio by mass is $\sim 1/100$, thus the small

dust mass fraction implies that there must be a substantial amount of colder dust that is not emitting at IRAS wavelength bands.

5.3.3 Infrared Luminosity

After subtracting the foreground and background Galactic emission, the total FIR flux of the cloud can be estimated from the uncontaminated portions of Region II, and IV. We assumed that Region I has the same emission characteristics as the other regions, and have applied the relation between CO and FIR intensity to estimate the flux density. This assumption is likely to be good since there is no conspicuous star formation associated with any parts of this cloud. The integrated FIR flux density of G216-2.5 is estimated to be 4130 Jy at 100 μm, and 850 Jy at 60 μm.

The total FIR luminosity $L_{IR}(tot)$ of the cloud was calculated according to the method described in the *Catalogued Galaxies and Quasars Observed in the IRAS Survey* (Lonsdale *et al.* 1985) using the 60 and 100 μm integrated flux intensities. The total FIR luminosity is given by:

$$L_{IR}(tot) = 4\pi d^2 F_{IR}(tot) \tag{5.8}$$

where d is the distance to the cloud, 2.2 kpc, and $F_{IR}(tot)$ is the total IR flux from 1 to 500 μm.

The FIR flux between λ = 42.4 - 122.5 μm can be estimated by:

$$F_{IR} = 1.26 \times 10^{-26}(S_{100}\Delta\nu_{100} + S_{60}\Delta\nu_{60}) \quad [Wm^{-2}], \tag{5.9}$$

where the source flux densities are in the unit of Janskys, and IRAS 60 and 100 μm bandwidths are $\Delta\nu$ = 2.58 $\times 10^{12}$ Hz, and $\Delta\nu$ = 1.0 $\times 10^{12}$ Hz, respectively.

The total FIR flux can then be extrapolated by assuming that the dust has a single temperature, $\overline{T_d}$. The correction factor $R(\overline{T_d}, \beta)$ for extrapolation is explicitly expressed as:

$$R(\overline{T_d}, \beta) = \frac{\int_{x_1}^{x_2} \frac{x^{3+\beta}}{e^x - 1} dx}{\int_{x_3}^{x_4} \frac{x^{3+\beta}}{e^x - 1} dx}, \tag{5.10}$$

where $x_n = (hc/\lambda_n k\overline{T_d})$, $\lambda_1 = 1$ μm, $\lambda_2 = 500$ μm, $\lambda_3 = 42.5$ μm, and $\lambda_1 = 122.5$ μm.

The total FIR luminosity can now be expressed as:

$$L_{IR}(tot) = 0.394 R(\overline{T_d}, \beta)(S_{100} + 2.58 S_{60}) D^2 \quad [L_\odot] \tag{5.11}$$

for D in kpc, and S_{100} and S_{60} in Janskys. Thus, the estimated IR luminosity of G216-2.5 is 2.4×10^4 $L_\odot$. The FIR luminosity to mass ratio 0.05 and 0.24, is much smaller than found in most star forming molecular clouds (Mooney 1992).

Figure 5.1 IRAS point sources overlayed on the ^{12}CO integrated intensity map. The contour represents the 3σ noise level of the ^{12}CO intensity. The plus signs are the sources on the face of G216-2.5, and the filled circles are beyond the boundary of the molecular cloud.

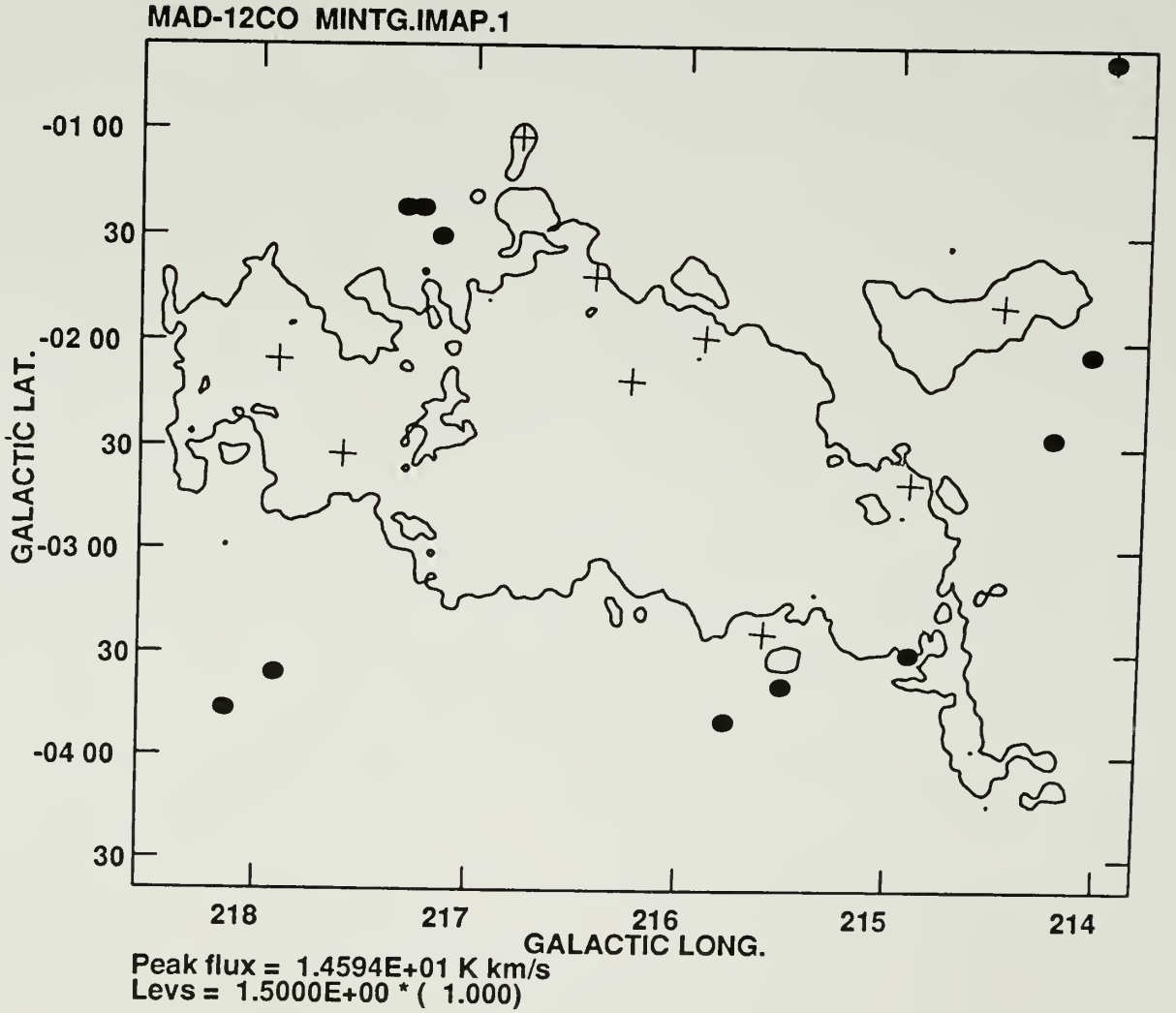
MAD-12CO MINTG.IMAP.1
-01 00
30
-02 00
30
-03 00
30
-04 00
30
GALACTIC LAT.
218
217
216
215
214
GALACTIC LONG.
Peak flux = 1.4594E+01 K km/s
Levs = 1.5000E+00 * (1.000)

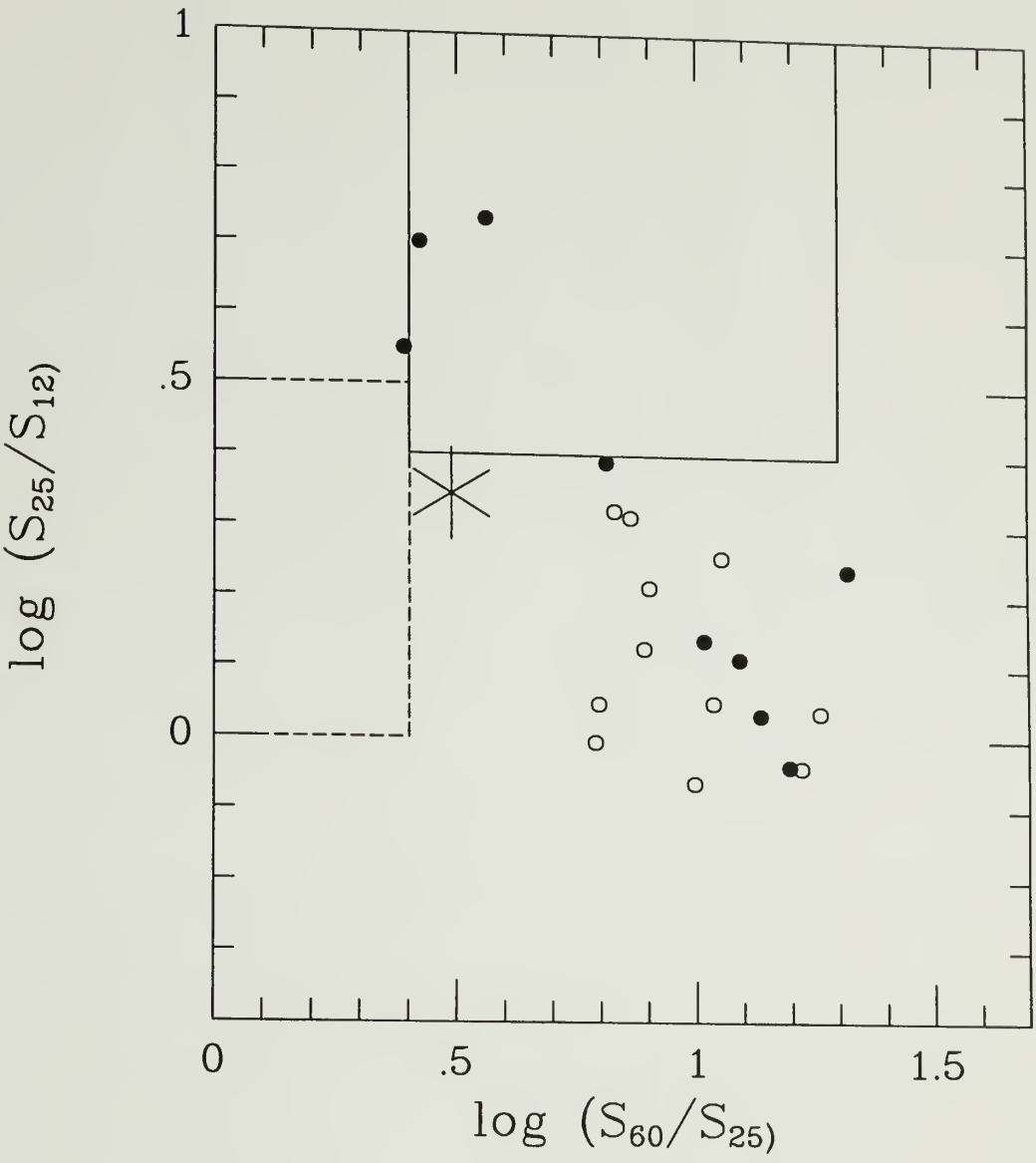

Figure 5.2 Color-color diagram for IRAS point sources. Filled circles present IRAS point sources toward G216-2.5, and open circles are beyond the boundary of the cloud. The solid-outlined box indicates the location of embedded cores, and dashed-outlined box indicates the location of T Tauri stars (Emerson 1985). The asterisk represents the average colors for T Tauri stars (Walker *et al.* 1989).

Figure 5.3 The 100 μm intensity image divided into four regions. The image was truncated at the 5σ noise level of the ^{12}CO integrated intensity. Contours are the same as the those of Figure 2.5.

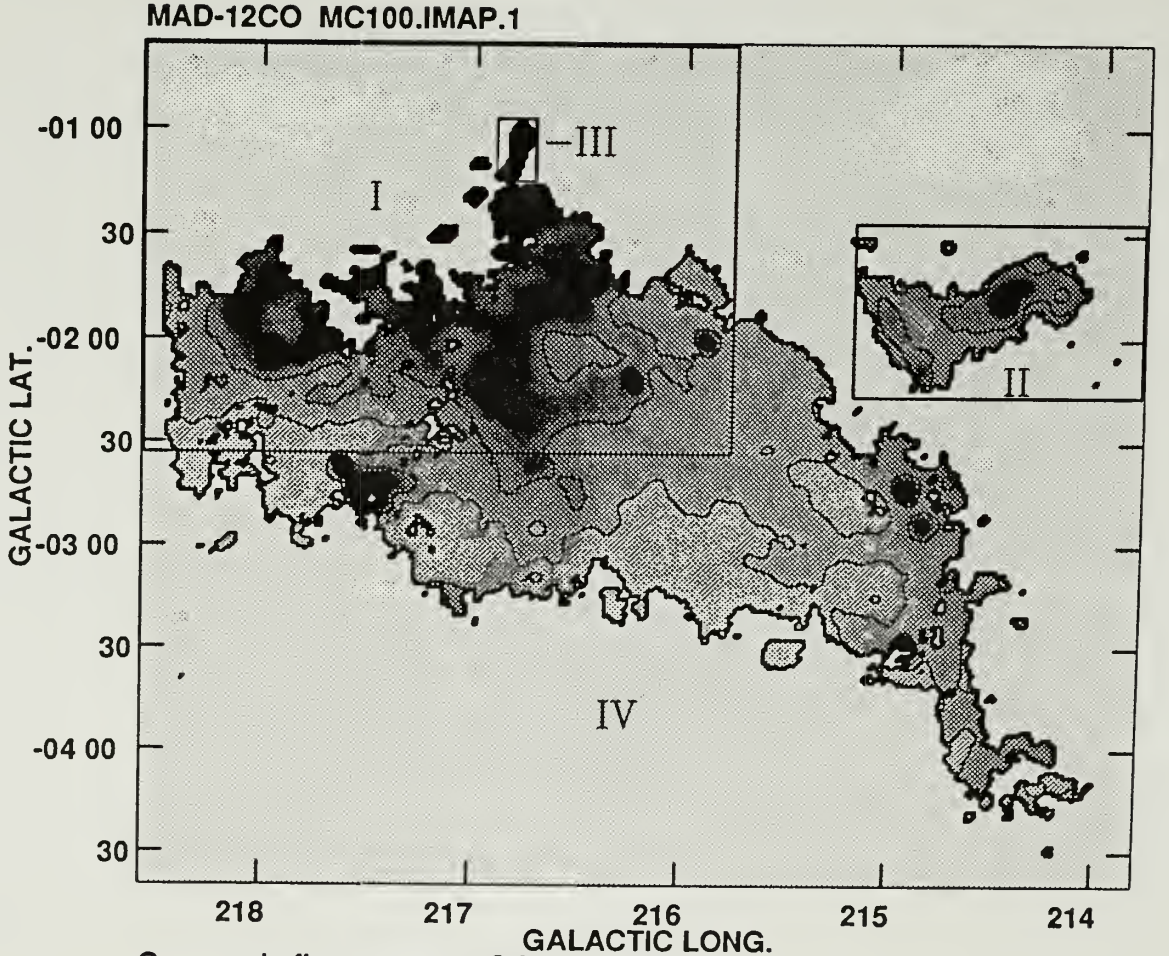
MAD-12CO MC100.IMAP.1
-01 00
30
-02 00
30
-03 00
30
-04 00
30
GALACTIC LAT.
218
217
216
215
214
GALACTIC LONG.
I
II
III
IV
Grey scale flux range= 2.0 18.0 MJy/ster
Peak contour flux = 5.8133E+01 MJy/ster
Levs = 2.0000E+00 * (1.000, 3.000, 5.000,
7.000, 9.000, 11.00)

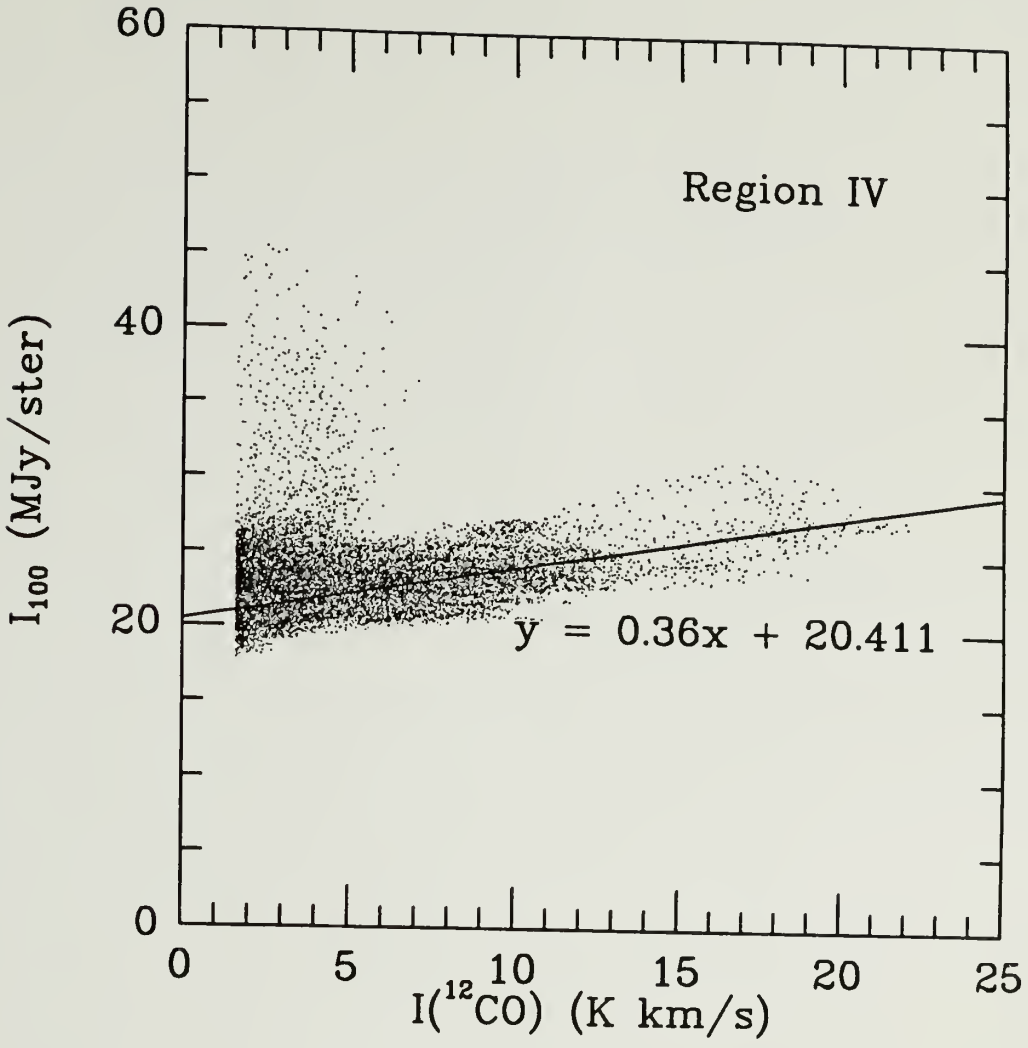

Figure 5.4 The 100 μm Intensity as a function of $I_{^{12}CO}$ for Region IV. Points with $I_{^{12}CO}$ greater than 7 K km s^{-1} were fitted by least squares and the fitted line is shown.

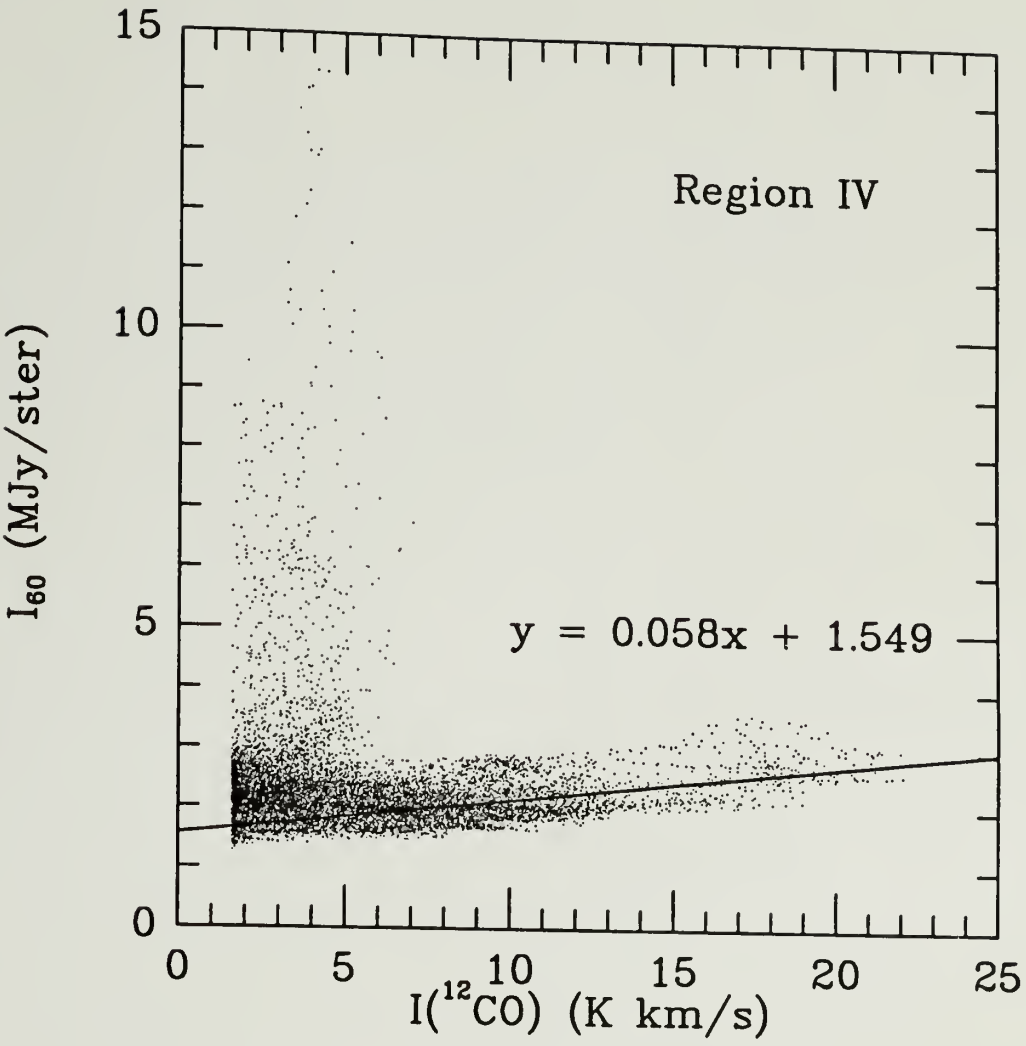

Figure 5.5 The 60 μm Intensity as a function of $I_{^{12}CO}$ for Region IV. Points with $I_{^{12}CO}$ greater than 7 K km s^{-1} were fitted by least squares and the fitted line is shown.

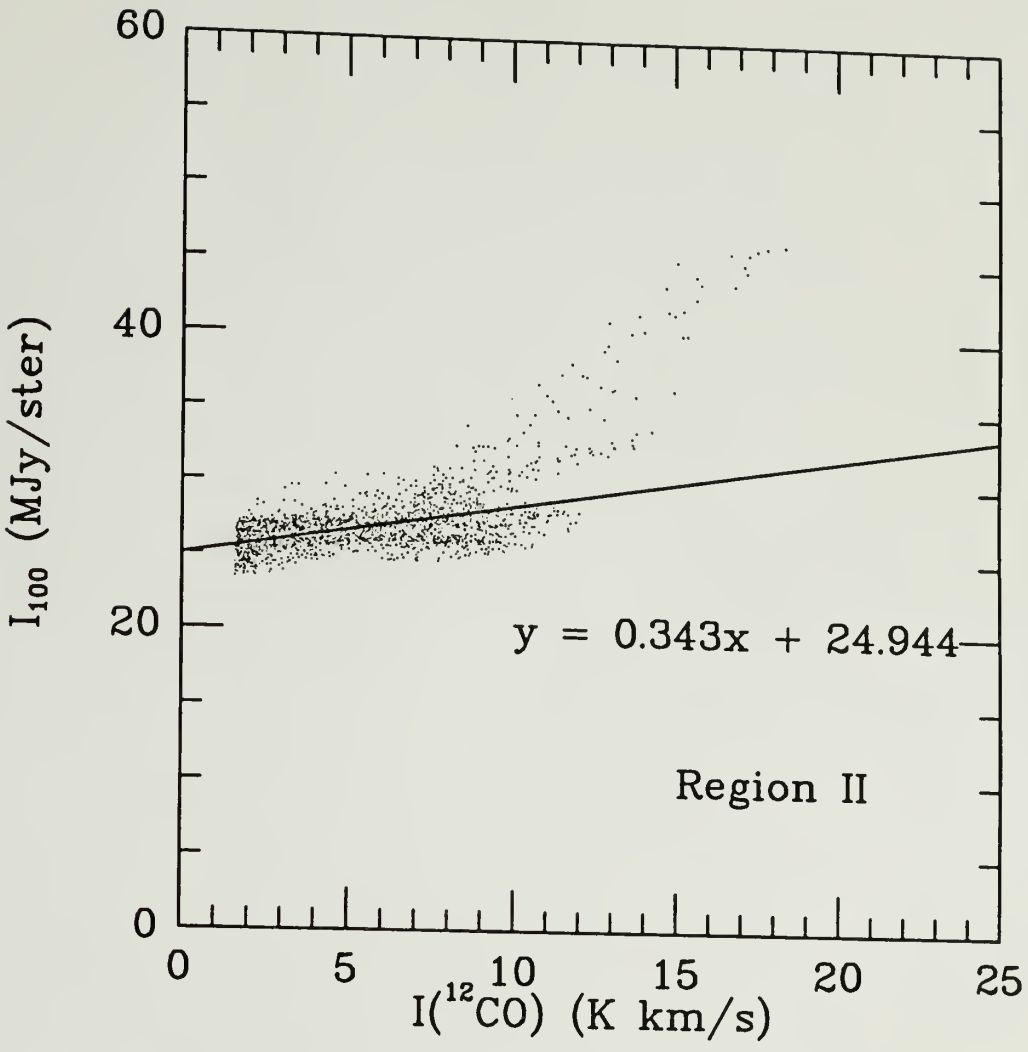

Figure 5.6 The 100 μm Intensity as a function of $I_{^{12}CO}$ for Region II. Points with $I_{^{12}CO}$ greater than 7 K km s^{-1} were fitted by least squares and the fitted line is shown. The points that substantially lie above the fitted line are due to the IRAS point source 06453-0209.

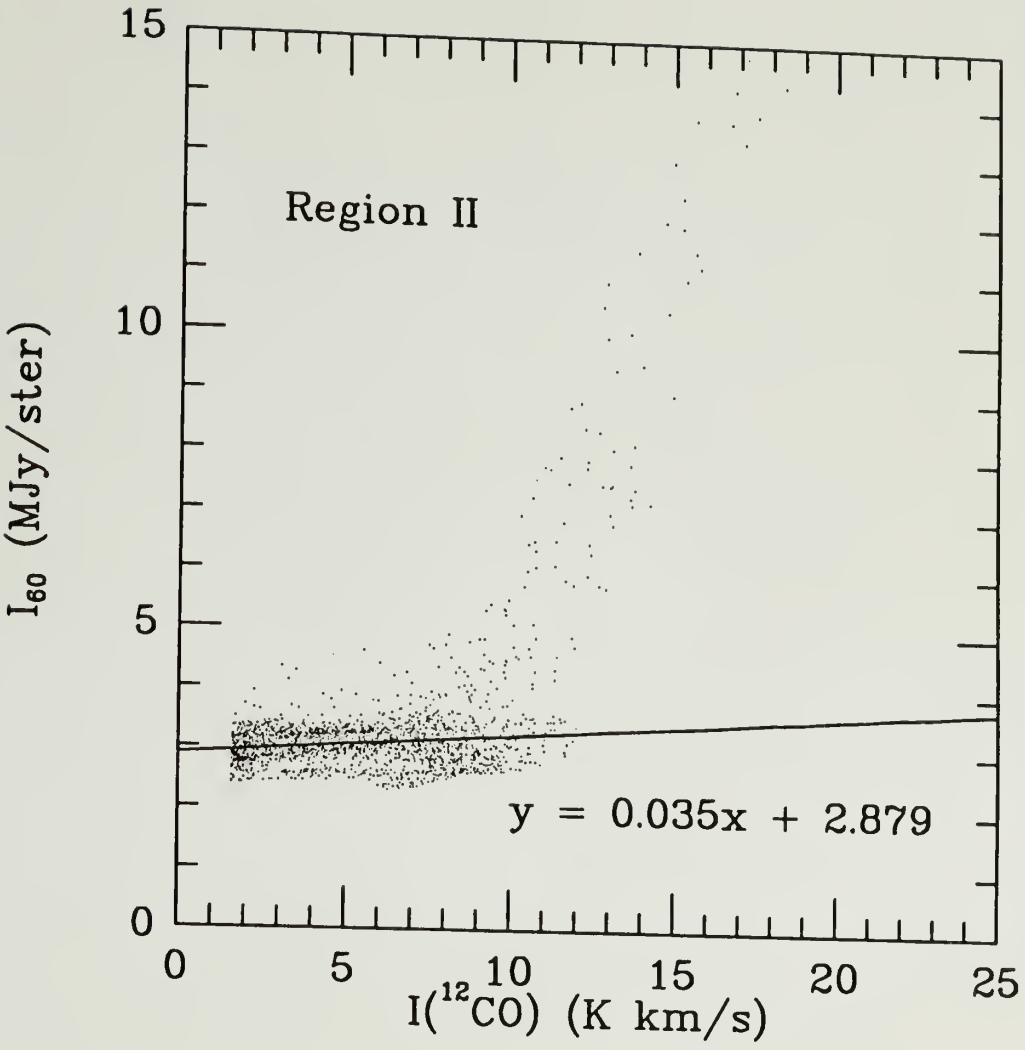

Figure 5.7 The 60 μm Intensity as a function of $I_{^{12}CO}$ for Region II. Points with $I_{^{12}CO}$ greater than 7 K km s^{-1} were fitted by least squares and the fitted line is shown. The points that substantially lie above the fitted line are due to the IRAS point source 06453-0209.

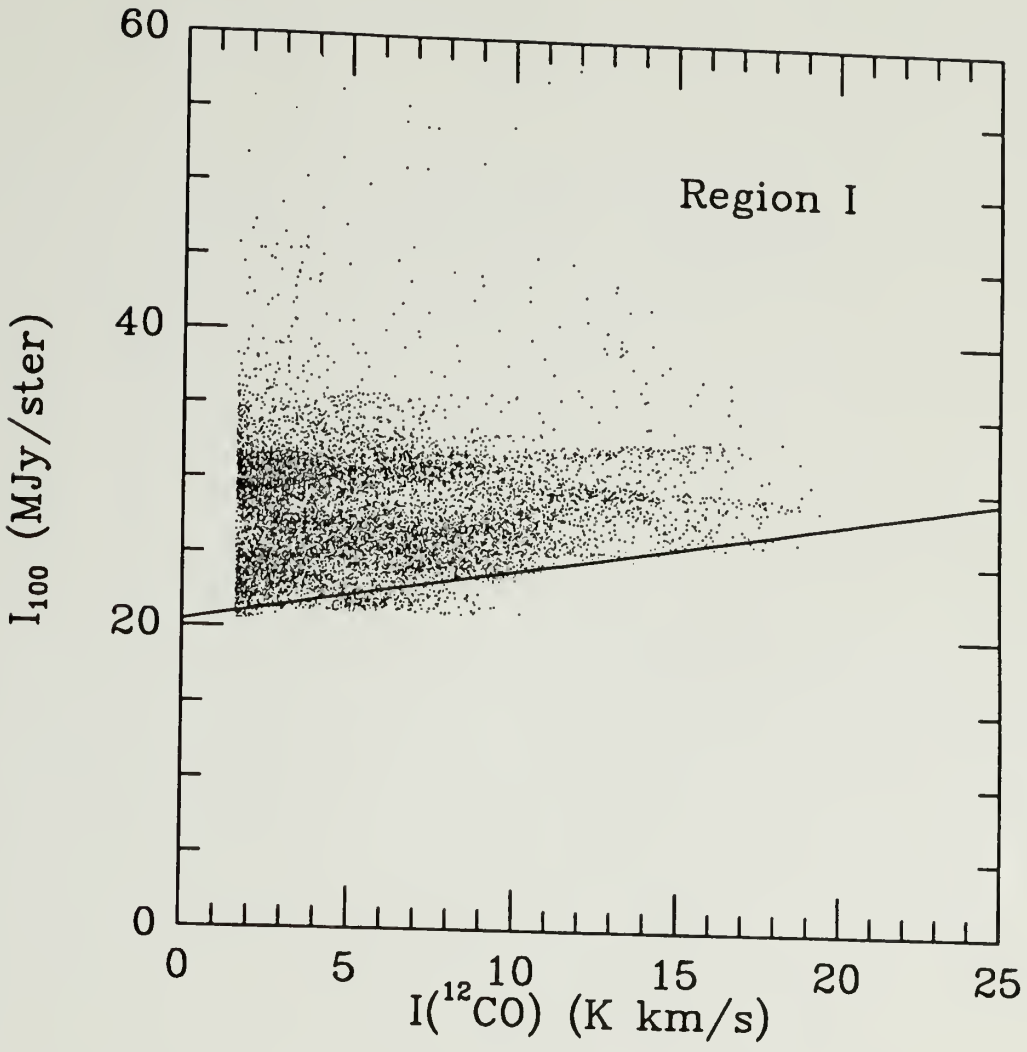

Figure 5.8 The 100 μm intensity as a function of $I_{^{12}CO}$ of the Region I. Solid line represents the least-squares fitted line for Region IV.

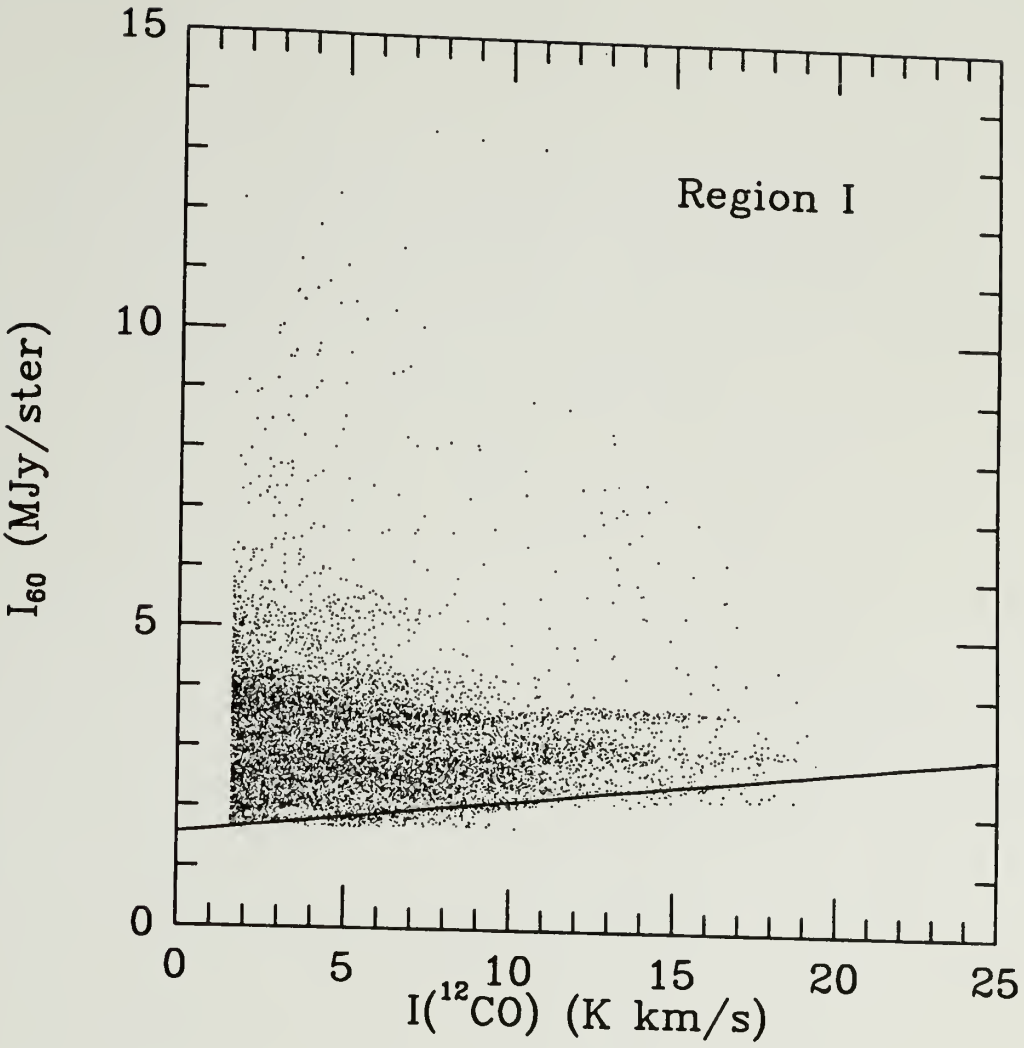

Figure 5.9 The 60 μm intensity as a function of $I_{^{12}CO}$ of the Region I. Solid line represents the least-squares fitted line for Region IV.

CHAPTER 6

NEAR-INFRARED DATA ANALYSIS

6.1 Introduction

In Chapter 5 we identified a number of IRAS point sources that could be relatively low-luminosity young stars formed within G216-2.5. To further study these FIR sources, near-infrared images at J, H, and K bands have been obtained for the first nine sources in Table 5.1. If these FIR sources are indeed young stellar objects in G216-2.5, we should be able to detect their near-infrared emission. Based on the near-infrared colors of these sources, their nature and evolutionary status can be addressed (Lada and Adams 1992).

6.2 Images

The near-infrared images, presented in Figure 6.1(a–i), were first flat fielded and then background subtracted. In Figure 6.1(a and b) the data obtained at San Pedro Martir are displayed. Mosaicked images were obtained only at K band and single frames centered on the IRAS sources were obtained at J and H bands. The data obtained at Kitt Peak are displayed in Figure 6.1(c–i), and those data represent nine frames mosaicked into large images at J, H, and K. The size of the

mosaicked frames is roughly $3' \times 3'$ for the Kitt Peak data, and $2'.2 \times 2'.2$ for the San Pedro Martir data. All images are presented in ADUs (analog-digital-units), not on a magnitude scale; thus, the stars appear brighter in the J band images than in the K band images, although this is not really the case.

The images obtained for both 06416-0352 and 06471-0325 at Kitt Peak were of poorer quality than the other images, thus, larger photometric errors may result. The background in some of the mosaicked frames were not well matched and offsets are apparent in some of the images.

The near-infrared counter parts of the IRAS point sources, if they are young stellar objects are expected to be relatively red (Adams and Lada 1992). In fact, extremely red objects have been detected toward 6 of the 9 IRAS point sources. In many cases the objects were so red, they were only detected at H and K bands. The results of the photometry of these fields are presented in the next section and a summary of each region is presented in section 6.4.

6.3 Color–Color and Color–Magnitude Diagrams

Photometry at J, H, and K was performed on the nine regions observed. One hundred and fifty individual near-infrared sources were identified in the 9 fields and their magnitudes were determined. Color–color diagrams for these objects are presented in the left-hand panels and color-magnitude diagrams are presented in the right-hand panels of Figure 6.2. Colors and magnitudes are presented for stars brighter than $m_K \sim 14^m.5$, $m_H \sim 15^m.5$ and $m_J \sim 15^m.5$. In both the color-color

and color-magnitude diagrams the solid line shows the location of unreddened main sequence and giant stars, and in the color-color diagram the dashed lines represent the reddening vector using the reddening law of Koorneef (1983) and enclose the region where reddened stars should be. As can be seen in the color-color diagrams, most of the stars are consistent with being unreddened main sequence and giant stars. The location of young stellar objects, such as T Tauri stars, Ae/Be stars and embedded core sources, in the near-infrared color-color diagram is reviewed by Lada and Adams (1992). These objects are often surrounded by disks that reprocess photospheric emission and also produce accretion luminosity. Both of these processes enhance the objects K-band flux, thus these young stellar objects often appear in the color-color diagram displaced to the right of the region occupied by reddened main sequence and giant stars. However, not all young stellar objects can be clearly distinguished from reddened stars in the near-infrared color-color diagram. Thus, there is some ambiguity in the color-color diagram, and objects which appear to be reddened stars may in fact be T Tauri stars or Ae/Be stars. Without additional information, it is impossible to identify all the young stellar objects in these fields.

6.4 Description of Individual Sources

In this section we describe the near-infrared data on the individual sources in more detail and attempt to identify the near-infrared counterparts of the IRAS sources.

06453-0209

This IRAS source is located in the middle of the satellite cloud (Region II). The infrared images shown in Figure 6.1(a), reveal 5 extremely red stars that lie near the center of the K-band image. Only star was detected at all three near-infrared bands and two stars were detected at H, and K bands. Two other stars were detected only in K band. The star detected in all three bands lies well outside the location of reddened and unreddened stars in the color-color diagram, while the other two stars have only red colors in H–K. However, the striking concentration of stars toward the position of the IRAS source and their extremely red colors suggest that these stars are physically related and are probably young, low luminosity stars (the total FIR luminosity from this region is only 189 solar luminosities) that have recently formed in the satellite cloud. In addition, Fukui *et al.* (1990) have claimed to detect a bipolar molecular outflow from this IRAS source, further strengthening our interpretation that these are young stars. In fact, if the large H–K colors observed for these stars is due to interstellar extinction, then the visual extinction would have to be 10 to 20 magnitudes, much larger than the extinction implied by the CO observations (see Table 6.4). This suggests that the H–K color may arise in a circumstellar disk or shell.

Figure 6.4 shows a grid of 81 ^{12}CO and ^{13}CO spectra centered on 06454-0209, the spectra cover $7'.5 \times 7'5$ region and spaced by $50''$. Relatively strong and broad emission is seen; these spectra do not have sufficient sensitivity to detect the molecular outflow. Figure 6.5 shows the CO, CS, and HCO^+ spectra obtained toward this IRAS source. The detection of CS and HCO^+ demonstrates that the young

stars are associated with a dense core of molecular gas. The size of the core is approximately 0.5 pc. Assuming that the CS emission is optically thin, has an excitation temperature of 10 K, and the CS abundance is 1×10^{-8} (Irvine, Goldsmith, and Hjalmarson 1987), the mass of the core is approximately 23 $M_{\odot}$.

06522-0350

This IRAS source is located in the very small cloud located directly above the main body of the cloud (Region III). The strongest ^{12}CO emission in G216-2.5 is found in this direction ($T_{\rm R}^{*}$ = 8.4 K). This IRAS source has the largest FIR luminosity (300 solar luminosities) of the 9 sources. The K band image shown in Figure 6.1(b) reveals 7 very red stars located in a small cluster at the center of the image. These stars were not detected in the J band image and were only faintly detected at H band; thus, none of these sources appear in the color-color diagram shown in Figure 6.2(b). With only the H-K color, it is not possible to unambiguously identify the nature of these stars, although this striking group is very likely a cluster of newly formed stars, and is responsible for the observed FIR emission. As in 06453-0209, the visual extinction inferred from the CO observations is insufficient to explain the very red colors of these objects if they are entirely due to interstellar extinction.

Figure 6.6 shows a grid of 81 ^{12}CO and ^{13}CO spectra centered on 06522-0350. The spectra cover $7'.5 \times 7'5$ region and spaced by $50''$. Relatively strong and broad emission is seen toward this source, and the map clearly shows the small, elongated structure of small cloud. CS and HCO^{+} emission have been detected and spectra

of these species are shown in Figure 6.7. The core has a size of approximately 0.3 pc and, making the same assumptions as for 06453-0209, the core mass is estimated to be 10 $M_{\odot}$.

06471-0329

This source is located at the CO boundary of the main body of G216-2.5, in the direction of only relatively weak CO emission. The near-infrared images shown in Figure 6.1(c) reveal two bright stars at the center of the K-band image. These are detected at all three IRAS bands. Most of stars in this field have colors, see Figure 6.2(c), that are consistent with relatively small amounts of visual extinction. However, one of the bright stars at the center is extremely red and lies well off the location of reddened stars in the color-color diagram. This object has colors similar to the embedded core sources discussed in Lada and Adams (1992). This near-infrared object may be the source of the FIR emission seen by IRAS. The FIR luminosity for this star, if at the distance of G216-2.5, is 129 $L_{\odot}$.

06481-0517

IRAS source 06481-0517 is located near the lower boundary of the main cloud. This source has the largest S_{25} to S_{12} μm flux density ratio. Again, like 06471-0329, only weak CO emission is seen in this direction. The near-infrared images shown in Figure 6.1(d) reveal one relatively red source at the center of the images. The color-color and color-magnitude diagrams, shown in Figure 6.2(d), indicate that this source has a large near-infrared excess, similar to the star in 06471-0329.

This near-infrared source is very likely the origin of the FIR emission. The FIR luminosity of this source is 167 $L_{\odot}$.

06416-0352

This IRAS source is located at the left-most side of G216-2.5. The near-infrared images are shown in Figure 6.1(e) and the color-color and color-magnitude diagrams are presented in Figure 6.2(e), The H-band frame is not of very high quality and thus, the J-H and H-K colors derived are suspect. Nevertheless, there do not appear to be any stars that can be identified as the infrared counterpart of the IRAS source.

06428-0257

The IRAS images are shown in Figure 6.1(f) and the color-color and color-magnitude diagrams are shown in Figure 6.2(f). As in 06416-0352, most of the stars are consistent with moderately reddened main sequence and giant stars, and there is no obvious near-infrared counterpart to the FIR source.

06471-0353

This IRAS source is located in the upper part of the main body of the cloud. Molecular emission is weakly present toward this source. The infrared images are shown in Figure 6.1(g) and the color-color and color-magnitude diagrams are shown in Figure 6.2(g). The K-band images reveal two very faint sources near the center. These two sources are detected at only H and K bands and have the largest H-K color in the color-magnitude diagram. The two faint H and K band sources may be

responsible for the roughly 110 solar luminosity of FIR emission detected by IRAS. Like the earlier sources, the large H-K color is unlikely due to cloud extinction, since the estimate of the visual extinction in this direction is only 1.1 magnitudes. Thus, the large H-K color is more likely due to the presence of a circumstellar disk or shell.

06492-0349

The infrared images for this source are shown in Figure 6.1(h) and color-color and color-magnitude diagrams are shown in Figure 6.2(h). As in 06416-0352, most of the stars are consistent with moderately reddened main sequence and giant stars, and there is no obvious near-infrared counter-part to the FIR source.

06507-0519

The near-infrared images of 06507-0519, shown in Figure 6.1(i), reveal a bright star near the center of the K-band image. This star is detected at H and K bands and lies well off the location of reddened stars in the color-magnitude diagram. As in 06416-0352, most of the stars are consistent with moderately reddened main sequence and giant stars. Estimates of the unusual extinction in this diagram suggest that the large H–K color is unlikely due to reddening, thus like the sources in 0647-0353, this object may be surrounded by a circumstellar disk or shell. There is one other star in this region that appears very red star. However, the K-band image of this star is badly distorted and did not fit the point spread function, therefore, no photometry was performed.

6.5 Absolute Magnitude vs. Mass Relation

We have tentatively identified the red sources that are listed in Table 6.4 and that are discussed above as likely young stellar objects. These objects are presumably responsible for the FIR emission. To estimate the mass of those objects we have used the rough correlation between infrared brightness and mass for Ae/Be stars and T Tauri stars first pointed out by Carpenter *et al.* (1992). Due to the extinction of these regions, many more source are identified in the K-band images. However, the K band data is most effected by the presence of an accretion or reprocessing disk. In these cases, the K band measurement is a combination of photospheric emission and disk emission. Since many of the most interesting sources were only detected in K band, we have used it as indicator of the mass of the stars.

6.5.1 Absolute Magnitude, M_K

The distance modulus for a star with apparent and absolute magnitudes at K-band of m_K and M_K, respectively, can be represented by:

$$m_K - M_K = 5\log d - 5 + A_K^c + A_K^\circ, \tag{6.1}$$

where d is the distance in pc, A_K^c is the extinction of the star, caused by the surrounding cloud, and A_K° is the general interstellar extinction. From the wavelength-dependent extinction law of Koorneef (1983), the relation between A_K and A_V is $A_K = 0.09A_V$. The visual extinction can be calculated from the N(^{13}CO) - A_V

relation which was obtained by using star count technique described in Chapter 3:

$$N(^{13}CO) = 1.73 \times 10^{15}(A_V - 0.95) \tag{6.2}$$

Using the adopted distance of G216-2.5 of 2.2 kpc, the general extinction to the cloud is approximated $A_V = 2.2$ magnitude, or $A_K = 0.2$ magnitude. Therefore, the absolute K magnitude can be expressed as:

$$M_K = m_K + 5 - 5\log d - 0.09A_V - 0.2 \ = m_K - 11.91 - 0.09A_V. \tag{6.3}$$

To correct for the cloud extinction, we have assumed the stars are, on average, located midway in the cloud, so only one-half of the cloud extinction is assumed to be in the front of the stars. Even so, the extinction correction at K band is small, and the uncertainty in estimating the visual extinction is not a dominant source of error. The absolute K magnitudes for the stars of interest are listed in Table 6.4 along with estimates of the ^{13}CO column density, and visual extinction in that direction.

6.5.2 Mass Estimate

The determination of the masses of young stars is difficult. Hillenbrand *et al.* (1992) have provided a mass estimate for 30 Ae/Be stars tabulated in Table 6.1. Masses of 35 classical T Tauri stars (TTS) and 10 weak-lined T Tauri stars (WTTS) were taken from Beckwith *et al.* (1990) and the data on these stars are tabulated in Table 6.2, and Table 6.3. All absolute K magnitudes tabulated are corrected for extinction, although the K-band extinction is very small for the most of the stars. In Figure 6.3 the relationship between mass and absolute magnitude for T Tauri

Table 6.1 Parameters of Ae/Be stars.

Name	*Spec. Type*	*d* (pc)	*K*	A_V	M_* [$M_\odot$]	M_K
BD+61 154	B8	650	5.70	2.1	5.3	-3.55
AB Aur	A0	160	4.40	0.4	3.2	-1.66
UX Ori	A2	460	7.40	1.2	3.3	-1.02
HK Ori	A5	460	7.29	1.2	2.0	-1.13
HD245185	A2	400	8.26	0.1	2.3	0.24
T Ori	B9	460	6.22	1.7	3.6	-2.25
V380 Ori	B9	460	6.09	1.7	3.6	-2.38
BF Ori	F2	460	8.03	0.0	1.4	-0.28
RR Tau	A3.5	800	7.10	1.1	3.2	-2.51
HD250550	B7	700	6.63	0.5	4.8	-2.64
LkHα 208	B7	1000	8.88	1.7	4.6	-1.27
MWC 137	B0	1300	6.41	4.5	18.9	-4.56
LkHα 215	B5	800	6.90	2.1	7.0	-2.80
HD259431	B2	800	5.68	1.6	12.2	-3.98
LkHα 218	B9	1150	8.50	1.5	3.8	-1.94
NXPup	A0	450	5.99	1.5	3.0	-2.41
HD97048	B9	215	6.04	1.3	3.4	-0.74
V856 Sco	A0	160	4.38	1.0	3.9	-1.73
HD150193	A2	160	5.51	1.5	2.6	-0.65
V921 Sco	B7	160	4.51	4.3	3.4	-1.90
KK Oph	A6	160	5.64	1.6	1.7	-0.52
HD163296	A0	160	4.72	0.3	3.3	-1.33
MWC 297	O9	450	3.08	8.3	26.5	-5.93
VV Ser	B9	440	5.61	3.0	3.3	-2.88
V1686 Cyg	B5	1000	6.17	4.8	8.5	-4.26
BD+40 4124	B2	1000	5.78	3.0	12.6	-4.49
HD200775	B2	600	4.70	2.0	16.4	-4.37
LkHα 234	B3	1000	6.84	3.4	8.5	-3.47
BD+46 3471	A0	900	6.58	1.0	7.3	-3.28
MWC 1080	B0	1000	4.70	5.3	20.6	-5.78

stars and Ae/Be stars is shown. The dashed line represents the magnitude-mass relation for the main sequence stars. The pre-main sequence stars lie below the main sequence and are more luminous for a given mass (or less massive for a given luminosity), as expected. There is a surprisingly good correlationship between absolute K magnitude and mass despite the fact that the stars are in different stages of pre-main sequence evolution. As used in Chapter 3, a bisector fit was applied to these pre-main sequence objects. The best fit line is given by;

$$\log(\mathrm{M}(\mathrm{M}_\odot)) = -0.237\mathrm{M}_\mathrm{K} + 0.097. \tag{6.4}$$

The best fit line is shown as a solid line in Figure 6.3.

In estimating masses from the mass-magnitude relation, substantial errors may be introduced. The Ae/Be, TTS and WTTS calibrator masses are uncertain; for the same magnitude, the mass of a young star may vary by a factor of 3. In addition, photometric errors and errors in the visual extinction contribute to the uncertainties in the mass estimates.

The masses estimated for the possibly young stellar objects in these field are between 0.3 and 2.8 $M_\odot$ with most below 1 $M_\odot$ (Table 6.4), values similar to the masses of T Tauri stars. In 06453-0209 and 06522-0350, where the evidence for the presence of young stars is the strongest, the stars have masses between 0.3 to 1.0 $M_\odot$. If the stars are responsible for the FIR luminosity in these regions, then each star would have to have a bolometric luminosity of about 40 $L_\odot$, similar to that of the most luminous T Tauri stars.

Table 6.2 Parameters of T Tauri stars

Name	*Spec. Type*	K	A_V	$M_* [M_\odot]$	M_K
CW Tau	K3	6.86	2.16	1.40	0.65
FP Tau	M5.5	8.84	0.00	0.26	2.82
CX Tau	M2	8.83	0.55	0.46	2.76
CY Tau	M1	8.42	0.14	0.48	2.39
DD Tau	M1	7.97	1.36	0.46	1.83
BP Tau	K7	8.05	0.23	0.67	2.01
DE Tau	M1	7.71	0.81	0.44	1.62
RY Tau	K1	5.74	0.55	1.69	-0.33
T Tau	K1	5.40	1.67	1.91	-0.77
DF Tau	M0.5	6.81	0.55	0.53	0.74
DH Tau	M0	8.33	1.52	0.67	2.17
DK Tau	K7	7.03	1.40	0.65	0.88
ZZ Tau	M4	8.54	0.65	0.28	2.46
HK Tau	M0.5	8.37	3.38	0.55	2.05
XZ Tau	M3	7.17	1.71	0.29	1.00
V710 TauA	M1	8.00	1.80	0.42	1.82
UZ TauE	M1	7.02	0.61	0.44	0.94
GG Tau	K7	7.25	1.21	0.65	1.12
GH Tau	M2	7.86	0.25	0.33	1.82
GI Tau	K7	7.55	1.33	0.70	1.41
GK Tau	K7	7.32	0.78	0.67	1.23
CI Tau	K7	7.76	1.58	0.70	1.60
DM Tau	M0.5	9.45	0.55	0.62	3.38
AA Tau	K7	8.29	0.72	0.67	2.20
HO Tau	M0.5	9.52	0.73	0.64	3.43
DN Tau	M0	8.03	0.35	0.62	1.98
HP Tau	K3	7.47	3.08	1.43	1.17
DO Tau	K7	7.49	2.44	0.72	1.25
V955 Tau	K7	7.73	3.85	0.72	1.36
DP Tau	M0.5	8.36	1.22	0.60	2.23
GO Tau	M0	9.39	2.44	0.67	3.15
DQ Tau	K7	8.08	2.13	0.67	1.87
DS Tau	K3	8.16	0.93	1.29	2.06
UY Aur	K7	7.05	1.14	0.65	0.93
GM Aur	K7	8.59	0.10	0.72	2.56

Table 6.3 Parameters of weak-lines T Tauri stars.

Name	*Spec. Type*	K	A_V	M_* $[M_\odot]$	M_K
V773 Tau	K2	6.48	2.04	1.74	0.28
V410 Tau	K7	7.54	0.00	0.63	1.52
CZ Tau	M1.5	9.33	1.36	0.40	3.19
DI Tau	M0	8.40	1.08	0.60	2.28
IQ Tau	M0.5	8.00	1.16	0.54	1.88
UX TauA	K2	7.58	0.47	1.49	1.52
FX Tau	M1	8.06	1.49	0.44	1.91
V927 Tau	M5.5	8.66	0.00	0.26	2.64
VY Tau	M0	8.79	1.02	0.70	2.68
SU Aur	G2III	5.95	0.64	2.65	-0.13

6.6 Conclusion

Nine of the IRAS point sources towards G216-2.5 have been imaged in the J, H, and K near-infrared bands. Likely near-infrared counterparts to these IRAS sources have been identified for six of the sources. Four of these are the same sources which had IRAS colors similar to embedded core sources. All of the stars identified as young stellar objects likely have near-infrared excesses similar to T Tauri and Ae/Be stars. If the sources are indeed young stars associated with G216-2.5, then they have absolute K magnitudes of 10.5 to 14.2. The brightest of these near-infrared sources could be Ae/Be stars, but most have K magnitudes consistent with their being T Tauri stars. Using a mass-magnitude relation established from well studied T Tauri and Ae/Be stars, we have estimated masses of these stars to be in the range of 0.3 to 2.8 $M_\odot$. Our identification of these stars as T Tauri stars is consistent with the FIR luminosity emitted in these regions.

Table 6.4 Parameters of embedded stars.

Name	*No.*	J	H	K	A_V	M_K	$M_* [M_\odot]$
06453-0209	1	15.08	14.67	13.65	4.94	1.52	0.55
-	2	-	14.07	13.47	4.94	1.34	0.60
-	3	-	-	13.92	4.94	1.79	0.47
-	4	-	14.69	13.81	4.94	1.68	0.50
-	5	-	-	13.68	4.94	1.55	0.53
06522-0350	1	-	14.60	13.42	3.26	1.36	0.60
-	2	-	14.05	12.24	3.26	0.18	1.13
-	3	-	13.64	12.21	3.26	0.15	1.15
-	4	-	14.96	13.50	3.26	1.44	0.57
-	5	-	13.77	12.57	3.26	0.51	0.95
-	6	-	14.80	14.17	3.26	2.11	0.40
-	7	-	14.87	13.62	3.26	1.56	0.53
06471-0329	1	14.85	12.71	10.47	1.24	-1.50	2.83
06481-0517	1	14.67	13.45	11.31	1.18	-0.66	1.79
06471-0353	1	-	15.15	14.24	1.53	2.26	0.36
-	2	-	15.40	14.10	1.53	2.10	0.40
06507-0519	1	-	14.19	12.63	2.61	0.60	0.90

Figure 6.1 J, H, and K images of (a) 06453-0209 (b) 06522-0350 (c) 06471-0329 (d) 06481-0517 (e) 06416-0352 (f) 06428-0257 (g) 06471-0353 (h) 06492-0349 (i) 06507-0519.

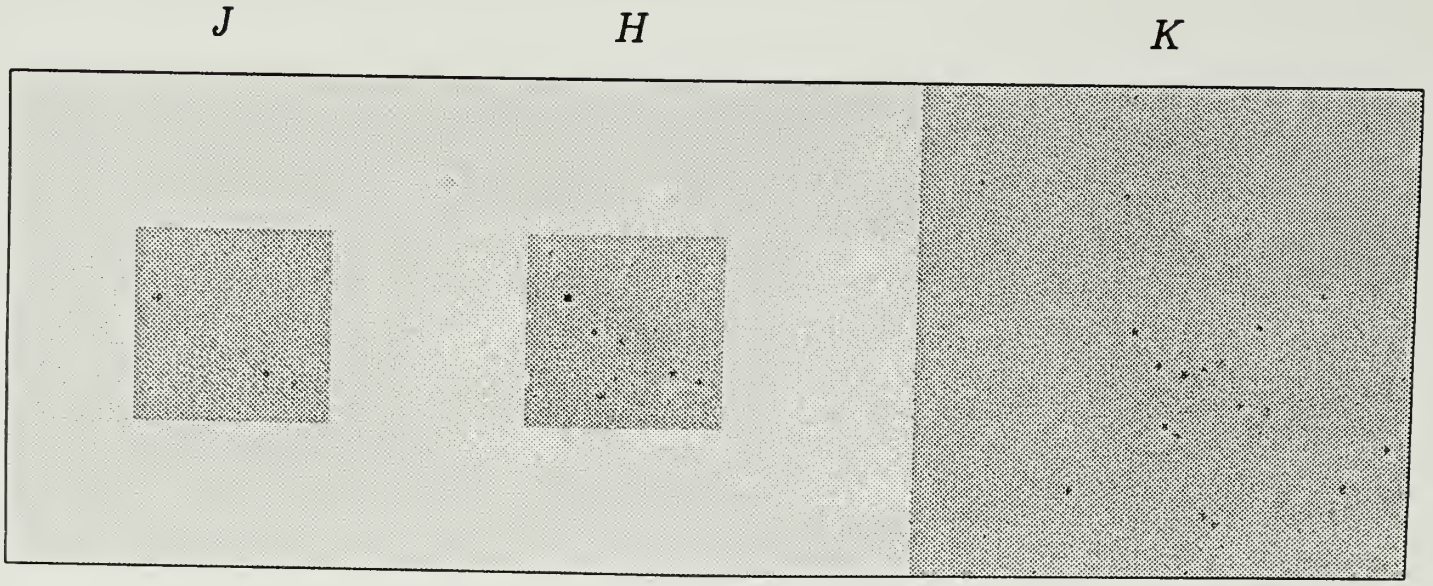

(a) 06453−0209

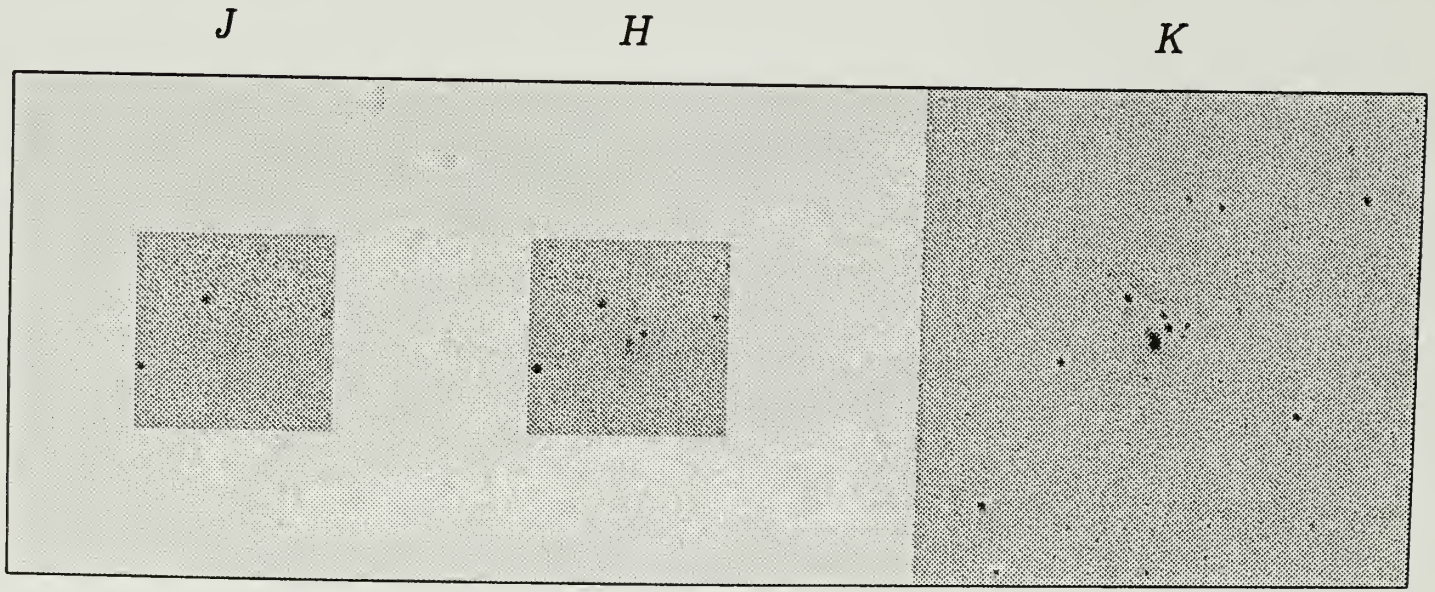

(b) 06522−0350

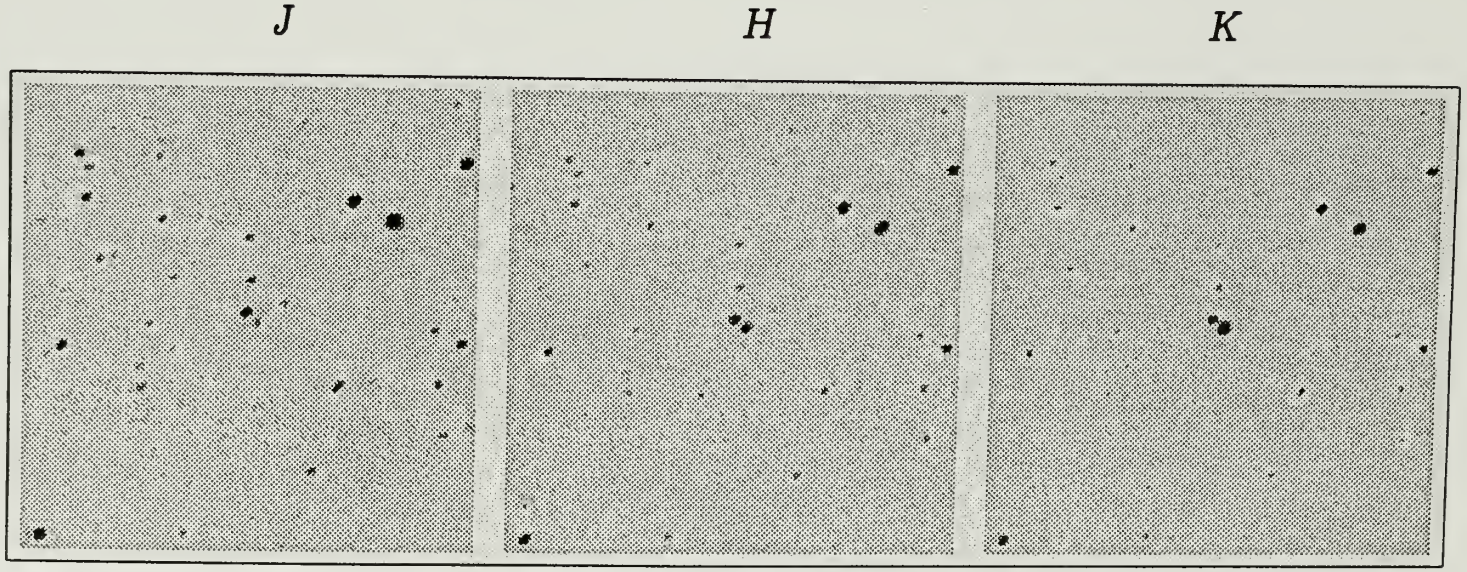

(c) 06471−0329

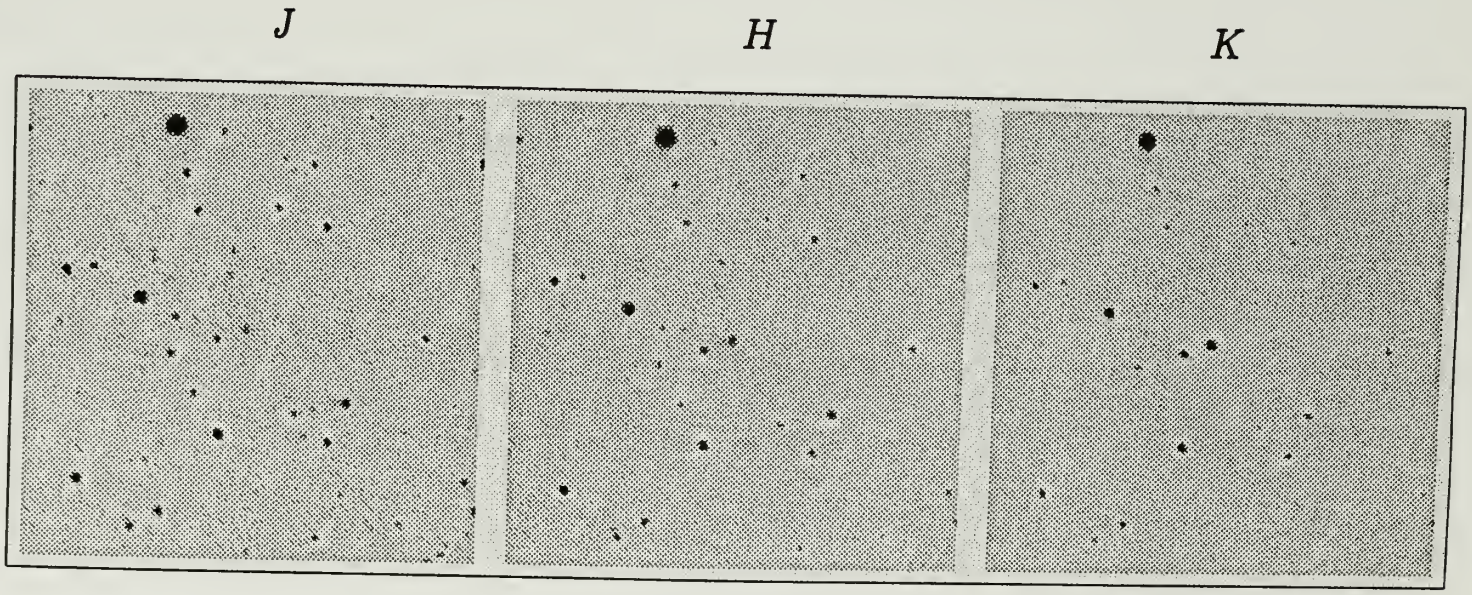

(d) 06481−0517

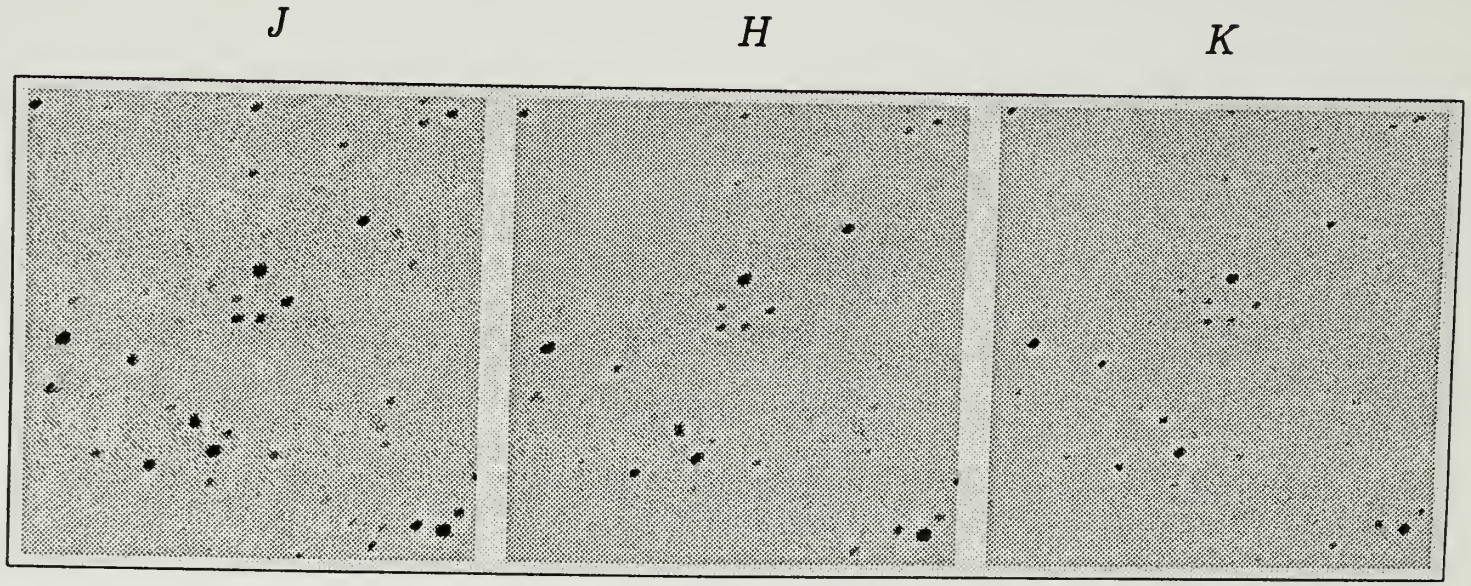

(e) 06416−0352

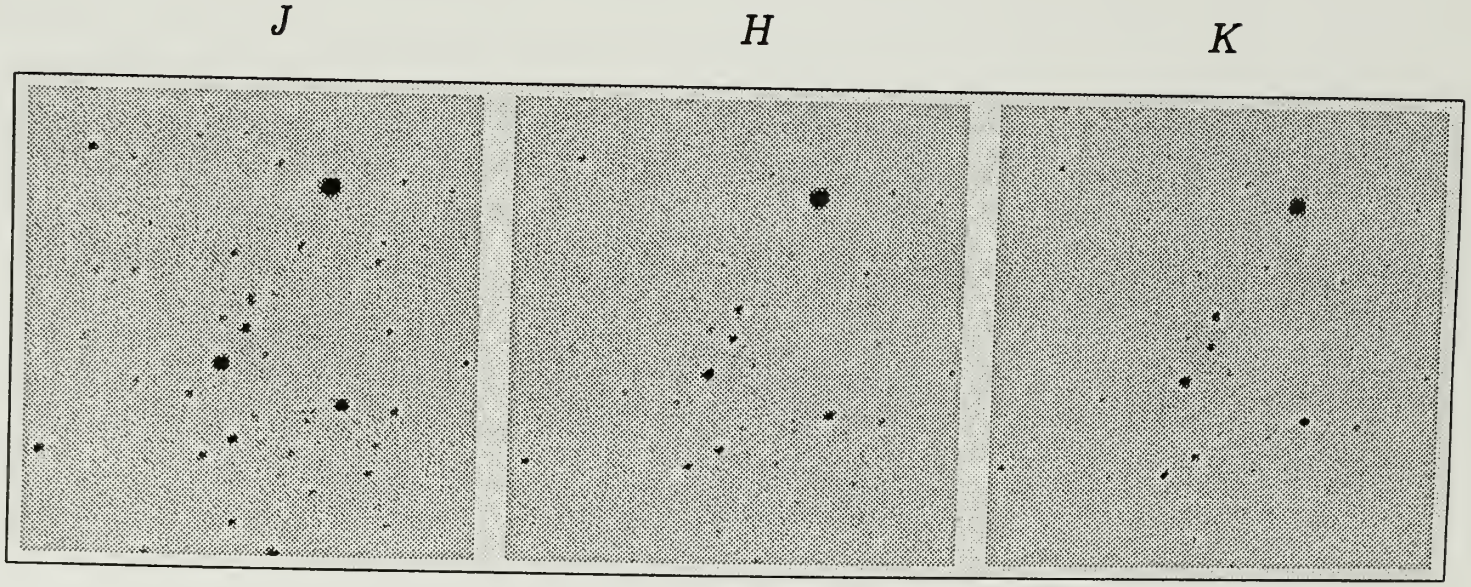

(f) 06428−0257

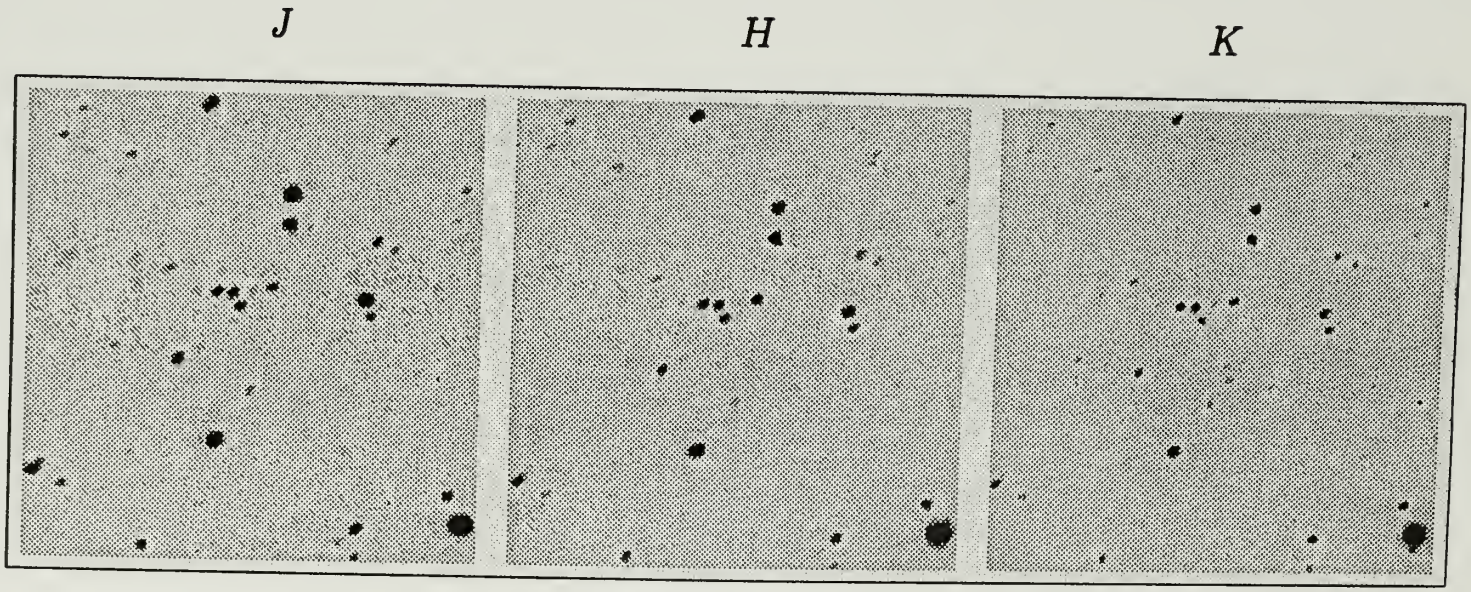

(g) 06471−0353

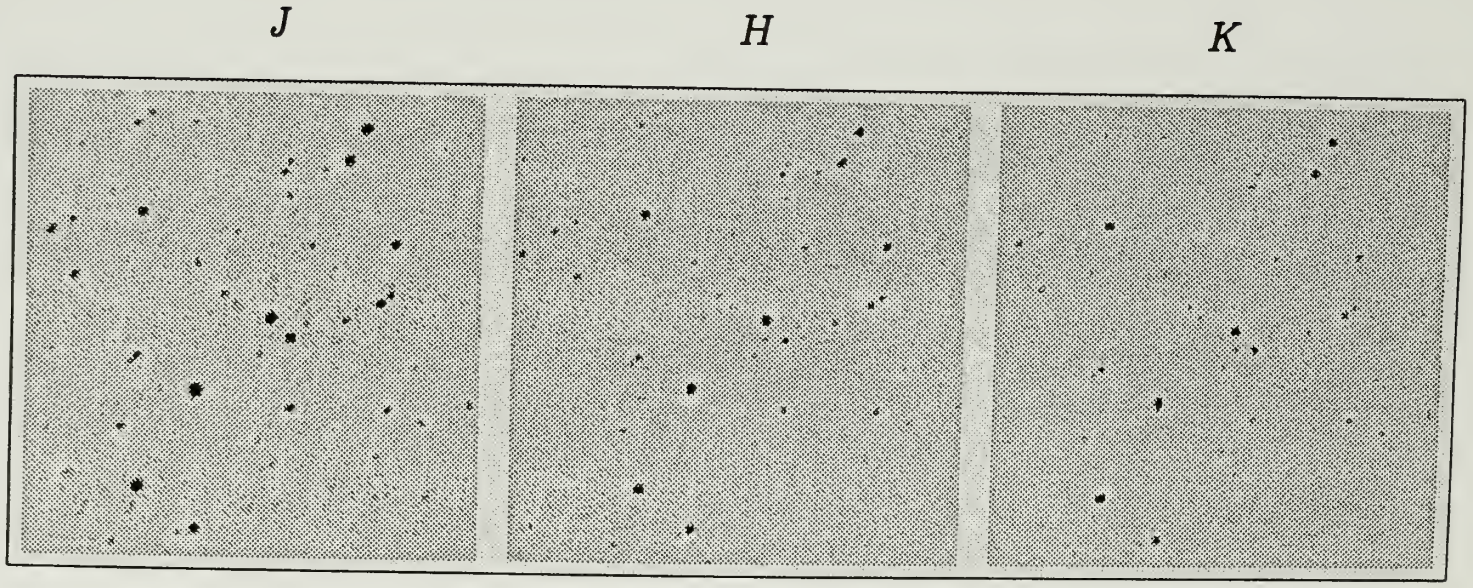

(h) 06492−0349

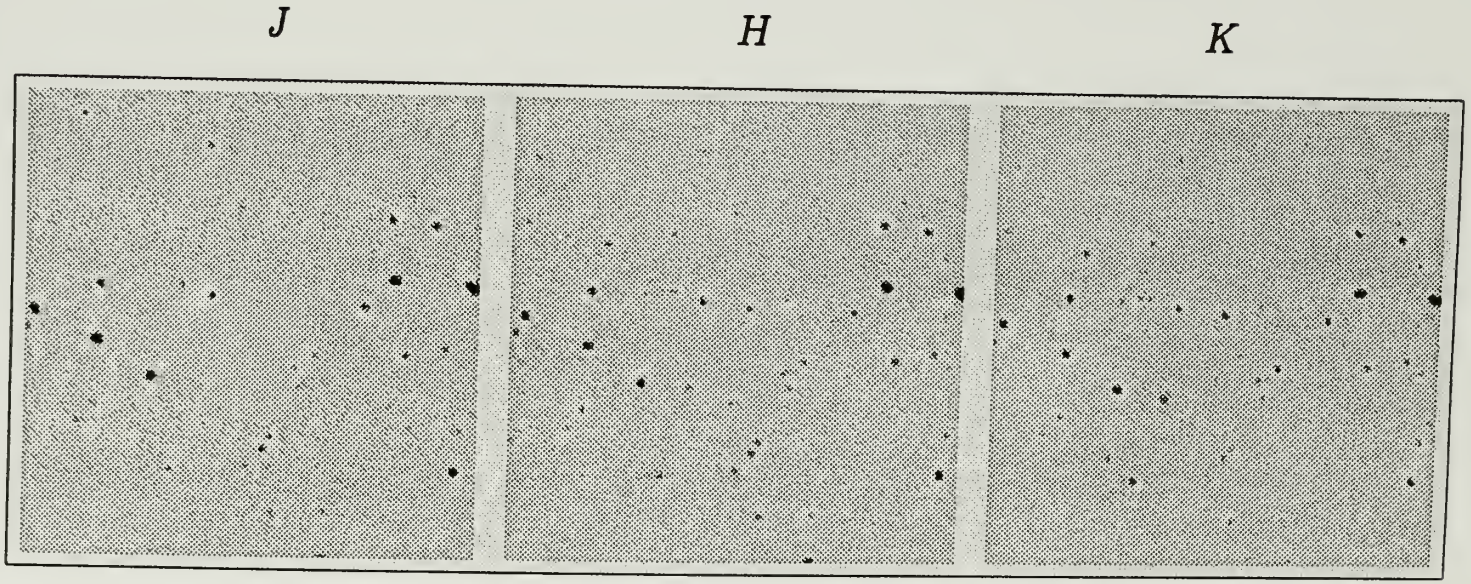

(i) 06507−0519

Figure 6.2 Color-color and color-magnitude diagrams for (a) 06453-0209 (b) 06522-0350 (c) 06471-0329 (d) 06481-0517 (e) 06416-0352 (f) 06428-0257 (g) 06471-0353 (h) 06492-0349 (i) 06507-0519. The solid line presents the main sequence and the dashed lines in the color-color diagram indicate reddening vectors of main sequence and giant stars.

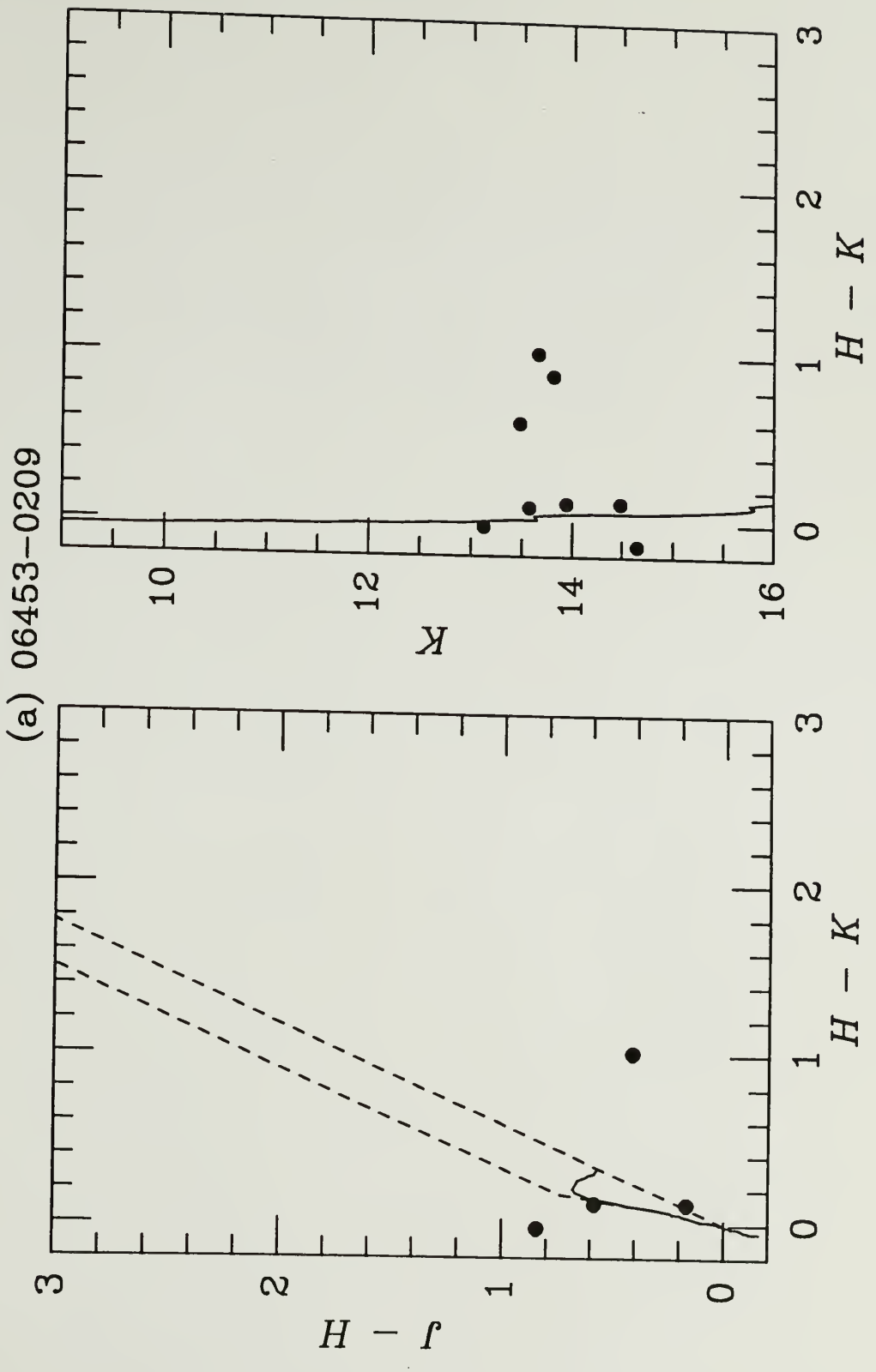
(a) 06453−0209
K
H − K
J − H
H − K

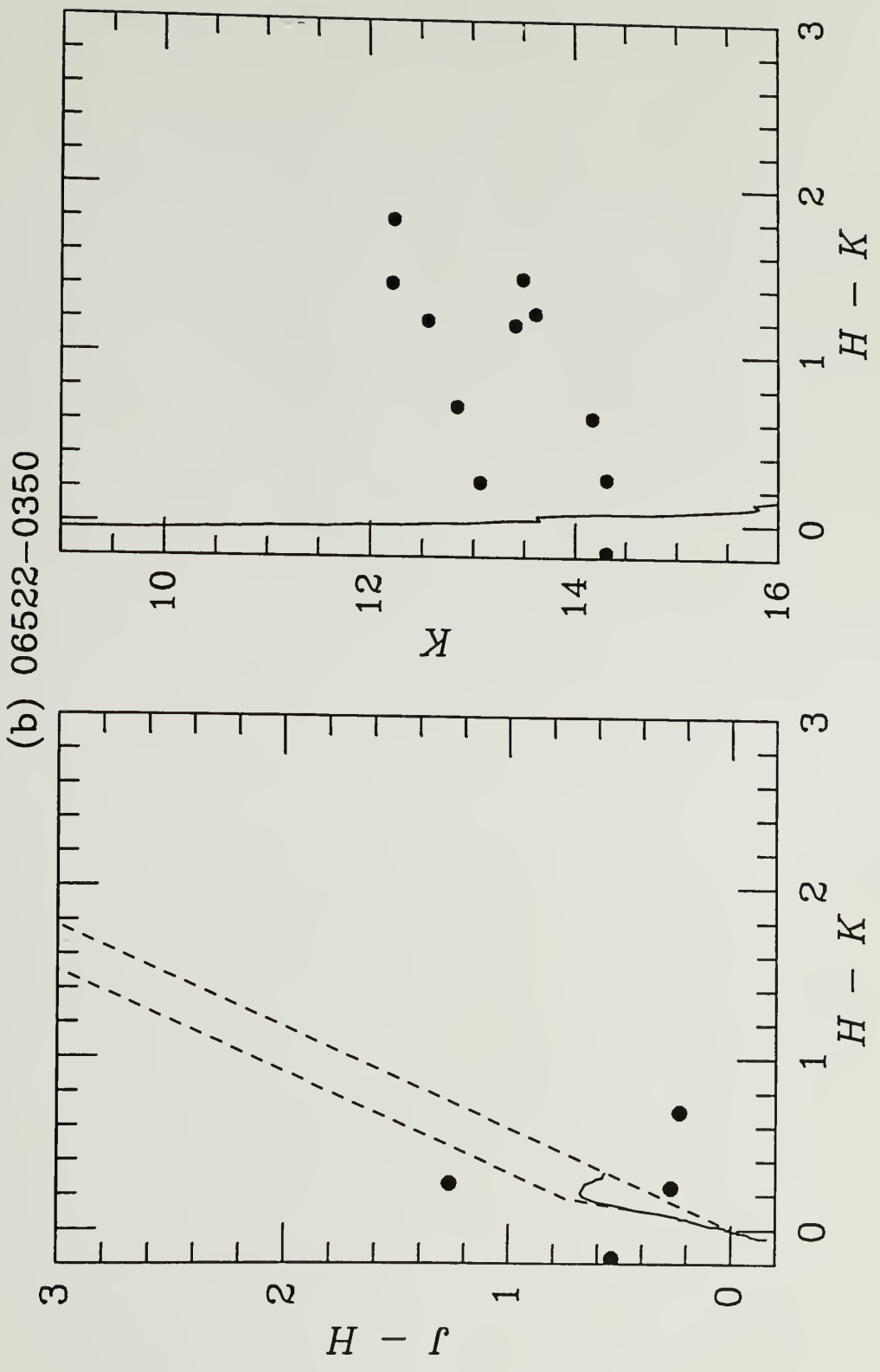
(b) 06522−0350
K
10
12
14
16
0
1
2
3
H − K
J − H
0
1
2
3
H − K

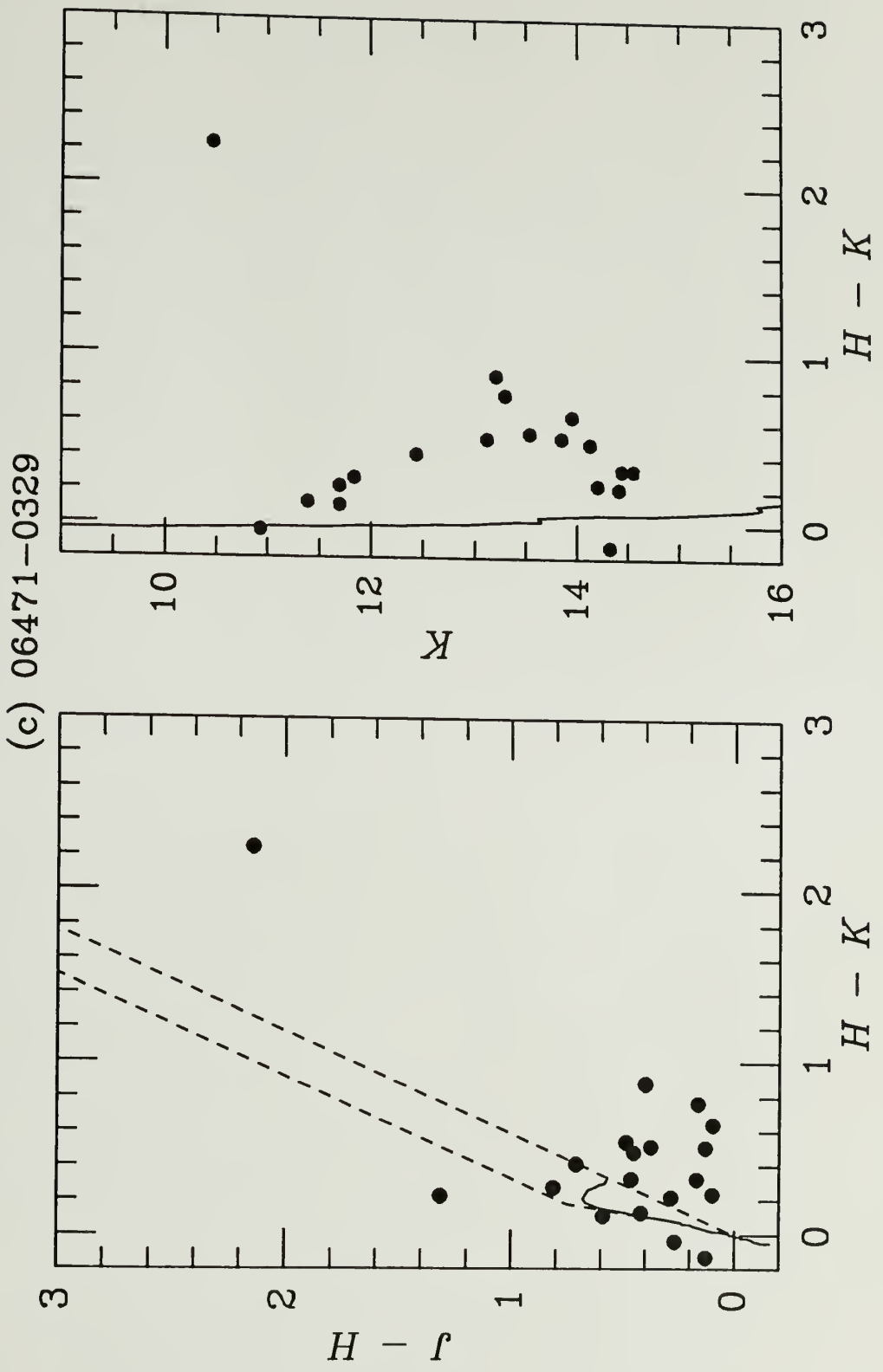
(c) 06471−0329
J − H
H − K
K
H − K

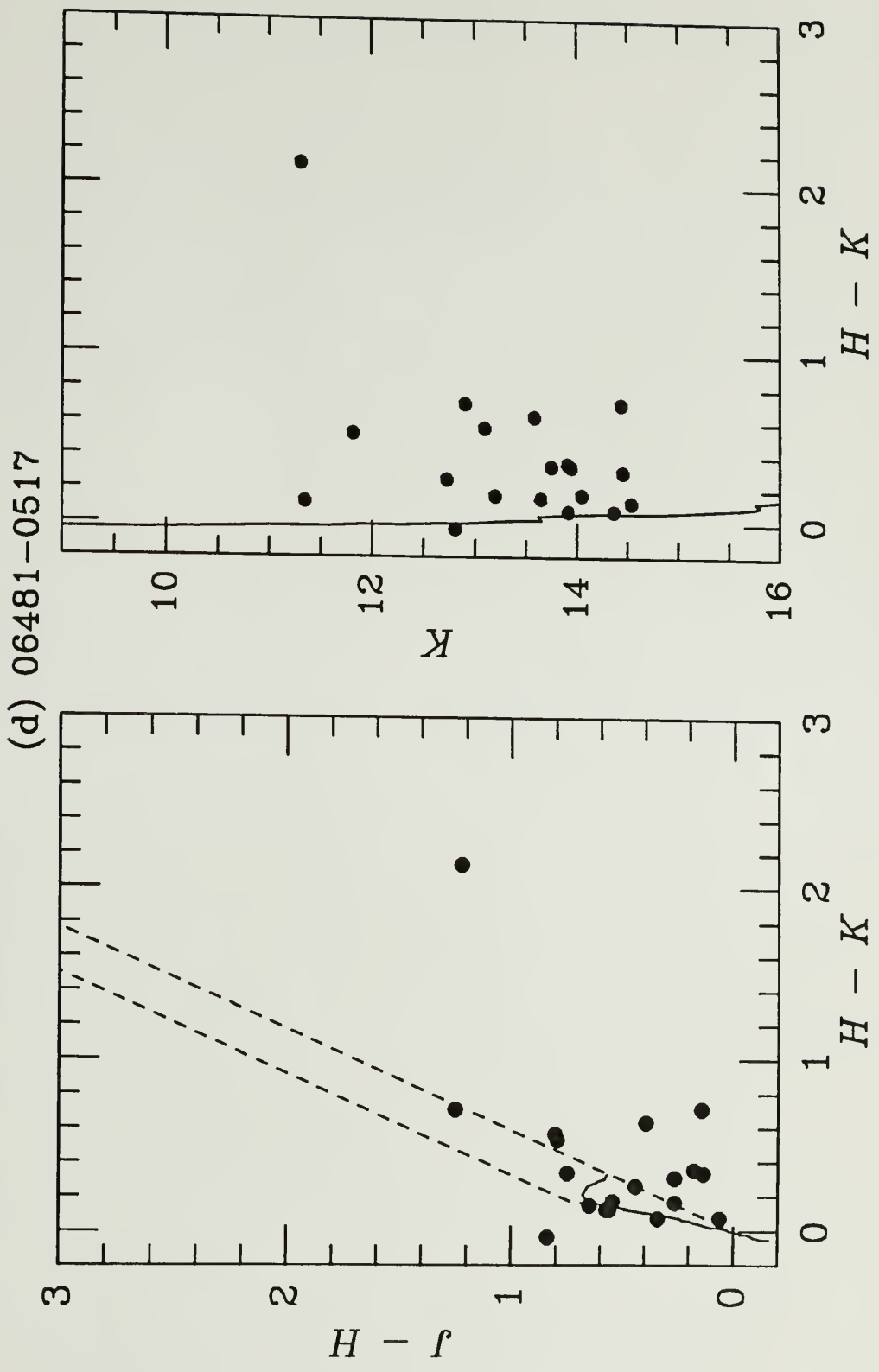
(d) 06481−0517
K
10
12
14
16
0
1
2
3
H − K
J − H
0
1
2
3
0
1
2
3
H − K

(e) 06416−0352

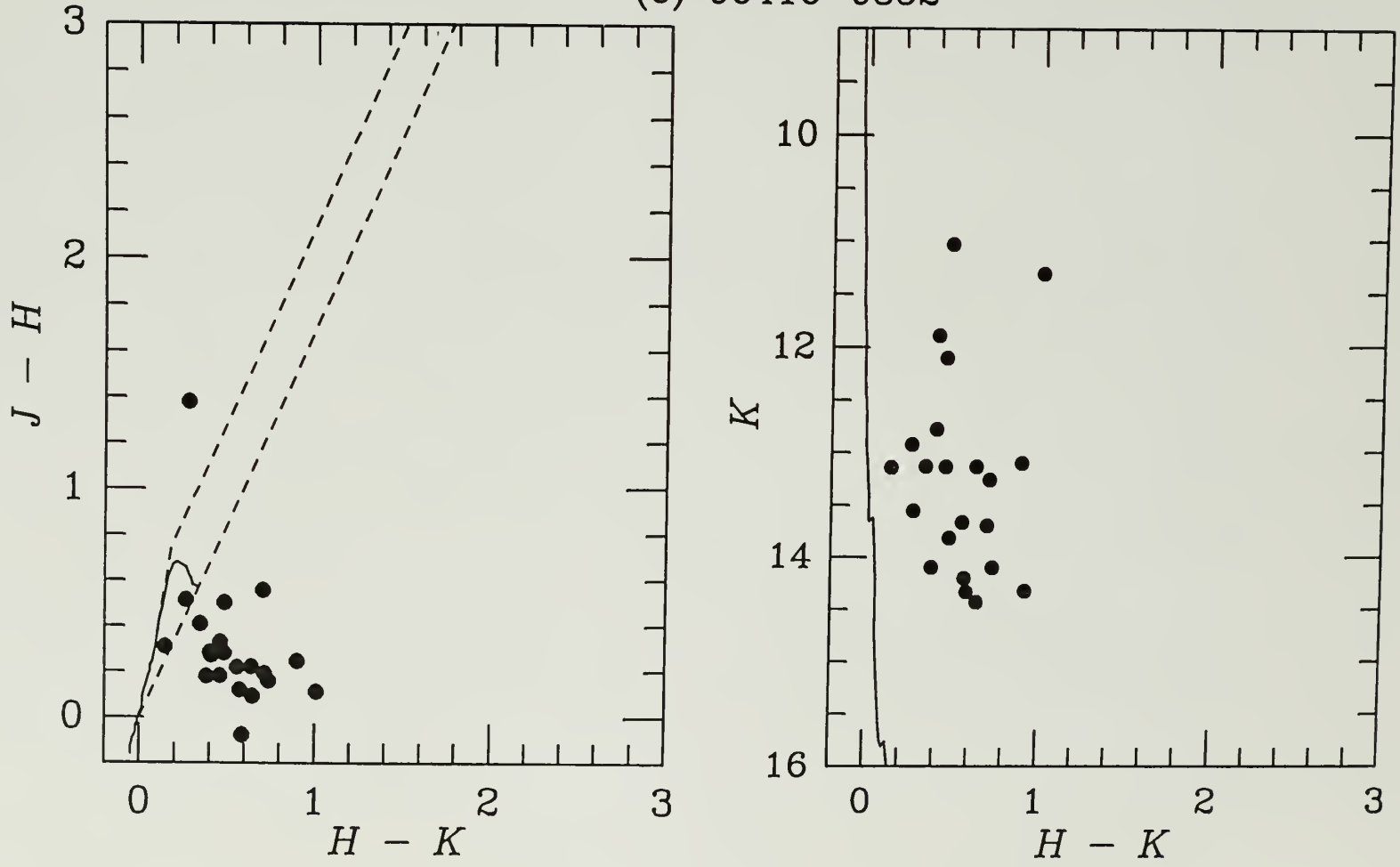

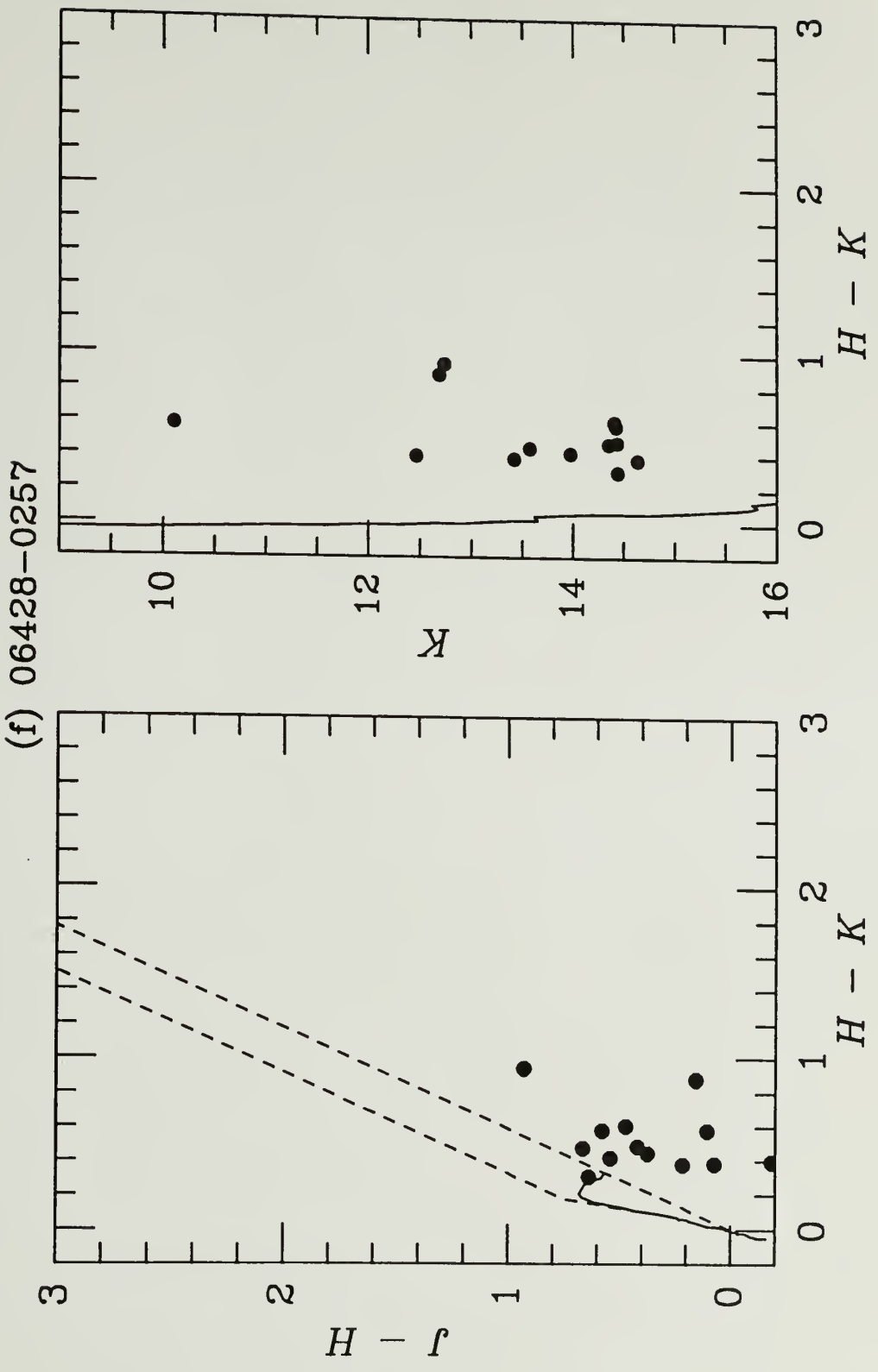
(f) 06428−0257
K
10
12
14
16
0
1
2
3
H − K
J − H
0
1
2
3
0
1
2
3
H − K

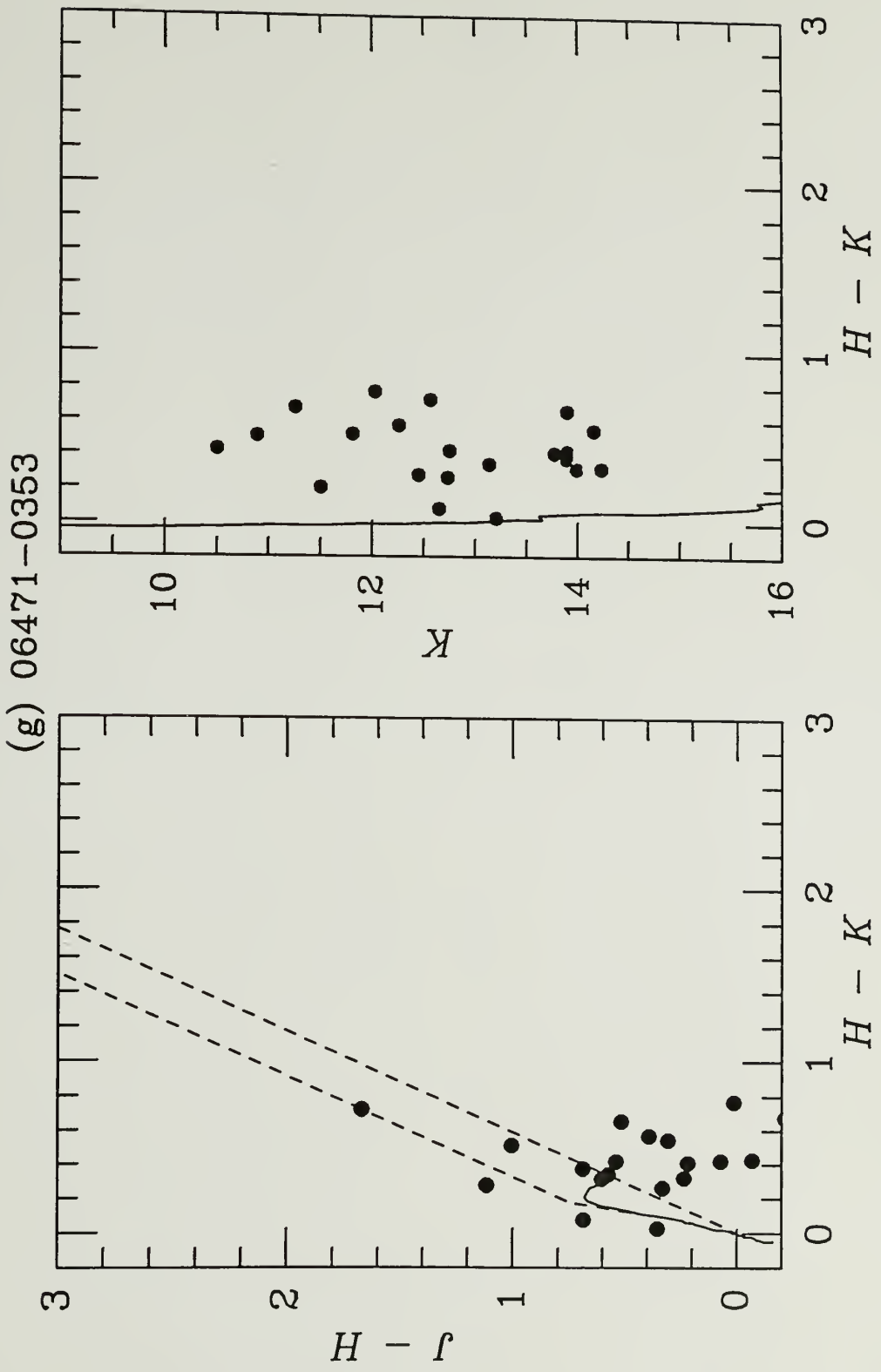
(g) 06471−0353
K
H − K
J − H
H − K

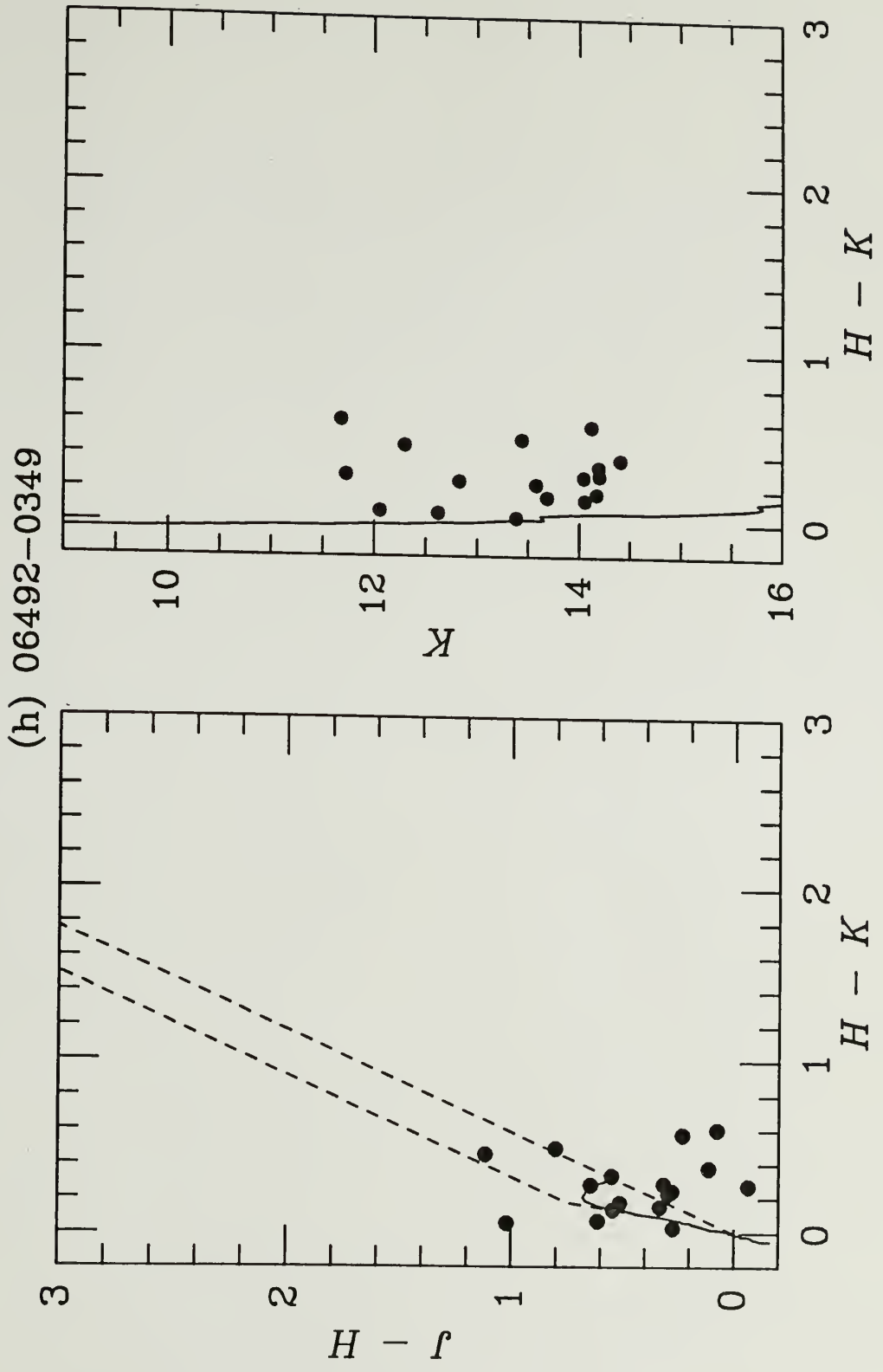
(h) 06492−0349
K
H − K
J − H
H − K

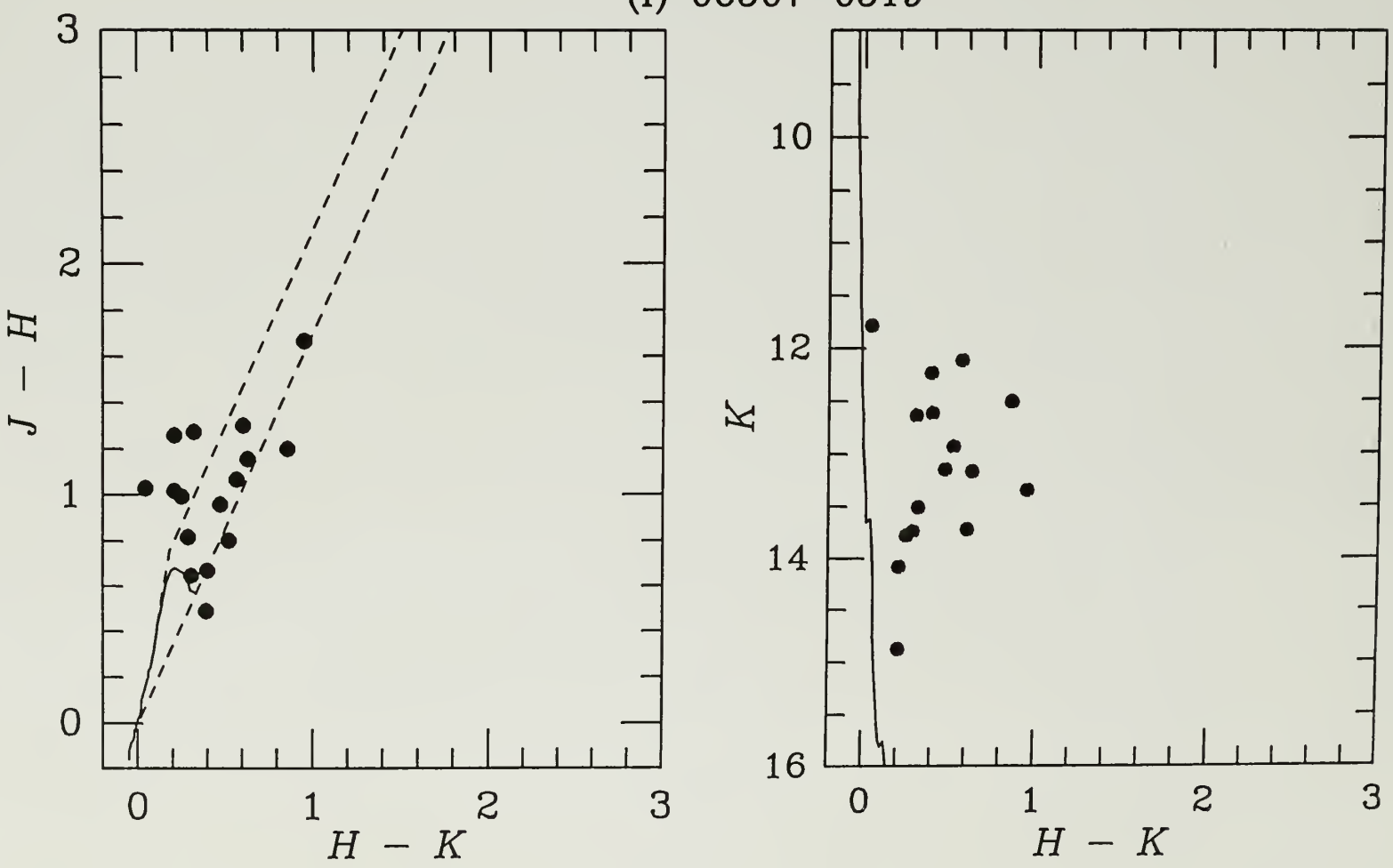
(i) 06507−0519
J − H
H − K
K
H − K

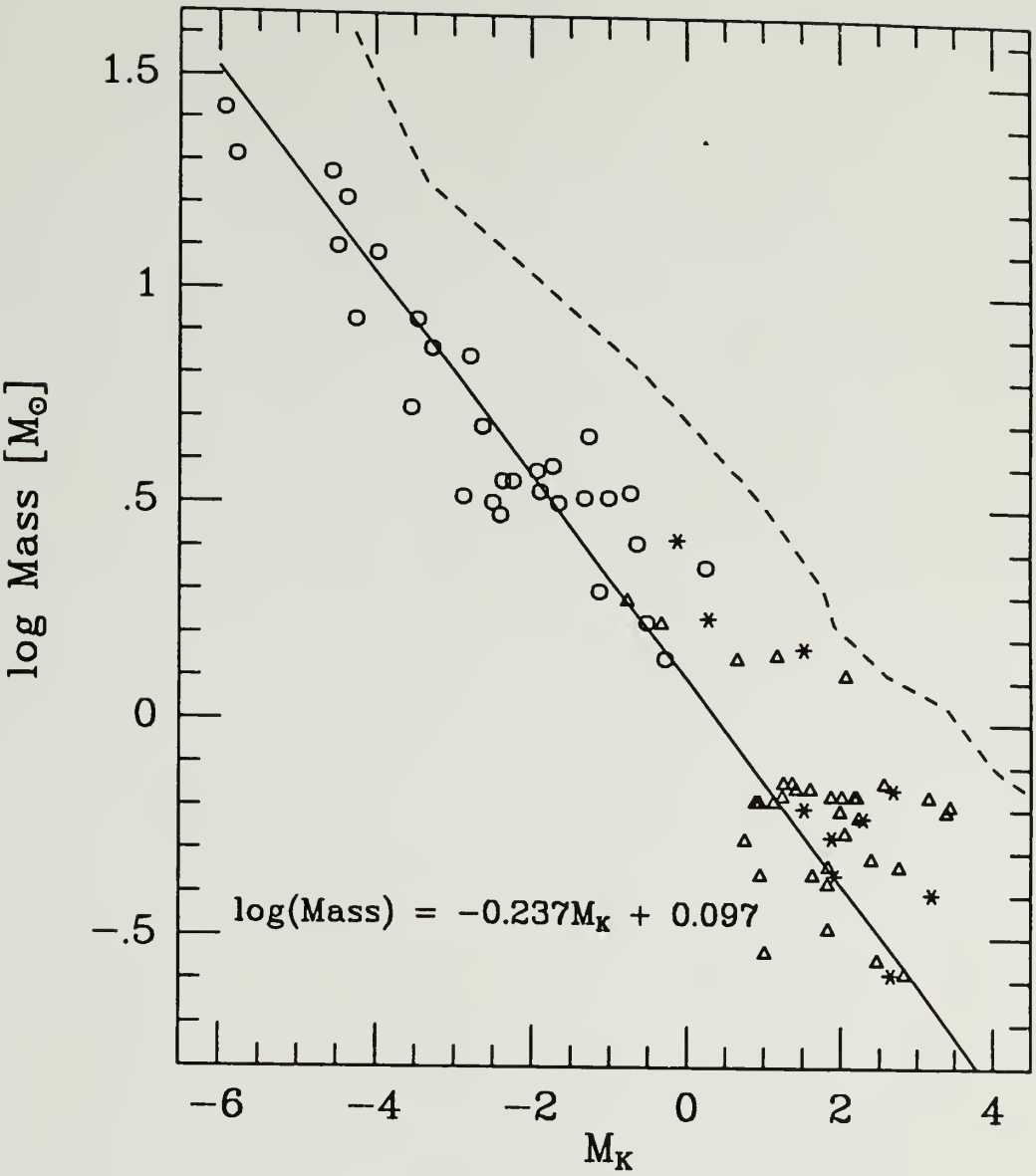

Figure 6.3 M_K versus mass relation. Open circles are the Ae/Be stars, asterisks; the WTTS, and open triangles; the TTS. The dashed line presents the main sequence.

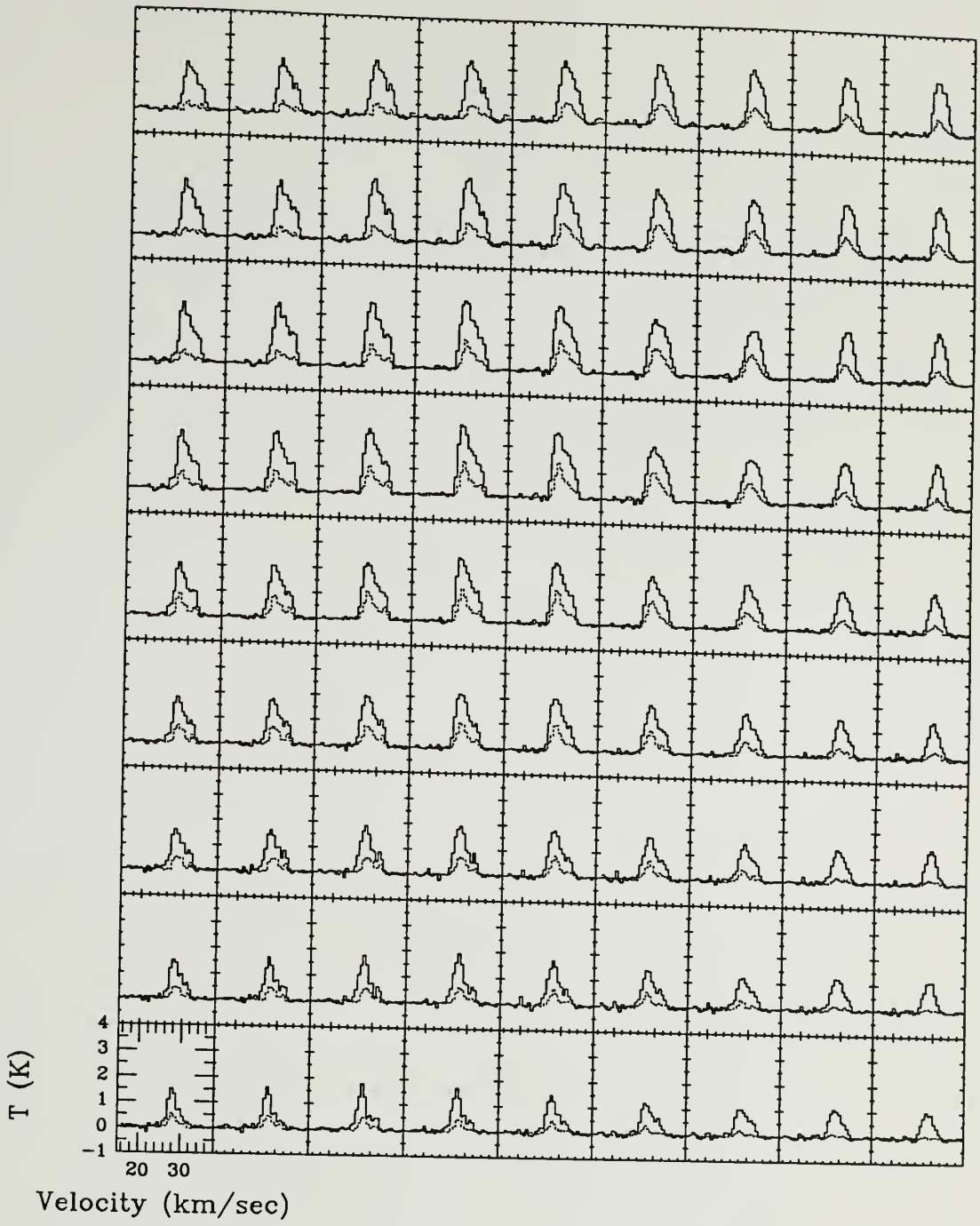

Figure 6.4 ^{12}CO and ^{13}CO spectra around the IRAS source 06453-0209.

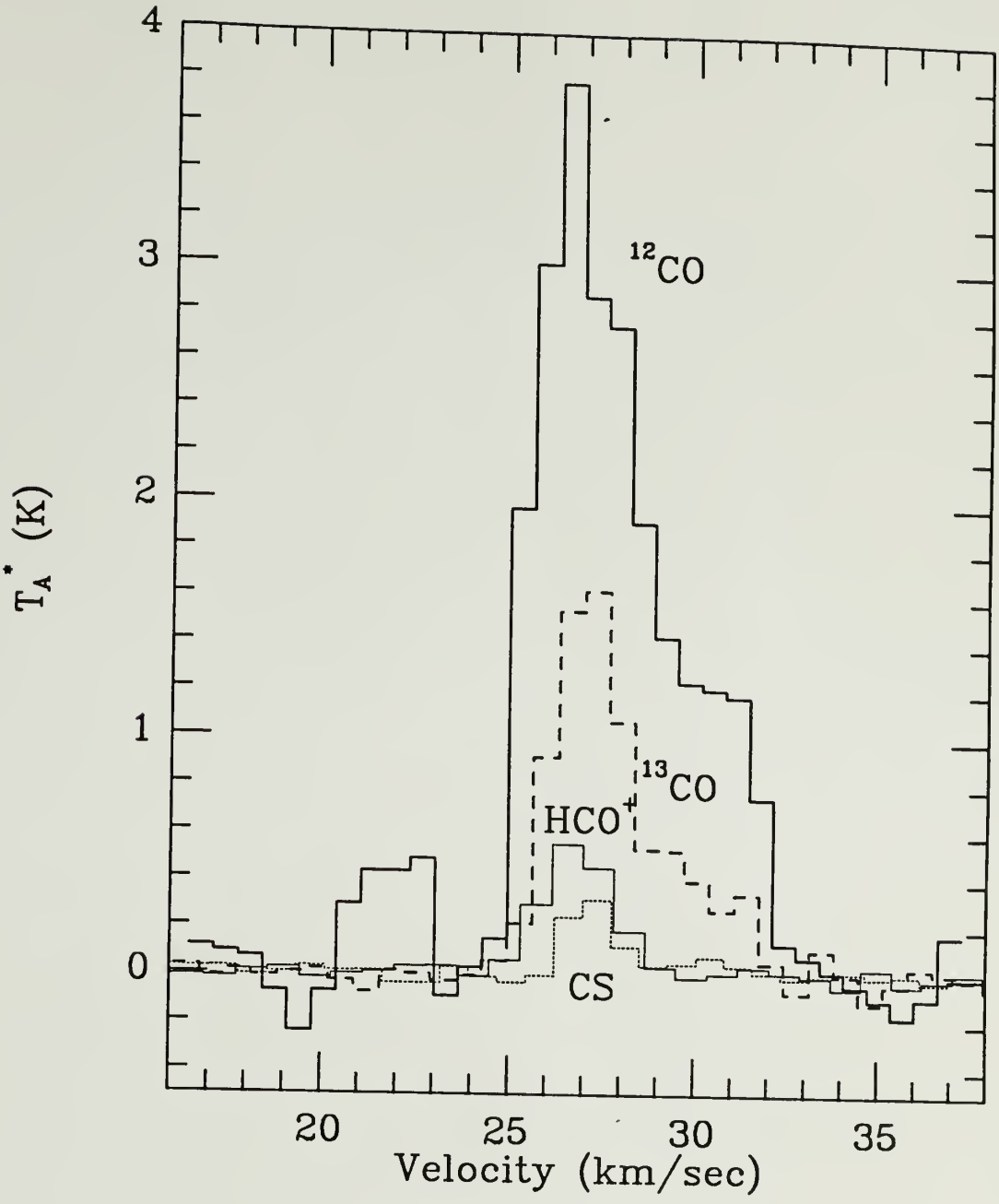

Figure 6.5 ^{12}CO, ^{13}CO, HCO$^+$, and CS spectra toward the IRAS source 06453-0209.

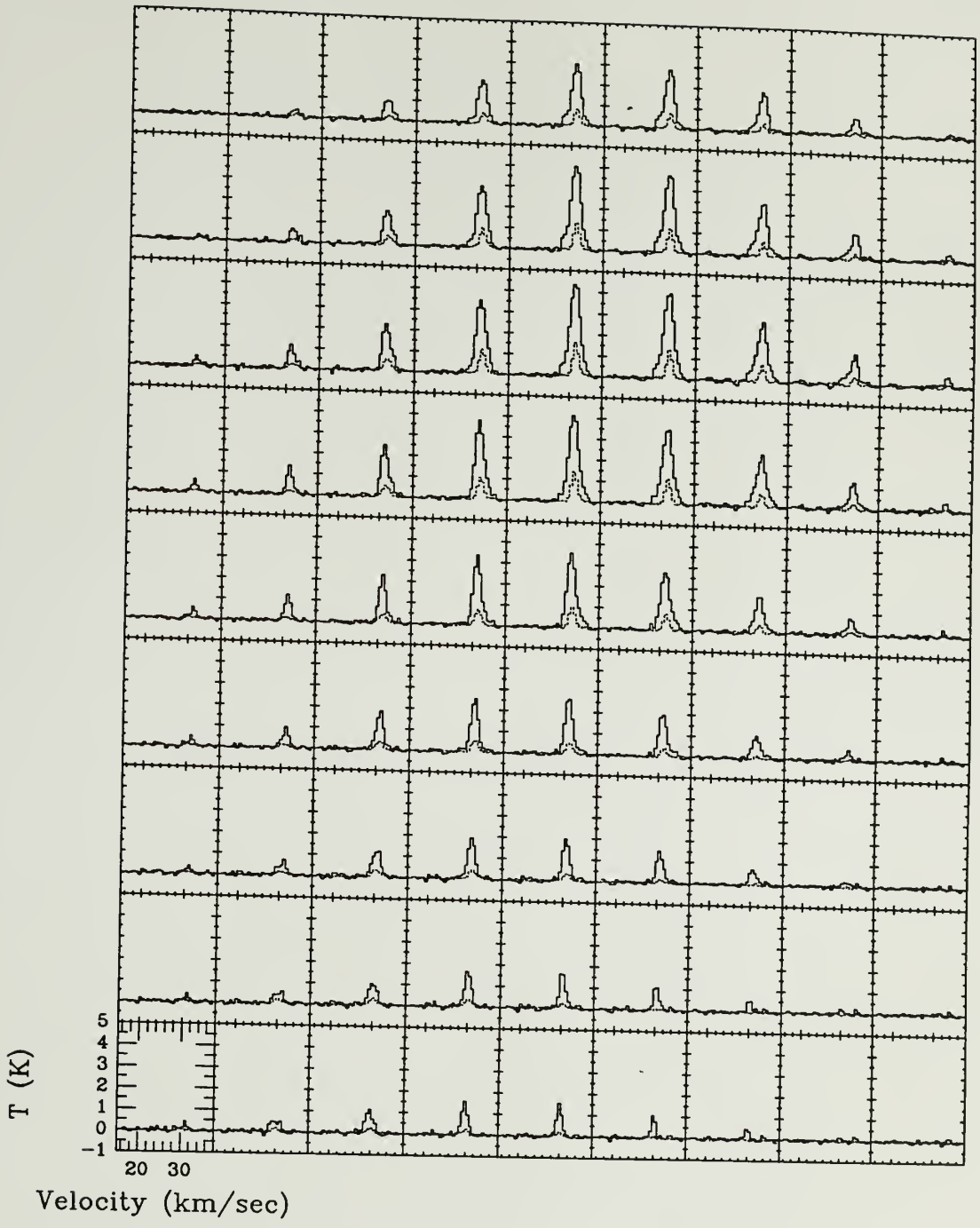

Figure 6.6 ^{12}CO and ^{13}CO spectra around the IRAS source 06522-0350.

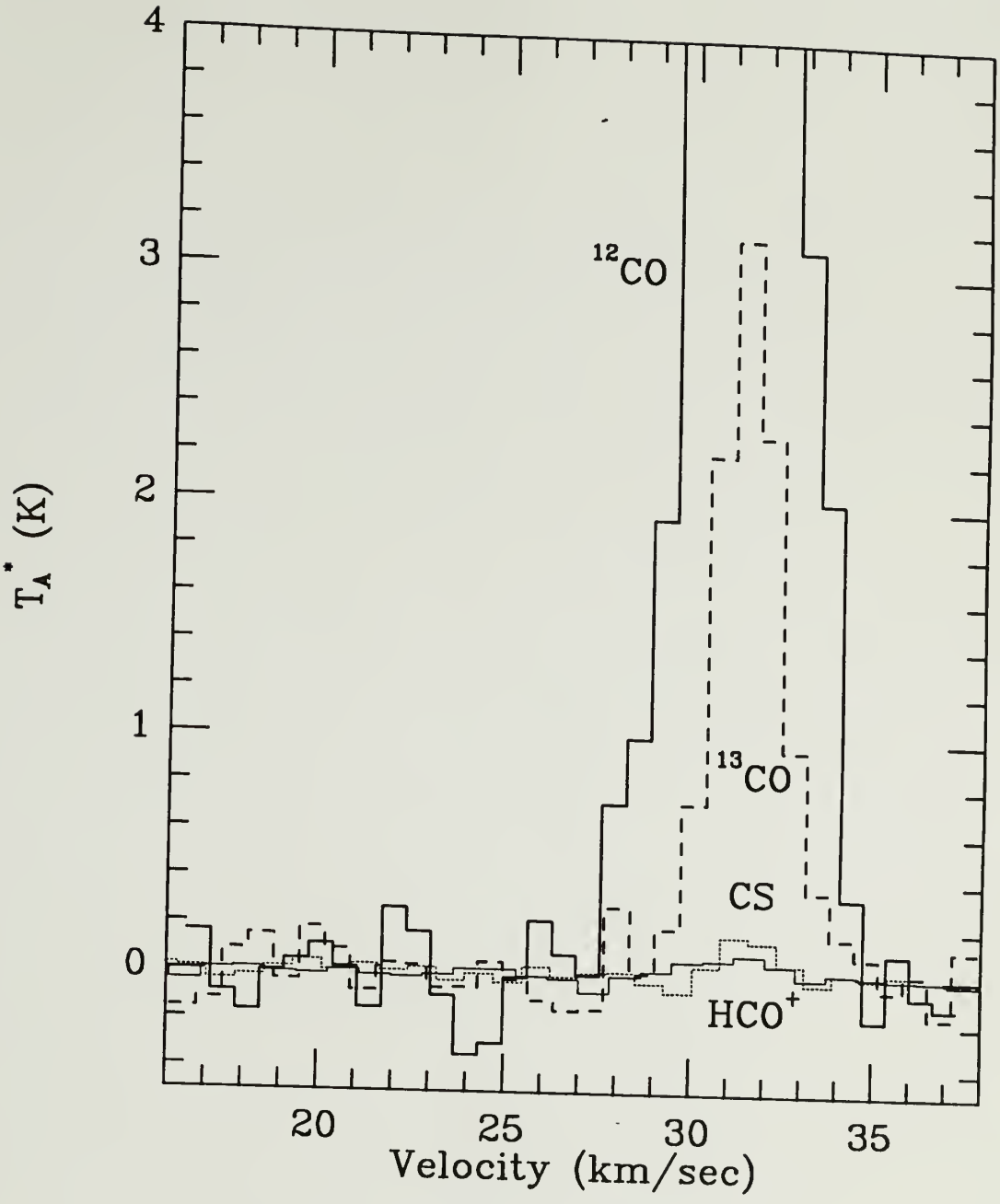

Figure 6.7 ^{12}CO, ^{13}CO, HCO$^+$, and CS spectra toward the IRAS source 06522-0350.

CHAPTER 7

SYNTHESIS AND DISCUSSION

7.1 Star Formation in G216-2.5

One of unique features of the GMC G216-2.5 is the absence of massive star formation. In addition, the large (few parsec) and massive (100 – 1000 $M_{\odot}$) cores found in most GMCs (Goldsmith 1988) are also absent. However, based on the FIR and near-infrared data we have identified several sites of relatively low luminosity and presumably low mass star formation within G216-2.5. These stars are found preferentially at the boundary of the main body of G216-2.5. Based on the near-infrared colors and magnitudes of these sources and the far-infrared emission for the regions, these stars are likely to be T Tauri stars. Many of the other IRAS point sources may also be star forming sites within G216-2.5; however, we could not uniquely identify near-infrared counterparts of these sources. Nevertheless, if these other IRAS point source are additional star forming sites within the cloud, their small FIR luminosity suggests that these are also regions of low mass star formation.

The CS observations have confirmed the existence of dense cores in G216-2.5. However, the cores that have been identified have sizes and masses more typical

of those found in dark clouds such as Taurus (Goldsmith 1988) rather than those found in GMCs. The dense cores found in most GMCs are several parsecs in extent and have CS antenna temperatures of 3 - 4 K (Goldsmith 1988). Again, the much weaker CS line strengths found for G216-2.5 cores are similar to the emission observed in dark clouds. Thus, the cloud cores in G216-2.5 relative to more typical GMCs are much smaller and less massive, and probably have much lower densities.

7.2 Gas and Dust Temperatures

Another interesting feature of G216-2.5 is that the ^{12}CO radiation temperature is much lower than normal GMCs. The peak antenna temperature (T_R^*) distribution for the cloud, displayed in Figure 7.1, is significantly different from that of the warmer GMC, S287 shown in Figure 7.2. These histograms show the distribution of the peak ^{12}CO antenna temperature in all positions in which T_R^* (^{13}CO) > 0.5 K binned in 0.14 K intervals. The average peak temperature is only$\sim$ 2 K for G216-2.5, while for S287 the average is 5.5 K.

The maximum ^{12}CO antenna temperature found in the main body of the cloud is 5.8 K, which translates into a gas kinetic temperature of 8.3 K (see Chapter 4), at the low end of temperatures found typically in dark clouds of 8 – 13 K (Dickman 1978a; and Snell 1981). Thus, an important question to be addressed is, why is the gas in G216-2.5 so cold ? First and foremost is the fact that G216-2.5 has no luminous internal heating sources, the closest OB associations are more than 500 pc from G216-2.6 (Table 7.1). The closest OB stars are found in S287 at a distance

of at least 100 pc, thus, the direct heating of G216-2.5 from stars in S287 would be very small (the earliest star in S287 is O9.5; Neckel *et al.* 1989 and Leisawitz 1988).

Table 7.1 Open clusters near G216-2.5 from Leisawitz (1988). Distance are in kpc, V_* is the stellar velocity, and V_{CO} is velocity of the CO emission when detected.

Name	*l*	*b*	*d (kpc)*	V_*	V_{CO}	*Earliest Star*	*Other name*
OCL499	203.6	0.1	1.5	16	-	B3	N2251
OCL515	206.2	-2.0	1.6	16	14	O4	N2244
OCL518	207.1	-0.9	1.7	-	-	OB	Collin104
Monoc	218.0	-0.4	2.4	40	27	O9.5	S287
OCL567	224.7	0.4	1.1	33	-	O9	N2353

In the absence of embedded stellar heating sources, which in fact are only effective at heating the gas in the dense cores where collisions can effectively couple the gas and dust temperatures, the primary heating mechanism for the gas is cosmic rays. Even though the interstellar radiation field plays an important role in heating the dust, the density of G216-2.5 is not sufficient to couple the dust and gas. Dust heating is probably important only in the denser regions of the cloud where $n(H_2) > 10^4$ cm^{-3}; thus cosmic-rays are the main heating mechanism for the gas in G216-2.5.

The temperature of the gas in G216-2.5 is probably established by the balance between cosmic-ray heating and gas radiative cooling. Goldsmith and Langer (1978) have shown that for the densities relevant for the bulk of G216-2.5 that the cooling of the gas is dominated by the emission of CO. To determine the rate at which energy is radiated from the cloud by collisionally excited molecular tran-

sitions requires a model for the radiative transfer. For nearly thermalized and optically thick transitions, such as ^{12}CO, the cooling per molecule is relatively independent of the molecular abundance and the density of the cloud. Once the opacity becomes large, the cooling must be that of a blackbody, thus depending only on the linewidth and temperature. We adopt the cooling rates given by Goldsmith and Langer (1978) (see Table 7.2). The primary coolants are carbon monoxide and its isotopes, ^{13}CO and $C^{18}O$.

Goldsmith and Langer (1978) adopted a local cosmic ray heating rate of $\Gamma_{CR} = 6.4 \times 10^{-28}$ n(H_2). However, it has been suggested that the flux may be reduced in the outer Galaxy (Dodds *et al.* 1975; Higdon 1979; and review by Bloemen 1989). Thus, we have considered two cosmic-ray heating rates: the rate given by Goldsmith and Langer and a rate reduced by a factor of two. Balancing the heating and cooling rates, we can solve for the temperature as a function of density, the results are tabulated in Table 7.2 and shown in Figure 7.3. Modeling of the ^{13}CO emission in G216-2.5 suggests that the density has to be at least 10^3 cm^{-3}, however, the weak CS emission suggests that the density is unlikely to be much greater than 10^4 cm^{-3}. As discussed in Chapter 4, the weak ^{12}CO emission observed translates into an unusually low kinetic temperature of the gas of < 8 K. For the Goldsmith and Langer rate and for densities of a few thousand cm^{-3}, which characterize most of the emission in ^{13}CO G216-2.5, the gas kinetic temperature is 8 – 10 K. This range of temperatures agrees very well with the temperatures found in dark clouds in the solar neighborhood without embedded heating sources (Dickman 1975; Snell 1981). Using the reduced heating rate, the gas kinetic temperature is $\sim$ 6 K at

the same density, which agrees well with the observational results for G216-2.5. Thus, the exceptionally low gas temperatures of G216-2.5 may be explained if the cosmic-ray flux is reduced by only a factor of 2 at 2 kpc beyond the solar circle.

Table 7.2 Total cooling rate and equilibrium temperature for two cosmic-ray heating rates.

$n(H_2)$ (cm^{-3})	Λ (ergs cm^{-3} s^{-1})	T (Γ_{CR})	T ($1/2\Gamma_{CR}$)
10^2	$1.5 \times 10^{-27} T^{1.4}$	14.6	8.9
3×10^2	$4.7 \times 10^{-27} T^{1.6}$	10.2	6.6
10^3	$6.8 \times 10^{-27} T^{2.2}$	7.9	5.8
4×10^3	$2.3 \times 10^{-26} T^{2.2}$	8.5	6.2
10^4	$1.5 \times 10^{-26} T^{2.7}$	9.4	7.3
10^5	$3.8 \times 10^{-26} T^{2.9}$	13.0	10.2

Dodds *et al.* (1975) reported an abrupt decrease in the flux of cosmic-rays beyond the solar circle, and Cersarky *et al.* (1977) and Higdon (1979) confirmed this based on SAS-2 γ-ray data. However, recent studies of the final SAS-2 data contradict this (Bloemen *et al.* 1984). Bloemen (1989) attributed the previous results of a gradient in the cosmic-ray number density to confusion due to the uncertainties in gas content of the Galaxy and to the differences between early SAS-2 results and the final data base. He asserts that a weak gradient in the cosmic-ray flux may be present, but that it is much smaller than found in early papers. However, to the model of Bloemen and Diegel (1989), the difference between the cosmic-ray number density in the solar neighborhood and 2 kpc beyond the solar circle is roughly a factor of 1.5 to 2. Thus, the lower cosmic-ray heating rate in the outer Galaxy can explain the low gas temperature of G216-2.5. Studies of

other outer Galaxy clouds by Mead and Kutner (1988) confirmed the low kinetic temperature of clouds there. They also suggested that a factor of 2 decrease in the cosmic-ray heating rate would explain the low kinetic temperatures of the molecular clouds they observed, which is consistent with our conclusion.

The mean dust color temperature of G216-2.5 is approximately 26 K, also lower than that of most GMCs (Mooney 1992). Since the dust is usually heated by embedded sources, the absence of embedded sources would explain the low dust temperature. However, Mooney (1992) suggested that the dust in G216-2.5 is colder than the dust in other non-massive star forming GMCs because the interstellar radiation field, which dominates the dust heating in the G216-2.5, is also reduced in the outer Galaxy.

We conclude that lower flux of both the cosmic-rays and the optical and UV radiation in the outer Galaxy is responsible for the exceptionally low gas and dust temperatures in G216-2.5.

7.3 Cloud Mass

In Chapter 4 we presented three different methods for estimating the mass of G216-2.5. The LTE mass estimate of $1 \times 10^5\ M_\odot$ was the smallest and the virial mass estimate of $6 \times 10^5\ M_\odot$ was the largest. In this section we discuss the uncertainties in these mass estimates.

7.3.1 *LTE Mass Estimate*

To determine the LTE mass, one needs to know the abundance of ^{13}CO. The abundance of ^{13}CO has been established from the estimate of visual extinction derived from the star counts (see Chapter 3). If the column density of ^{13}CO is underestimated due to the effects discussed in Chapter 4, then the abundance of ^{13}CO will also be underestimated by the same amount. Since the total gas column density is proportional to $N(^{13}CO)/X(^{13}CO)$, any error in deriving the LTE column density should not introduce an error in the total gas column density. Thus, even though the LTE ^{13}CO column density can be significantly underestimated for low hydrogen densities ($N(H_2) < 1000$ cm^{-2}), due to incorrect assumptions about the ^{13}CO excitation temperature in the LTE analysis, this should not dramatically effect the total gas column densities.

It is important to include the intercept in the $A_V - N(^{13}CO)$ relation, so that the total gas column density is directly linked to the estimate of the visual extinction. The presence of an intercept may be attributed to dust residing in the cloud envelope, which is primarily atomic hydrogen. However, the intercept can be in part due to material in which ^{13}CO is not excited. Thus, when both the slope and intercept are included in estimating hydrogen column densities, we obtain a mass that is somewhat independent of the LTE assumptions.

One may ask how accurately the visual extinctions can be estimated and total gas column density can be derived. While the correlation between total hydrogen column density and visual extinction was empirically established by Bohlin, Savage, and Drake (1978), it was only established for visual extinction less than 2

magnitudes. Thus, it is necessary to extrapolate the relation they found in order to apply it to molecular clouds, assuming the grain properties are the same as in lower density regions. There are also restrictions on the use of star counts to derive the visual extinction. Above $A_V = 5$ magnitudes, it is very difficult to determine the visual extinction using star count techniques, due to the lack of stars to count. However, since the visual extinction for only small portion of G216-2.5 is greater than 4 magnitudes, the extinction measurements should be accurate. Thus, we feel that the LTE mass estimate is relatively reliable.

7.3.2 Virial Mass Estimate

A number of assumptions enter into the determination of the virial mass, such as the definition of cloud size, the density structure, and the effect of saturation of the ^{12}CO linewidths. These could significantly affect virial mass estimate. Saturation broadening was discussed in detail by Lee, Snell, and Dickman (1990). Since the centroid velocity dispersion, which is not subject to saturation corrections, contributes a significant fraction of the total velocity dispersion in G216-2.5, the effects of saturation should be minimal.

The size definition is another parameter that enters the virial mass estimate. In Chapter 4 we have adopted the mean cloud diameter based on the total area of the cloud (Equation 4.14). The problem with this size estimate is that it depends on the sensitivity of the CO observations. If the data were less sensitive the cloud would appear smaller, whereas if the data were more sensitive, the cloud would appear larger. To correct this problem other definitions of cloud size have been

used (Solomon *et al.* 1987; and Carpenter, Snell and Schloerb 1990). Solomon *et al.* (1987) introduced a definition of size based on the temperature weighted size dispersions in l and b. Carpenter, Snell, and Schloerb (1990) also introduced a ^{12}CO intensity-weighted size dispersion for radius of clouds, similar to that of Solomon *et al.*

For a cloud with a fairly uniform distribution of emission, the difference between these size definitions and ours is very small. But for a very filamentary and fragmentary clouds, or a very elongated cloud, the difference between these size definitions can be large as a factor of two. For an elongated cloud, such as G216-2.5 using the definition of Carpenter, Snell, and Schloerb (1990) leads to 70 pc, 30% smaller than our estimate. A 30% smaller size leads to a 30% smaller virial mass, however, this does not explain the discrepancy with the LTE mass estimate.

Another parameter that affects the virial mass estimate is the density distribution of the cloud. For a spherical cloud with a r^{-1} density distribution, the derived virial mass will be 20% larger than that given by Equation 4.16. The constant (582 in Equation 4.16) is generally related to the assumed density distribution; Langer *et al.* (1989) used 640, Scoville *et al.* (1987), 698. Those are all within $\pm$ 20% of the value assumed here, not large enough to account for the mass discrepancy.

7.3.3 Mass Estimate Using a Conversion Factor from γ-ray Analysis

The conversion factor in the CO luminosity-mass relation has been established through γ-ray analysis. Several γ-ray studies (Lebrun *et al.* 1983; Bloemen *et al.* 1984; and summary by Bloemen 1989) found conversion constants ranging from 2

to 3×10^{20} cm^{-2} (K km s^{-1})$^{-1}$. Also the γ-ray analysis indicates that the conversion factor is roughly constant throughout the Galaxy (Bloemen 1987). The merit of this method is that it is independent of virial mass estimate of clouds. We have used a recent estimate of the conversion factor, 2.3×10^{20} cm^{-2} (K km s^{-1})$^{-1}$(Bloemen 1989), and obtained a mass $M_{CO} = 3 \times 10^5\ M_\odot$. However, one may still have reasons to be concerned about this estimate. The presence of a general relation between mass and CO luminosity may still be a result of clouds being in virial equilibrium. If G216-2.5 is not in virial equilibrium, yet the the clouds that established the empirical relation are, the mass of G216-2.5 could be still overestimated by this technique. Alternatively, the unusually low antenna temperature of the CO emission in G216-2.5 may indicate that it should provide less CO emission per unit mass than the average GMC. If this is the case, the mass may be underestimated.

Accurate determinations of mass are still very difficult. Similar analysis of clouds in the inner Galaxy (Lee, Snell, and Dickman 1990) found that virial mass estimates were on average a factor of 1.7 greater than the LTE mass estimates. However, Carpenter, Snell, and Schloerb (1990) found a good agreement between LTE and virial masses.

A factor of two or even three difference between mass estimates could easily be attributed to the uncertainties mentioned above. The factor of 6 difference for G216-2.5 is somewhat large and may reflect the unusual properties of this cloud; the discrepancy between the virial and other mass estimates, if real, may reflect the unusual dynamical state of G216-2.5. The kinematics of this cloud are discussed further in the next section.

7.4 Kinematics and Evolutionary Status of G216-2.5

G216-2.5 has a very striking velocity structure. Rings and expanding shell-like structure are seen both in the channel maps and in spatial-velocity maps. The features are similar to those found in active star forming clouds. However, in these clouds (e.g. Gem OB1; Carpenter, Snell, and Schloerb 1992) there are obvious stellar sources to drive the expanding shells and to generate the rich structure observed. The morphology of the molecular clouds associated with Gem OB1 is dominated by filaments and arcs of molecular material, presumably formed by expanding H II regions and stellar winds from young stars within the cloud. One of the molecular clouds at $\alpha = 05^h57^m$, $\delta = +20°$ within the Gem OB1 complex has a properties very similar to those of G216-2.5. However, this cloud is clearly part of a much larger arc of molecular gas that encircles the S252/S247 star forming regions. The radius of this arc is $\sim$ 120 pc. J. Carpenter kindly provided his ^{12}CO and ^{13}CO data for this region for comparison. We have estimated LTE and virial masses in the same way as for G216-2.5; the virial mass derived is $M_{VIR} = 6 \times 10^5\ M_\odot$, and the LTE mass derived is $M_{LTE} = 8 \times 10^4\ M_\odot$. The mass estimates are very similar to those for G216-2.5, and the discrepancy between the two mass estimates are similar. The other remarkable aspects of this cloud are the broad line widths, very low gas temperatures, and total absence of massive star formation. The distribution of peak antenna temperatures of the cloud Gem OB1-c is shown in Figure 7.4, and is surprisingly similar to that of G216-2.6 (Figure 7.1). Thus, G216-2.5 and Gem OB1-c are nearly twin clouds. However, it is clear in the case

of Gem OB1-c that it is part of a large shell structure surrounding the active star forming sites.

A warmer GMC, S287, is located $\sim$ 100 pc from G216-2.5, and is probably physically related as discussed earlier. Its mass and size are substantially smaller than G216-2.5 (roughly one tenth) and only a few stars (one late O star, and several B stars) are associated. There is no apparent gas connection between the two clouds, as the region between the two clouds was observed in ^{12}CO with 15′ sampling, though this does not completely rule out a possible association of the two clouds. One may wonder if the association between G216-2.5 and S287 is similar to that of Gem OB1-c and S252/S247.

An important issue to address is the evolutionary status of G216-2.5. Maddalena and Thaddeus (1985) suggested, based on the absence of massive star formation and its very low temperature, that G216-2.5 have relatively young and had not evolved to the point of star formation. Similar suggestions for the evolutionary status of G216-2.5 has been made by Blitz (1991). However, if GMCs are long-lived they may undergo episodic massive star formation events. Mooney (1992) describes a scenario in which GMCs undergo a massive star formation burst, fragment and expand, and then appear as quiescent cold clouds, with the fossil remains of the past burst of star formation. Thus, one may ask whether G216-2.5 is young or in this quiescent phase of evolution.

A number of facts about G216-2.5 favor an evolutionary state that places it between episodes of massive star formation. First, the cloud has a relatively large velocity dispersion for a non-star-forming GMC, what one might expect of the

aftermath of a star formation burst. Second, there are clear evidence for shells and rings within the cloud, which may be the fossil remains of earlier star formation activity. Third, the kinematics of the cloud are dominated by a global velocity gradient, suggesting that the cloud is part of a very large expanding shell. Lastly, the discrepancy between the LTE and virial masses may be explained if the cloud has been severely perturbed and is currently expanding. In addition, one can use the very striking similarities between G216-2.5 and Gem OB1-c to argue that both clouds are in similar evolutionary states, and for Gem OB1-c the evidence that it is part of a shell produced by the past star formation activity is much more convincing. Thus, we believe that G216-2.5 is a remnant cloud from an older star formation event. The still active S287 cloud and another nearby cloud mapped by Maddalena and Thaddeus (1985) may all have been part of the molecular cloud complex that included G216-2.5.

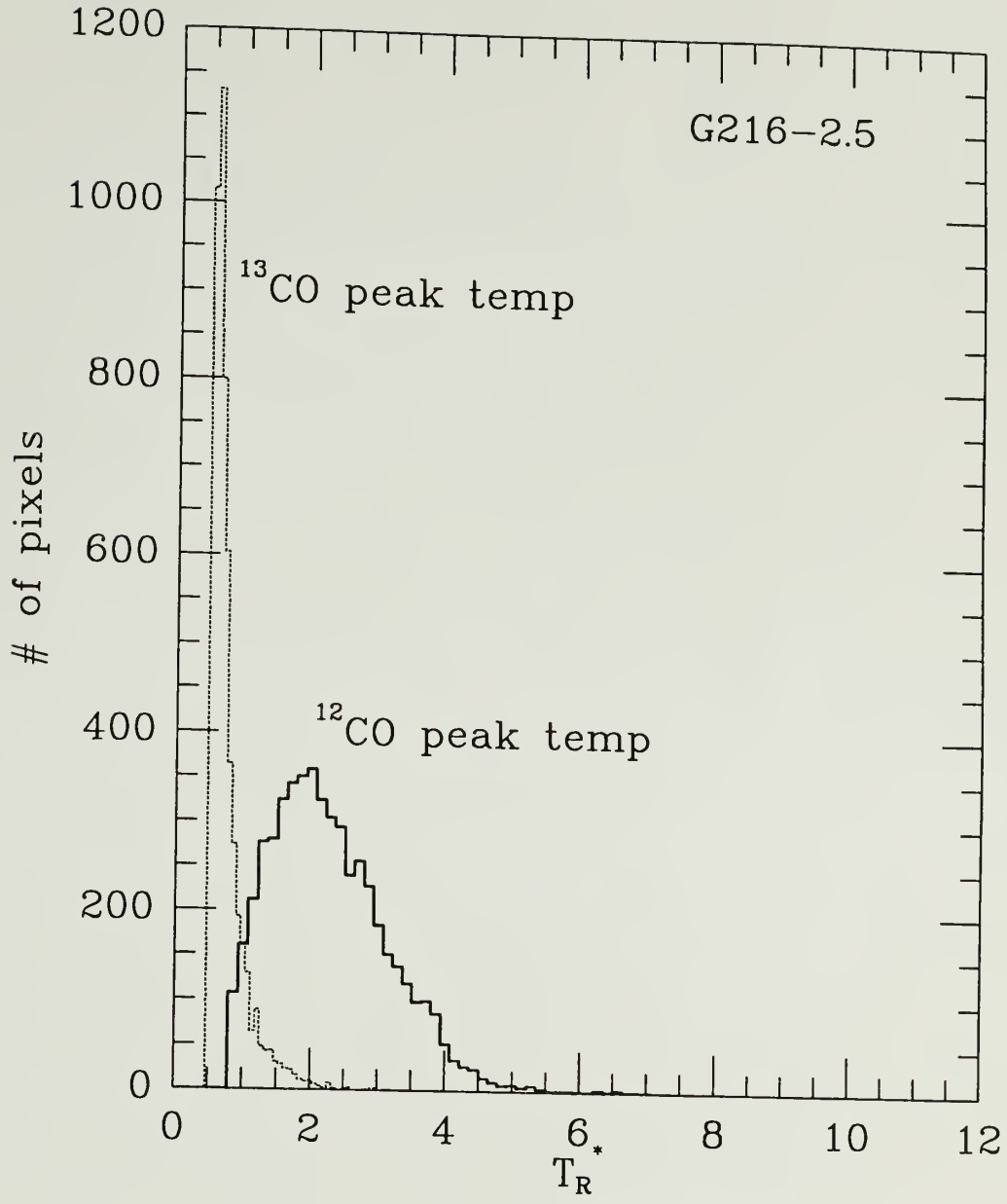

Figure 7.1 The ^{12}CO and ^{13}CO peak temperature distribution of G216-2.5. All positions with T_R^* (^{13}CO) > 0.5 K are shown. The antenna temperatures are binned in 0.14 K intervals.

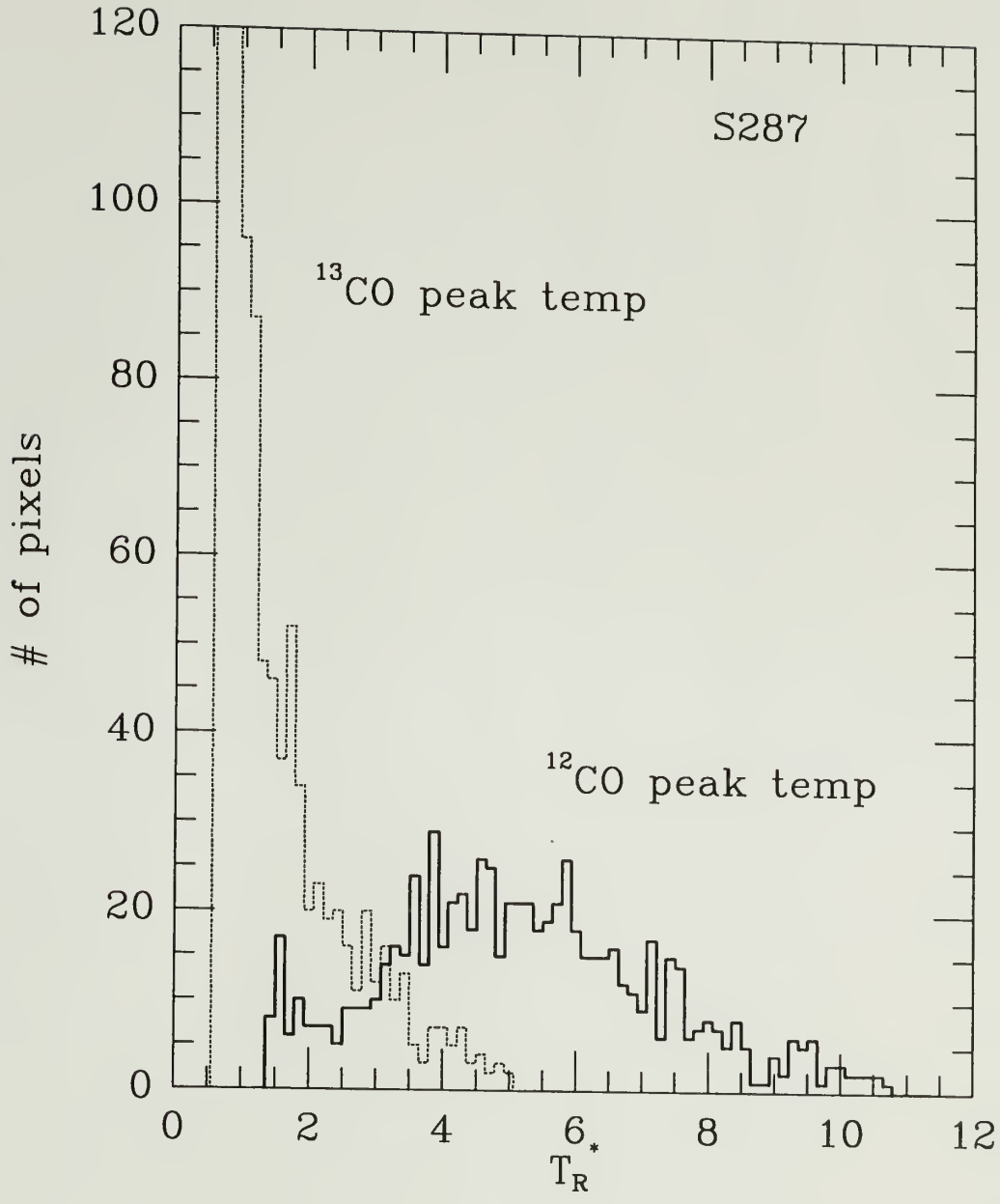

Figure 7.2 The ^{12}CO and ^{13}CO peak temperature distribution of S287. All positions with T_R^* (^{13}CO) > 0.5 K are shown. The antenna temperatures are binned in 0.14 K intervals.

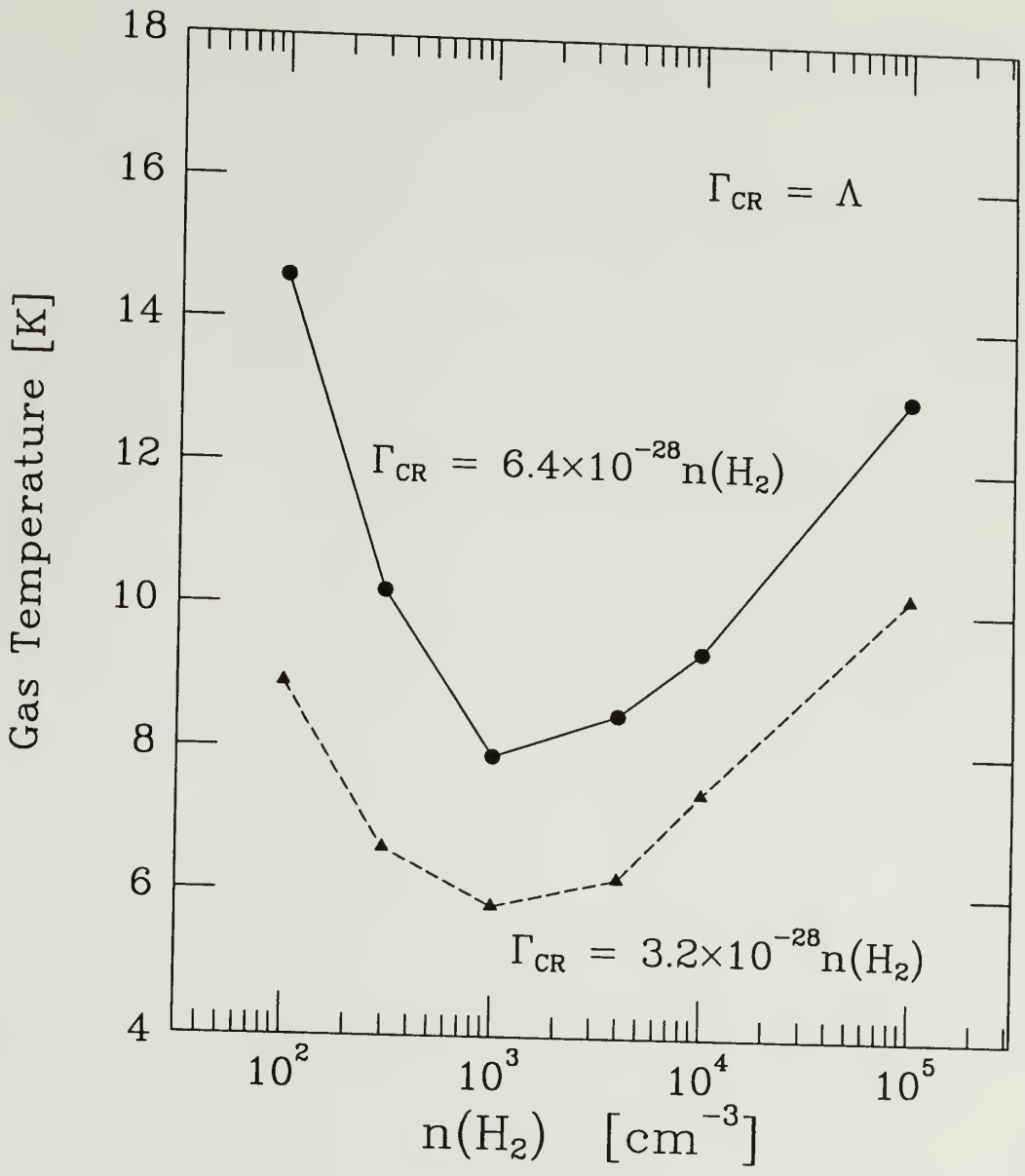

Figure 7.3 The equilibrium gas kinetic temperature as a function of density for two different cosmic-ray heating rates.

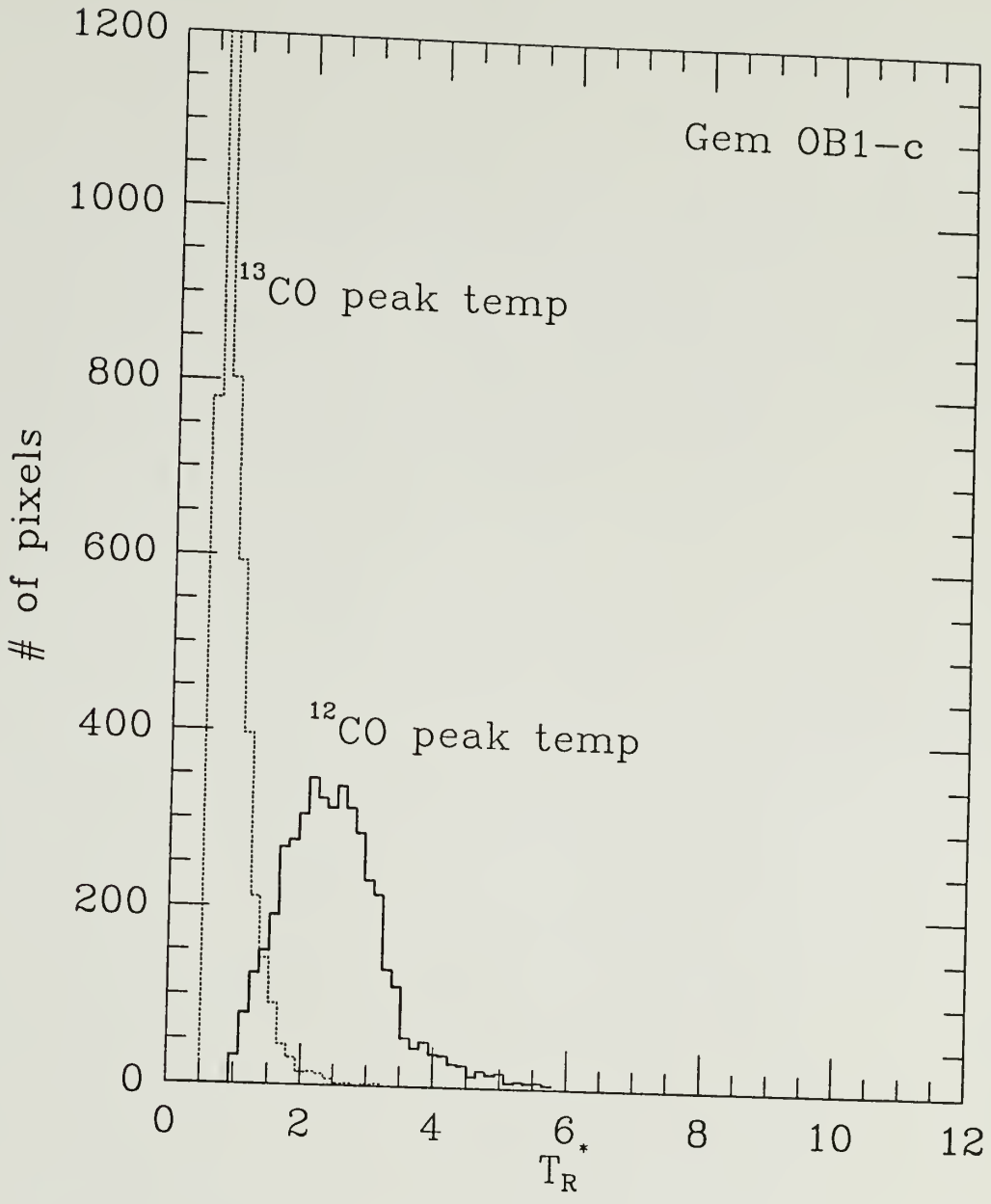

Figure 7.4 The ^{12}CO and ^{13}CO peak temperature distribution of Gem OB1-c. All positions with T_R^* (^{13}CO) > 0.5 K are shown. The antenna temperatures are binned in 0.14 K intervals.

CHAPTER 8

SUMMARY

This dissertation presents the first high resolution observations of a cold, massive molecular cloud that is not forming high mass stars. The results of this study are summarized below.

• We have mapped G216-2.5 (Maddalena's cloud), in the emission of the J = 1–0 transition of ^{12}CO and ^{13}CO using FCRAO's QUARRY fifteen beam array receiver. Each map contains 57,300 spectra covering a region 11 square degrees in extent, with observations spaced by 50″. As originally pointed out by Maddalena and Thaddeus (1985), we have confirmed that the cloud is unusually cold and has very broad linewidths ($\Delta V \sim 8$ km s^{-1}).

• The visual extinction of the highest CO column density region was determined by star counts, and the results were used to investigate the gas and dust properties of the cloud. The ^{13}CO column density to visual extinction ratio is found to be similar to that found in local molecular clouds, suggesting that if the gas to dust ratio is normal, the ^{13}CO abundance relative to molecular hydrogen in this cloud is similar to that of the clouds near the sun. Our best estimate of the ^{13}CO abundance relative to molecular hydrogen is 1.73×10^{-6}.

• A number of IRAS point sources were identified toward or near G216-2.5. Nine of these sources have been imaged in the near-infrared. Photometry at J, H, and K bands suggest that low luminosity, and presumably low mass stars are forming in this cloud. However, the star formation appears to be occurring preferentially at the edge of the cloud. Two groups of young stars with $\sim$ 5 to 7 members have been identified in two small clouds adjacent to the main body of the cloud. Stellar masses have been estimated using a luminosity–mass relation derived from known T Tauri stars and Ae/Be stars. The masses of the stars are roughly estimated to be between 0.3 to 2.8 $M_{\odot}$.

• The high resolution CO observations confirmed the low gas kinetic temperature found by Maddalena and Thaddeus (1985). The gas temperature of $<$ 8 K is similar to those for dark clouds. The gas heating in G216-2.5 is dominated by cosmic-rays. The somewhat lower temperature found over most of G216-2.5 can be explained if the cosmic-ray flux is smaller by a factor of $\sim$ 2 in the outer Galaxy. The average temperature of the dust based on the extended emission at 60 and 100 μm is 26 K. The low dust temperature is due to the lack of internal heating sources. The dust heating is probably dominated by the interstellar radiation field (ISRF), and the weaker ISRF inferred by Mooney (1992) can explain the exceptionally low dust temperatures found in G216-2.5.

• The LTE mass has been estimated to be $1.1 \times 10^5 M_{\odot}$ and the virial mass has been estimated to be $6.3 \times 10^5 M_{\odot}$. A detailed discussion of the various sources of uncertainty in the determination was presented. The discrepancy between the two mass estimates of a factor of 6 is larger than expected based on the uncertainties

in these methods. If the LTE mass is correct, the large virial mass may reflect the fact that G216-2.5 is not gravitationally bound.

- The average density of G216-2.5 is $10 \sim 60$ cm^{-3} much lower that that of most GMCs. Models of the cloud emission indicate that the density of the gas responsible for producing the ^{13}CO and CS emission must be substantially larger, suggesting that the density structure of the cloud is very inhomogeneous.

- A number of facts about G216-2.5 favor an evolutionary state in which the cloud is between episodes of massive star formation. First, the cloud has a relatively large velocity dispersion for a non-star-forming GMC, as what might expect of the aftermath of a star formation burst. Second, there is clear evidence for shells and rings within the cloud, which may be the fossil remains of its earlier star formation activity. Third, the kinematics of the cloud is dominated by a global velocity gradient suggesting that the cloud is part of a very large expanding shell. Lastly, the discrepancy between the LTE and virial masses may be explained if the cloud has been severely perturbed and is currently expanding. In addition, the striking similarities between G216-2.5 and Gem OB1-c argue that both clouds are in similar evolutionary state. Thus, we believe that G216-2.5 is a remnant cloud from a past episode of massive star formation; the large star forming complex may include the S287 molecular cloud.

BIBLIOGRAPHY

[1] Bachiller, R., and Cernicharo, J. 1986, *AA*, 166, 283.

[2] Beckwith, S. V. W., Sargent, A. I., Chini, R. S., and Güsten, R. 1990, *AJ*, 99, 924.

[3] Blitz, L., 1991, in *The Physics of Star Formation and Early Stellar Evolution*, eds. C. H. Lada and N. D. Kylafis. (Dordrecht: Kluwer Academic Publishers), p. 1.

[4] Blitz, L., Fich, M., and Stark, A. A. 1982, *ApJS*, 49, 183.

[5] Bloemen, J. B. G. M. 1985, *Ph.D. Dissertation.* Leiden University.

[6] Bloemen, J. B. G. M. 1987, in *Interstellar Process*, eds. D. J. Hollenbach and H. A. Thronson, Jr. (Dordrecht: Reidel), p. 143.

[7] Bloemen, J. B. G. M. 1989, *ARAA*, 27, 469.

[8] Bloemen, J. B. G. M. and Dogiel V. A. 1989, in preparation.

[9] Bloemen, J. B. G. M., Caraveo, P. A., Hermsen, Lebrun, F., Maddalena, R. J., Strong, A. W., and Thaddeus, P. 1984, *AA*, 139, 37.

[10] Bohlin, R. C., Savage, B. D., and Drake, J. F. 1978, *ApJ*, 224, 132.

[11] Bok, B. J., and Corwell, C. S. 1973, in *Molecules in the Galactic Environment*, eds. M. A. Gordon, and L. E. Snyder (New York: Wiley), p. 53.

[12] Boulanger F., and Pérault, M. 1988, 330, 964.

[13] Carpenter, J. M., Snell, R. L., and Schloerb, F. P. 1990, *ApJ*, 362, 147.

[14] Carpenter, J. M., Snell, R. L., and Schloerb, F. P. 1992, private communication.

[15] Carpenter, J. M., Snell, R. L., Schloerb, F. P., and Skrutskie, M. F. 1992, *ApJ* submitted.

[16] Cernicharo, J., and Guélin, M. 1987, *AA*, 176, 299.

[17] Cersarky C. J., Cassé, M., Paul, J. A. 1977 *AA*, 60, 139.

[18] Cox, P. and Mezger, P. G. 1989, *AAR*, 1, 49.

[19] Dickman, R. L. 1975, *ApJ*, 202, 57.

[20] Dickman, R. L. 1978a, *ApJS*, 37, 407.

[21] Dickman, R. L. 1978b, *AJ*, 83, 363.

[22] Dickman, R. L. 1988, in *Molecular Clouds in the Milky Way and External Galaxies*, eds. R. L. Dickman, R. L. Snell, and J. S. Young (Dordrecht: Reidel), p. 55.

[23] Dickman, R. L. and Clemens, D. P. 1983, *ApJ*, 271, 143.

[24] Dickman, R. L., and Herbst, W. L. 1990, *ApJ*, 357, 531.

[25] Dickman, R. L., and Kleiner, S. C. 1985, *ApJ*, 295, 479.

[26] Dickman, R. L., Snell, R. L., and Schloerb, F. P. 1986, *ApJ*, 306, 326.

[27] Diegel, S., Bally, J., and Thaddeus, P. 1990, *ApJ*, 357, L29.

[28] Dodds, D., Strong, A. W., and Wolfendale, A. W., 1975, *MNRAS*. 171, 569.

[29] Duvert, G., Cernicharo, J., and Baudry, A. 1985, *AA*, 164, 2.

[30] Elias, J. H., Frogel, J. A., Matthews, K., and Neugebauer, G. 1982 *AJ*, 87, 1029.

[31] Elmegreen, D. M., and Elmegreen, B. G. 1979, *AJ*, 84, 615.

[32] Emerson, J. P., 1985, in *IAU Symposium No. 115; Star Forming Regions*, eds. M. Peimbert and J. Jugaku, p. 19.

[33] Encrenaz, P. J., Falgarone, E., and Lucas, R. 1975, *AA*, 44, 73.

[34] Erickson, N. R., Goldsmith, P. F., Giles, N., Grosslein, R. M., Viscuso, P. J., Erickson, R. B., and Predmore, R. 1992, *IEEE Trans. Microwave Theory and Techniques*, 40(1), 1.

[35] Feitzinger, J. V., and Spiker, J. 1987, *AA*, 184, 122.

[36] Frerking, M. A., Langer, W. D., and Wilson, R. W. 1982, *ApJ*, 262, 590.

[37] Fukui, Y. 1989, in *ESO Workshop No. 33; Low Mass Star Formation and Pre-main Sequence Objects*, ed. B. Reipurth, p. 95.

[38] Goldreich, P., and Kwan., J. 1974, *ApJ*, 189, 441.

[39] Goldsmith, P. F. 1988, in *Molecular Clouds in the Milky Way and External Galaxies*, eds. R. L. Dickman, R. L. Snell, and J. S. Young (Dordrecht: Reidel), p. 1.

[40] Goldsmith, P. F. and Langer, W. D. 1978, *ApJ*, 881.

[41] Green, S. and Thaddeus, P. 1976, *ApJ*, 205, 766.

[42] Haslam, C. G. T., Salter, C. J., Stoffel, H., and Wilson, W. E. 1981, *AA*, 67, 1.

[43] Henderson, A. P., Jackson, P. D., and Kerr, F. J. 1982, *ApJ*, 263, 116.

[44] Herbst, W., and Sawyer, D. L. 1981, *ApJ*, 243, 935.

[45] Heyer, M. H., Vrba, F. J., Snell, R. L., Schloerb, F. P., Strom. S. E., Goldsmith, P. F., and Strom, K. M. 1987, *ApJ*, 321, 855.

[46] Higdon, J. C. 1979, *ApJ*, 232, 113.

[47] Hildebrand, R. H. 1983, *Quart. J. Roy. Ast. Soc.*, 24, 267.

[48] Hillenbrand, L. A., Strom, S. E., Keene, J., and Vrba, F. J. 1992, *ApJ*, submitted.

[49] Humpreys, R. M. 1978, *ApJS*, 38, 309.

[50] Irvine, W. M., Goldsmith, P. F., and A. Hjalmarson 1987, in *Interstellar Processes*, eds. D. L. Hollenbach and H. A. Thronson Jr., (Dordrecht: Reidel), p. 561.

[51] Isobe, T., Feigelson, E. D., Akritas, M. G., and Babu, G. J. 1990, *ApJ*, 364, 104.

[52] Kennedy, P. M., and Buscombe, W. 1977, *MK Spectral Classifications* (Evanston, IL: Northwestern University).

[53] Koorneef, J. 1983, *AA*, 128, 84.

[54] Kutner, M. C., and Ulich, B. L. 1981, *ApJ*, 250, 341.

[55] Kutner, M. C. 1984, *Fundamentals of Cosmic Physics*, 9, 233.

[56] Lada, C. J., and Adams, F. C. 1992, *ApJ*, 393, 278.

[57] Langer, W., Wilson, R. W., and Goldsmith P. F. 1989, *ApJ*, 337, 355.

[58] Lebrun, F., Bennet, K., Bignami, G., Bloemen, J. B. G. M., Bucherri, R., 1983, *ApJ*, 281, 634.

[59] Lee, Y., Snell, R. L., and Dickman, R. L. 1991, *ApJ*, 379, 639.

[60] Leisawitz, D., 1988 *Catalog of Open Clusters and Associated Interstellar Matter,* NASA Reference Publication RP-1202.

[61] Lonsdale, G., Helou, G., Good, J. C., and Rice, W. 1985, *Catalogued Galaxies and Quasars Observed in the IRAS Survey* (Pasadena: Jet Propulsion Laboratory).

[62] MacLaren, I., Richardson, K. M., and Wolfendale, A. W. 1988, *ApJ*, 333, 821.

[63] Maddalena, R. J., and Thaddeus, P. 1985, *ApJ*, 294, 231.

[64] Maloney, P. R., 1987, *Ph.D. Dissertation*, University of Arizona, Tucson.

[65] Mead, C. 1988, *ApJS*, 67, 149.

[66] Mead, C. and Kutner, M. C. 1988, *ApJ*, 330, 399.

[67] Mead, C., Kutner, M. C., and Evans II, N. J. 1990, *ApJ*, 354, 492.

[68] Mooney T. 1992, *Ph.D. Dissertation*, University of New York, Stony Brook.

[69] Myers, P. C., Dame, T. M., Thaddeus, P., Cohen, R. S., Silverberg, R. F., Dwek, E., and Hauser, M. G. 1986, *ApJ*, 301, 398.

[70] Myers, P. C. 1987, in *Interstellar Process*, eds. D. J. Hollenbach and H. A. Thronson, Jr. (Dordrecht: Reidel), p.71.

[71] Neckel, T., Staude, H. J., Meisenheimer, K., Chini, R., and Gusten, R. 1989, *AA*, 210, 378.

[72] Penzias, A. A. 1975, in *Atomic and Molecular Physics and the Interstellar Matter*, Les Houghes 1974 Session XXVI, eds. R. Balian, P. Encrenaz and J. Lequeux (New York: North-Holland), p. 373.

[73] Rhijn, P. J. van 1929, *GroningenPublication* 43.

[74] Sanders, D. B., Solomon, P. M., and Scoville, N. Z. 1984, *ApJ*, 276, 182.

[75] Scoville, N. Z., and Solomon, P. M. 1974, *ApJL*, 187, L67.

[76] Scoville, N. Z., and Sanders, D. B. 1987, in *Interstellar Processes*, eds. D. J. Hollenbach and H. A. Thronson, Jr., p. 21.

[77] Scoville, N. Z., Yun, M. S., Clemens, D. P., Sanders, D. B., and Waller, W. H. 1987, *ApJS*, 63, 821.

[78] Sharpless, S. 1959, *ApJS*, 4, 257.

[79] Snell, R. L. 1981, *ApJS*, 45, 121.

[80] Snell, R. L., Mundy, L. G., Goldsmith, P. F., Evans, N. J. II, and Erickson, N. R. 1984, *ApJ*, 276, 625.

[81] Snell, R. L., Heyer, M. H., F. P. Schloerb 1989, *ApJ*, 337, 739.

[82] Sodroski, T. J. 1991, *ApJ*, 366, 95.

[83] Solomon, P. M., Rivolo, A. R., Barret, J., and Yahil, A. 1987, *ApJ*, 319, 730.

[84] Solomon, P. M., and Rivolo, A. R. 1989, *ApJ*, 339, 919.

[85] Thaddeus, P., and Channan, G. A. 1985, *Nature*, 314, 73.

[86] Tucker, K. D., Dickman, R. L., Encrenaz, P. J., Kutner, M. L. 1976, *ApJ*, 210, 679.

[87] Walker H. J., Cohen, M., Volk, K., Wainscoat, R. J., and Schwarz, D. E. 1989, AJ, 98, 2163.

[88] Weaver, R. G., and Williams, R. D. 1973, *AAS*, 8, 1.

[89] Wielen, R., Jahreiss, H., and Krüger, R. 1983, in *IAU Colloquium 76, The Nearby Stars and the Stellar Luminosity Function*, eds. A. G. D. Phillip and A. R. Upgren (Schenectady: L. Davis), p. 163.